SPATIAL INTERFERENCE CANCELLATION AND CHANNEL ESTIMATION FOR MULTIPLE-INPUT MULTIPLE-OUTPUT WIRELESS COMMUNICATION SYSTEMS

Mr. Chaiyod Pirak

A Dissertation Submitted in Partial Fulfillment of the Requirements
for the Degree of Doctor of Philosophy in Electrical Engineering
Department of Electrical Engineering
Faculty of Engineering
Chulalongkorn University
Academic Year 2005

ISBN 974-53-2403-5

การขจัดสัญญาณแทรกสอดเชิงปริภูมิ และ การประมาณค่าช่องสัญญาณ สำหรับระบบสื่อสารไร้สายแบบหลายทางเข้าหลายทางออก

นายชัยยศ พิรักษ์

วิทยานิพนธ์นี้เป็นส่วนหนึ่งของการศึกษาตามหลักสูตรปริญญาวิศวกรรมศาสตรดุษฎีบัณฑิต
สาขาวิชาวิศวกรรมไฟฟ้า ภาควิชาวิศวกรรมไฟฟ้า
คณะวิศวกรรมศาสตร์ จุฬาลงกรณ์มหาวิทยาลัย
ปีการศึกษา 2548

ISBN 974-53-2403-5

Thesis Title	SPATIAL INTERFERENCE CANCELLATION AND CHANNEL ESTIMATION FOR MULTIPLE-INPUT MULTIPLE-OUTPUT WIRELESS COMMUNICATION SYSTEMS
By	Mr.Chaiyod Pirak
Field of Study	Electrical Engineering
Thesis Advisor	Associate Professor Somchai Jitapunkul, Dr.Ing.
Thesis Co-advisor	Professor K.J. Ray Liu, Ph.D.

Accepted by the Faculty of Engineering, Chulalongkorn University in Partial Fulfillment of the Requirements for the Doctor's Degree

. . . . . Dean of the Faculty of Engineering
(Professor Direk Lavansiri, Ph.D.)

THESIS COMMITTEE

. . . . . Chairman
(Professor Prasit Prapinmongkolkarn, D.Eng.)

. . . . . Thesis Advisor
(Associate Professor Somchai Jitapunkul, Dr.Ing.)

. . . . . Thesis Co-advisor
(Professor K.J. Ray Liu, Ph.D.)

. . . . . Member
(Professor Monai Krairiksh, D.Eng.)

. . . . . Member
(Assistant Professor Taptim Angkaew, D.Eng.)

. . . . . Member
(Assistant Professor Chedsada Chinrungrueng, Ph.D.)

ชัยยศ พิรักษ์: การขจัดสัญญาณแทรกสอดเชิงปริภูมิและการประมาณค่าช่องสัญญาณ สำหรับระบบสื่อสารไร้สายแบบหลายทางเข้าหลายทางออก(SPATIAL INTERFERENCE CANCELLATION AND CHANNEL ESTIMATION FOR MULTIPLE-INPUT MULTIPLE-OUTPUT WIRELESS COMMUNICATION SYSTEMS), อ. ที่ปรึกษา: รองศาสตราจารย์ ดร.สมชาย จิตะพันธ์กุล, อ. ที่ปรึกษาร่วม: Professor Dr. K.J. Ray Liu, 138 หน้า, ISBN 974-53-2403-5

ระบบสื่อสารไร้สายแบบหลายทางเข้าหลายทางออก เป็นระบบสื่อสารที่โดดเด่นระบบหนึ่ง ซึ่งสามารถสนองความต้องการในการให้บริการการส่งข้อมูลความเร็วสูงของระบบสื่อสารไร้สายในอนาคต ระบบสื่อสารนี้สามารถเสริมสมรรถนะของระบบสื่อสารไร้สายได้อย่างมีนัยสำคัญ ทั้งในด้านการเพิ่มอัตราข้อมูลโดยอัตราการขยายเชิงสหสัญญาณ ในด้านการลดความน่าจะเป็นในการตัดสินผิดพลาดโดยอัตราการขยายเชิงซ้ำ และในด้านการขจัดการแทกสอดจากการเข้าถึงหลายทางโดยสายอากาศที่ชาญฉลาด อย่างไรก็ตามข้อมูลของช่องสัญญาณที่แม่นยำเป็นสิ่งที่มีความจำเป็นอย่างยิ่งสำหรับระบบสื่อสารดังกล่าวที่ติดตั้งเครื่องรับแบบเชื่อมติดกัน การได้เปรียบทางสมรรถนะและปัญหาที่กล่าวมาข้างต้นนี้เป็นแรงจูงใจในการทำวิทยานิพนธ์ฉบับนี้

ในส่วนแรกของวิทยานิพนธ์นำเสนอระบบสายอากาศที่ชาญฉลาดแบบใหม่สำหรับเครื่องรับแบบขจัดการแทรกสอดในระบบไดเร็คซีเควนซ์ซีดีเอมเอ ระบบที่นำเสนอใช้ประโยชน์ของข้อมูลรหัสแผ่กระจายของผู้ใช้เพียงอย่างเดียวในการปรับน้ำหนักสำหรับควบคุมทิศทางของลำคลื่น ระบบที่นำเสนอสามารถทนทานต่อการแทรกสอดภายในลำคลื่นโดยเฉพาะในสภาพแวดล้อมแบบใกล้-ไกล สมรรถนะของระบบที่นำเสนอได้ถูกวิเคราะห์ในเชิงการลู่เข้า และความน่าจะเป็นในการตัดสินผิดพลาด ผลการวิเคราะห์และการจำลองการทำงานแสดงให้เห็นว่า ระบบที่นำเสนอมีสมรรถนะที่ผลดีกว่าระบบเดิมที่มีอยู่ในด้านต่าง ๆ ดังที่กล่าวมา

ในส่วนที่สองของวิทยานิพนธ์นำเสนอตัวประมาณค่าช่องสัญญาณแบบใหม่ สำหรับระบบสื่อสารหลายทางเข้าหลายทางออกซึ่งถูกเข้ารหัสเชิงปริภูมิ-เวลา และสำหรับระบบสื่อสารหลายทางเข้าหลายทางออกชนิดสหสัญญาณแบบแบ่งความถี่เชิงตั้งฉากซึ่งถูกเข้ารหัสเชิงปริภูมิ-ความถี่ ตามลำดับ ในระบบแรกได้นำเสนอกรรมวิธีฝังสัญญาณนำร่องแบบใหม่สำหรับใช้ในการร่วมประมาณค่าช่องสัญญาณ และตรวจวัดข้อมูล และนำเสนอตัวประมาณค่าช่องสัญญาณแบบความควรจะเป็นสูงสุดแบบไร้เงื่อนไข และแบบค่าคลาดเคลื่อนกำลังสองเฉลี่ยน้อยสุดเชิงเส้น สมรรถนะของระบบที่นำเสนอได้ถูกวิเคราะห์โดยการวัดค่าคลาดเคลื่อนกำลังสองเฉลี่ยของการประมาณค่าช่องสัญญาณ การเปรียบเทียบขอบเขตล่างของ Cramer-Rao และการเปรียบเทียบขอบเขตบนของ Chernoff ของอัตราความผิดพลาดบิตสำหรับรหัสเชิงปริภูมิ-เวลา การจัดสรรกำลังอย่างเหมาะสมได้ถูกศึกษาในระบบที่นำเสนอด้วย ผลการวิเคราะห์และการจำลองการทำงานแสดงให้เห็นว่า เมทริกซ์ตัวถือข้อมูลและเมทริกซ์สัญญาณนำร่องที่มีโครงสร้างแบบสหสัญญาณรหัสมีประสิทธิภาพสูงสุดเมื่อเทียบกับโครงสร้างแบบอื่นในช่องสัญญาณไม่เสมือนคงที่ ในระบบที่สองได้นำเสนอนัยทั่วไปของระบบฝังสัญญาณนำร่องที่นำเสนอในระบบแรก รวมทั้งการประมาณค่าช่องสัญญาณสมนัยแบบกำลังสองน้อยสุด และการตรวจวัดข้อมูลสมนัยแบบความควรจะเป็นสูงสุด ตัวประมาณค่าช่องสัญญาณปรับตัวได้และไม่ได้ชนิดฐาน FFT แบบกำลังสองน้อยสุดได้ถูกนำเสนอต่อมาเพื่อปรับปรุงสมรรถนะของตัวประมาณค่าช่องสัญญาณที่กล่าวมา สมรรถนะของระบบที่นำเสนอได้ถูกวิเคราะห์โดยการวัดค่าความคลาดเคลื่อนกำลังสองเฉลี่ยของการประมาณค่าช่องสัญญาณดังกล่าวข้างต้น ผลกระทบของค่าความคลาดเคลื่อนของการไม่สอดคล้องเชิงแบบสำหรับโพรไฟล์การประวิงของช่องสัญญาณหลายวิถีที่ไม่เป็นค่าจำนวนเต็มสำหรับตัวประมาณค่าช่องสัญญาณดังกล่าวข้างต้นได้ถูกวิเคราะห์ต่อมา จำนวนของแท็ปที่เหมาะสมสำหรับตัวประมาณค่าช่องสัญญาณปรับตัวได้ชนิดฐาน FFT แบบกำลังสองน้อยสุดได้ถูกศึกษาด้วย ผลการวิเคราะห์และการจำลองการทำงานแสดงให้เห็นว่าตัวประมาณค่าช่องสัญญาณปรับตัวได้นี้ มีสมรรถนะสูงสุดเมื่อเทียบกับตัวประมาณค่าช่องสัญญาณที่นำเสนอทั้งหมด

ภาควิชา	วิศวกรรมไฟฟ้า	**ลายมือชื่อนิสิต**	. . . . .
สาขาวิชา	วิศวกรรมไฟฟ้า	**ลายมือชื่ออาจารย์ที่ปรึกษา**	. . . . .
ปีการศึกษา	2548	**ลายมือชื่ออาจารย์ที่ปรึกษาร่วม**	. . . . .

##4471806721: MAJOR ELECTRICAL ENGINEERING
KEY WORD: ARRAY SIGNAL PROCESSING / SPATIAL INTERFERENCE CANCELLATION / CHANNEL ESTIMATION / PILOT EMBEDDING / MIMO / OFDM / CDMA
CHAIYOD PIRAK: SPATIAL INTERFERENCE CANCELLATION AND CHANNEL ESTIMATION FOR MULTIPLE-INPUT MULTIPLE-OUTPUT WIRELESS COMMUNICATION SYSTEMS, THESIS ADVISOR: SOMCHAI JITAPUNKUL, Dr.Ing., THESIS CO-ADVISOR: K.J. RAY LIU, Ph.D., 138 pp., ISBN 974-53-2403-5

A multiple-input multiple-output (MIMO) wireless communication system is one of prominent systems for realizing high data-rate transmission services highly demanded in the future wireless communications. It can provide a significant performance enhancement to the wireless communications, including increased data rates through a multiplexing gain, an enhanced error probability through a diversity gain, and cancellation of multiple access interference through smart antennas. However, for such system employing coherent receivers, an accurate channel state information is crucially needed. These performance advantages and challenge, respectively, are the motivations of this dissertation.

In the first part of this dissertation, a novel smart antenna system for interference canceling receivers in direct-sequence code-division multiple access (DS-CDMA) systems is proposed. This proposed scheme only exploits the spreading codes of users as the information for its weight adjustment for controlling its beam. This proposed scheme is also robust to the in-beam interference, especially in the near-far effect situation. Convergence and error probability performance analysis is also carried out. Theoretical and simulation results indicate that the proposed scheme outperforms the existing works.

In the second part of this dissertation, novel channel estimators for space-time (ST) coded MIMO systems and for space-frequency coded MIMO-orthogonal frequency-division multiplexing (OFDM) systems are proposed, respectively. For the first systems, the novel pilot-embedding approach for joint channel estimation and data detection is first proposed. The unconstrained maximum likelihood (ML) and linear minimum mean square error (LMMSE) channel estimators are then proposed. Mean square error (MSE) of the channel estimation, Cramer-Rao lower bound, and Chernoff's bound of bit error rate for ST codes are analyzed for examining the proposed scheme's performances. The optimum power allocation is also investigated. Theoretical and simulation results show that a code-multiplexing based structure for the data-bearer and pilot matrices is the best among all other structures for nonquasi-static channels. For the second systems, a generalization of the proposed pilot-embedding scheme as well as the corresponding least square (LS) channel estimation and ML data detection are first proposed. Then, LS and adaptive LS FFT-based channel estimators are proposed to improve the performance of such channel estimator. The effect of model mismatch error for non-integer multipath delay profiles and MSE of these channel estimators are analyzed. The optimum number of taps for the adaptive LS FFT-based channel estimator is also determined. Theoretical and simulation results indicate that the adaptive LS FFT-based channel estimator is the best among all other channel estimators.

Department Electrical Engineering	Student's signature . . . . .
Field of study Electrical Engineering	Advisor's signature . . . . .
Academic year 2005	Co-advisor's signature . . . . .

Acknowledgements

First of all, I would like to sincerely thank my advisor, Dr.Somchai Jitapunkul. His contributions to my dissertation and personal life style were the greatest things in my graduate study. He was the first person who gave me an opportunity to develop myself in various aspects, such as a vision for the future research, skills for handling research problems, and how to become a good researcher. His contributions and supports have never been faded from my memory forever.

The next person who I would like to express my gratitude to is Dr.K.J.Ray Liu. I would like to sincerely thank him for being my advisor when I was pursuing my Ph.D. research in the United States of America. His contributions to my dissertation were the best. He did not only teach me about how to conduct the front-running research, but he also taught me how to become the good researcher. His success is my motivation to follow up. His contributions and supports have retained in my memory forever.

The third person I would like to pay gratitude to is Dr.Z.Jane Wang. She was the best supervisor for me in both a colleague aspect and a personal aspect. She did not only supervise me on how to conduct the good research and write the research journal paper in a professional writing style, she also taught me how to handle the reviewers' comments as well as the other problems I had faced in USA. Her contributions to my dissertation and life style have never been erased from my memory forever.

I would like to extend my gratitude to Dr.Prasit Prapinmongkolkarn, Dr.Monai Krairiksh, Dr.Taptim Angkaew, and Dr.Chedsada Chinrungrueng for being my defense committees. Their suggestions as well as insightful discussions greatly helped me to improve the quality of this dissertation. I would like to acknowledge King Mongkut's Institute of Technology North Bangkok and Commission on Higher Education, Ministry of Education, Royal Thai Government for granting the Ph.D. scholarship to support my entire Ph.D. programme. I would also like to acknowledge the grants from Dr.K.J.Ray Liu and from the Cooperation Project between Department of Electrical Engineering and Private Sector for Research and Development, Chulalongkorn University, Thailand, in supporting me for pursuing my research. Without these funding, this dissertation could never be completed.

I would like to acknowledge Chulalongkorn University, Thailand; the Digital Signal Processing Research Laboratory; University of Maryland College Park, USA.; the Institute for System Research; and the Communications and Signal Processing Laboratory for providing me the great facilities throughout my Ph.D. programme.

Finally, I would like to express my deep gratitude to my family for supporting me throughout my Ph.D study. Their encouragement, warmth, and love were the great power for me to overcome all troubles I had faced. The last person who always give me the will power to produce a good work and overcome all obstacles is my girlfriend, Tantawan. Without them, I could not pass this Ph.D. journey with the success.

Table of Contents

Chapter Page

Chapter Page

List of Tables

List of Figures

Figure Page

CHAPTER I

INTRODUCTION

Wireless communications is the rapidly growth segment of the communication industries. It has captured the attention of media and the imagination of the public, and become one of the necessary elements in the daily life. Since the establishment of cellular systems that experienced drastically growth over the last decade, they are now serving around two billion users worldwide. Indeed, cellular phones have become an important tool for both business and resident sectors in most developed countries, and are rapidly replacing wired systems in many developing countries. In addition, wireless local area networks (LANs) have been aggressively replacing wired networks in many homes, businesses, and campuses. From the past to the present, many new applications, including wireless sensor networks, automated highways and factories, smart home and appliances, and remote telemedicine, are emerging from research ideas to concrete systems. Further, the rapid growth of wireless system in conjunction with the rapid expansion of laptop and palmtop computers indicates a bright future for wireless networks, both as stand-alone system and as part of the larger networking infrastructure.

1.1 Wireless Communication Systems

There are two most common wireless communication systems involving in our everyday life: cellular telephone systems and wireless LANs. Therefore, it is of importance to introduce such systems.

1.1.1 Cellular Telephone Systems

Cellular telephone systems are popular and lucrative worldwide. Indeed, the wireless revolution is ignited by such systems. Cellular systems provide two-way voice and data communication with regional, national, or international coverage. Nowadays, these systems have evolved to support lightweight handheld mobile terminals operating inside and outside

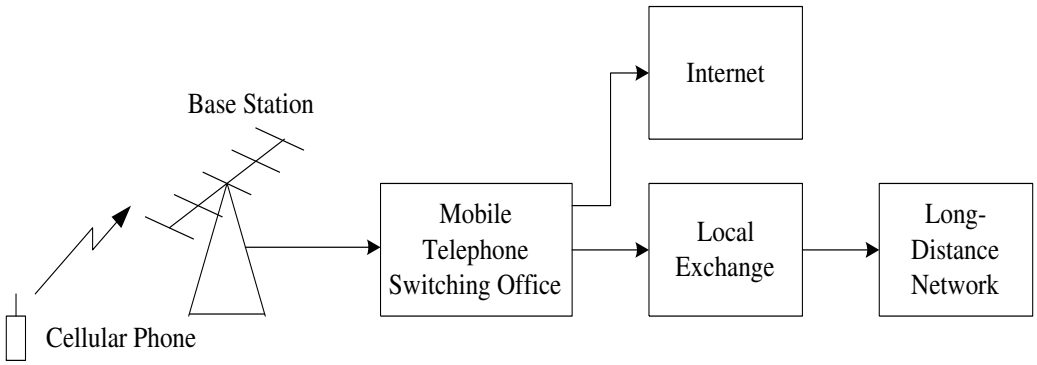

Figure 1.1 Current cellular network structure.

buildings at both pedestrian and vehicle speeds, in opposition to the old system where the terminals were installed inside vehicles with antennas mounted on the vehicle roof.

The basic principle of cellular systems is frequency reuse, which exploits the fact that signal power falls off with distance to reuse the same frequency spectrum at spatially-separated locations. In fact, the coverage area of the cellular systems is divided into non-overlapping cells where some set of channels is assigned to each cell. This same channel set is used in another cell at some distance away. Operation within a cell is controlled by a centralized base station. The interference caused by users in different cells operating on the same channel set is called *intercell interference*. The spatial separation of cells that reuse the same channel set, i.e. the reuse distance, should be as small as possible so that frequencies are used as often as possible, thereby maximizing spectral efficiency. However, as the reuse distance decreases, intercell interference increases, due to the smaller propagation distance between interfering cells. Since intercell interference must remain below a given threshold for acceptable system performance, reuse distance cannot be reduced below some minimum value. In practice, it is quite difficult to determine this minimum value since both the transmitting and interfering signals experience random power variations due to the characteristics of wireless signal propagation. In order to determine the best reuse distance and base station placement, an accurate characterization of signal propagation within the cells is needed.

All base stations in a given geographical area are connected via a high-speed communications link to a mobile telephone switching office (MTSO), as shown in Fig.1.1. The MTSO serves as a central controller for the network, allocating channels within each cell,

coordinating handoff between cells when a mobile traverses a cell boundary, and routing calls to and from mobile users. A new user located in a given cell requests a channel by sending a call request to the cell's base station over a separate control channel. The request is relayed to the MTSO, which accepts the call request if a channel is available in that cell. If no channels are available, then the call request is rejected. A call handoff is initiated when the base station or the mobile in a given cell detects that the received signal power for that call is approaching a given minimum threshold. In this case, the base station informs the MTSO that the mobile requires a handoff, and the MTSO then queries surrounding base stations to determine if one of these stations can detect that mobile's signal. If so, then the MTSO coordinates a handoff between the original base station and the new base station. If no channels are available in the cell with the new base station, then the handoff fails and the call is terminated. A call will also be dropped if the signal strength between a mobile and its base station drops below the minimum threshold needed for communication due to random signal variations.

Efficient cellular system designs are *interference-limited*, i.e. the interference dominates the noise floor since otherwise more users could be added to the system. As a result, any technique to reduce interference in cellular systems leads directly to an increase in system capacity and performance. Some methods for interference reduction in use today or proposed for the future systems include cell sectorization, directional and smart antennas, multiuser detection, and dynamic resource allocation.

The first generation of cellular systems used analog communications, since they were primarily designed in the 1960's, before digital communications became prevalent. Second generation systems moved from analog to digital due to its many advantages. The components are cheaper, faster, smaller, and require less power. Digital systems also have higher capacity than analog systems since they can use more spectrally-efficient digital modulation and more efficient techniques to share the cellular spectrum. Due to their lower cost and higher efficiency, service providers used aggressive pricing tactics to encourage user migration from analog to digital systems, and today analog systems are primarily used in areas with no digital services. However, digital systems do not always work as well as the analog ones. Users can experience poor voice quality, frequent call dropping, and spotty coverage in certain areas. The third generation cellular systems are able to provide

higher transmission rates than the second generation cellular systems. It still uses the digital modulation technique similar to the second generation one. In addition, it can provide different data rates depending on mobility and location. However, it is not compatible with the second generation systems, so service providers must invest in a new infrastructure before they can provide the third generation cellular system services. Until now, it still debates in many countries about the third generation standard as well as the worth of deploying such systems in comparison to upgrading the second generation systems to cope the demand for high data transmission services.

1.1.2 Wireless LANs

Wireless LANs provide high-speed data within a small region, e.g. a campus or small building, as users move from place to place. Typically, wireless devices that access these LANs are stationary or moving at pedestrian speeds. All wireless LANs standards in the U.S. operate in unlicensed frequency bands. The primary unlicensed bands are the industrial, scientific, and medical (ISM) bands at 900 MHz, 2.4 GHz, and 5.8 GHz, and the unlicensed national information infrastructure (U-NII) band at 5 GHz. In the ISM bands, unlicensed users are secondary users so must cope with interference from primary users when such users are active; meanwhile, there are no primary users in the U-NII band. A federal communications commission (FCC) license is not required to operate in these two bands. However, this advantage comes at the the price of additional interference caused by other unlicensed systems operating in these bands for the same reason. The interference problem can be minimized by setting a limit on the power per unit bandwidth for unlicensed systems. Wireless LANs can have either a star architecture, with wireless access points or hubs placed throughout the coverage region, or a peer-to-peer architecture, where the wireless terminals self-configure into a network.

The first generation wireless LANs were first proposed and designed in the early 1990's, which were based on proprietary and incompatible protocols. Most operated within the 26 MHz spectrum of the 900 MHz ISM bands using direct sequence spread spectrum, with data rates on the order of 1-2 Mbps. Unfortunately, the lack of standardization for these products led to high development costs, low-volume production, and small markets for each individual product.

The second generation wireless LANs were further developed for improving a low data-rate in the first generation one. As such, the well-known IEEE 802.11b standard was proposed. It can support the data rates of around 1.6 Mbps (raw data rates of 11 Mbps), operating with 80 MHz of spectrum in the 2.4 GHz ISM bands by exploiting the direct sequence spread spectrum technology. The growth rate of 802.11b wireless LANs has explosively increased resulting from a relatively high volume of productions produced by many companies and the adoption of this technology in the computer industry, i.e. the integration of 802.11b wireless LANs cards in many laptop computers.

Two additional standards in the 802.11 family were developed to provide higher data rates than 802.11b: IEEE 802.11a and IEEE 802.11g. The 802.11a standard is based on multicarrier modulation, and can support 20-70 Mbps data rates. It operates with 300 MHz of spectrum in the 5 GHz U-NII band. In addition, it can accommodate a large number of users at higher data rates due to the larger bandwidth used in this standard, in comparison to the 802.11b standard. The other standard, 802.11g, also uses multicarrier modulation and can be used in either the 2.4 GHz and 5 GHz bands with speeds of up to 54 Mbps. Many wireless LANs cards and access points support all three standards to avoid incompatibility.

There are many technical issues to be addressed for wireless communication systems, including how to improve the system capacity with a high data rate and how to remove interference signals, e.g. spatial and temporal interference signals, from such systems. In the next section, a prominent system, namely a multiple-input multiple-output (MIMO) system, that can overcome such difficulties will be described.

1.2 Multiple Antennas and Space-Time Communications

In this section, the wireless communication systems with multiple antennas at the transmitter and receiver are presented. These systems are commonly known as MIMO communication systems. An exploitation of the multiple antennas at both transmitter and receiver can provide the performance advantages in terms of increasing data rates through multiplexing gain and improving error probability performance through diversity gain. In MIMO communication systems, the transmit and receive antennas can both be used for diversity gain. Multiplexing gain can be obtained by exploiting the structure of the channel gain matrix to create independent signalling paths that can be used to send independent

data. Historically, the initial excitement about MIMO was started by the pioneering work of Winters [1], Foscini [2], Gans [3], and Telatar [4,5] predicting remarkable spectral efficiencies for wireless communication systems with multiple transmit and receive antennas. These spectral efficiency gains often require accurate knowledge of the channel at the receiver, and sometimes at the transmitter as well. Therefore, the issue about channel estimation is of crucially interest accordingly, especially for the systems employing coherent receivers or the systems employing transmit filters for compensating channel variations. In addition to spectral efficiency gains, intersymbol interference (ISI) and interference from other users can be reduced by using smart antenna techniques. The cost of the performance enhancements obtained through MIMO techniques comes at the expense of deploying multiple antennas, the extra space and power of these extra antennas, and the added complexity required for multi-dimensional signal processing. More details will be discussed as follows.

1.2.1 MIMO Wireless Fading Channels

Wireless fading channels of point-to-point MIMO communication systems with L_t-transmit and L_r-receive antennas can be classified into two categories: narrowband MIMO fading channels and frequency-selective MIMO fading channels. Narrowband MIMO fading channels are also called flat (or frequency-nonselective) MIMO fading channels. For the narrowband MIMO fading channels, there exists only a direct path connecting the L_t-transmit antennas onto L_r-receive antennas [6]. Therefore, there are L_tL_r channel links in such channel models. In addition, since there is no multiple paths in this kind of channels, the channels do not suffer from ISI. For the other channels, frequency-selective MIMO fading channels, there exists multiple paths in each pair of transmit and receive antennas. These channels could suffer from ISI when the bandwidth of such channels is larger relative to the channel's multipath delay spread. There are two approaches to dealing with ISI in MIMO channels [6]. First, a channel equalizer can be used to mitigate the effects of ISI. However, the equalizer is much more complex in MIMO channels since the channel must be equalized over both space and time. Second, multicarrier modulation or orthogonal frequency division multiplexing (OFDM) can be employed as an alternative to equalization in frequency-selective fading channels. Frequency-selective MIMO fading channels exhibit diversity across space, time, and frequency, so ideally all three dimensions should be fully

exploited in the signalling scheme.

Different assumptions can be assumed about the knowledge of the channels at the transmitter and receiver. For a static channel, the channel state information (CSI) at the receiver is typically assumed known, since the channel gains can be obtained easily by sending a training sequence for channel estimation. If a feedback path is available, then CSI at the receiver can be sent back to the transmitter to provide CSI at the transmitter. When the channel is not known at either the transmitter or receiver, then some distribution on the channel gain must be assumed. The most common model for this distribution is a zero-mean spatially white (ZMSW) model, where the channel gain is assumed to be identically independently distributed (i.i.d) zero-mean unit-variance, complex circularly symmetric Gaussian random variable. In general, different assumptions about CSI and about the distribution of the channel gain lead to different channel capacities and different approaches to space-time signalling.

1.2.2 Performance Advantages of MIMO Communication Systems

Different strategies for exploiting the multiple antennas at the transmitter and receiver lead to different performance advantages of the MIMO communication systems. Here, a summary of such advantages is presented.

1.2.2.1 MIMO Multiplexing Gain

When both the transmitter and receiver have multiple antennas, there is a mechanism for performance gain called multiplexing gain. The multiplexing gain of a MIMO system stems from the fact that a MIMO channel can be decomposed into a number R of parallel independent channels. By multiplexing independent data onto these independent channels, an R-fold increase in data rates can be achieved in comparison to a system with just one antenna at the transmitter and receiver. This increased data rate is called the *multiplexing gain.*

In order to obtain independent channels from the MIMO system, the MIMO channel with $L_r \times L_t$ channel gains needs to be assumed known to both the transmitter and receiver. Let $\mathbf{H}$ be an $L_r \times L_t$ channel gain matrix and R_H be a rank of $\mathbf{H}$ of the MIMO system. The process for obtaining the independent channels are summarized as follows. First, the

singular value decomposition (SVD) is performed for $\mathbf{H}$, to arrive at

$$\mathbf{H} = \mathbf{U}\mathbf{\Sigma}\mathbf{V}^H, \tag{1.1}$$

where the $L_r \times L_r$ matrix $\mathbf{U}$ and the $L_t \times L_t$ matrix $\mathbf{V}$ are unitary matrices, and $\mathbf{\Sigma}$ is an $L_r \times L_t$ diagonal matrix of singular values $\{\sigma_i\}$ of $\mathbf{H}$. Since R_H is the rank of $\mathbf{H}$, it cannot exceed the number of columns or rows of $\mathbf{H}$, $R_H \leq \min(L_t, L_r)$. If $\mathbf{H}$ is full rank, which is sometimes referred to as a rich scattering environment, then $R_H = \min(L_t, L_r)$. Other environments may lead to a low rank $\mathbf{H}$: a channel with high correlation among the gains in $\mathbf{H}$ may have rank 1. Second, the parallel decomposition of the channel is obtained by defining a transformation on the channel input and output through *transmit precoding* and *receiver shaping*, respectively. Specifically, in transmit precoding, the input to the transmitter antennas is generated through a linear transformation by pre-multiplying the original input vector with $\mathbf{V}$. Receiver shaping performs a similar operation at the receiver by pre-multiplying the channel output vector with $\mathbf{U}^H$. As a result, the transmit precoding and receiver shaping transform the MIMO channel into R_H parallel single-input single-output (SISO) channels. Note that multiplication by a unitary matrix does not change the distribution of the noise. Finally, by sending independent data across each of the parallel channels, the MIMO channel can support R_H times the data rate of a system with just one transmit and receive antenna, leading to a multiplexing gain of R_H. Note, however, that the performance on each of the channels will depend on its gain σ_i.

1.2.2.2 MIMO Diversity Gain

Alternatively, the multiple antennas at the transmitter and receiver can be used to obtain diversity gain instead of capacity gain. In this setting, the same symbol, weighted by a complex scale factor, is sent over each transmit antenna, so that the input covariance matrix has unit rank. By pursuing this strategy, the error probability performance will be improved, since more channels are used for sending the same symbol, proportionally to a number of the transmit and receive antennas used. This improved error probability performance is called the *diversity gain*. This strategy corresponds to the transmit precoding and receiver shaping described in section 1.2.2.1 being just column vectors: $\mathbf{V} = \mathbf{v}$ and $\mathbf{U} = \mathbf{u}$. This strategy provides diversity gain by coherently combining of the multiple signal paths. Channel knowledge at the receiver is typically assumed since this is required for coherent

combining. The diversity gain then depends on the availability of the knowledge of channels at the transmitter. When the channel matrix $\mathbf{H}$ is known, the received signal-to-noise ratio (SNR) is optimized by choosing $\mathbf{u}$ and $\mathbf{v}$ as the principal left and right singular vectors of the channel matrix $\mathbf{H}$, respectively. When the channel is not known, at the transmitter, the transmit antenna weights are all equal. In addition, the lack of transmitter CSI will result in a lower SNR and capacity than with optimal transmit weighting. This strategy has obviously reduces capacity relative to optimizing the transmit precoding and receiver shaping matrices at an additional benefit of the reduced demodulation complexity.

1.2.2.3 Multiplexing/Diversity Tradeoffs

From the previous sections, there are two mechanisms for utilizing multiple antennas to improve wireless system performance. One option is to obtain capacity gain by decomposing the MIMO channel into parallel channels and multiplexing different data streams onto these channels. This capacity gain is referred to as a multiplexing gain. However, the SNR associated with each of these channels depends on the singular values of the channel matrix. Alternatively, the strategy for exploiting the multiple antennas to achieve a diversity gain can be done by coherently combining the channel gains. It is not necessary to use the antennas purely for multiplexing or diversity. Some of the space-time dimensions can be used for diversity gain, and the remaining dimensions used for multiplexing gain.

The multiplexing/diversity tradeoff or, more generally, the tradeoff between data rates, probability of error, and complexity for MIMO systems has been studied in the literature, from both a theoretical perspective and in terms of practice space-time code designs [7--9]. These works have primarily focused on block fading channels with receiver CSI only since when both transmitter and receiver know the channels, the tradeoff is relatively straightforward: antenna subsets can first be grouped for diversity gain and then the multiplexing gain corresponds to the new channels with reduced dimension due to the grouping. For the block fading model with receiver CSI only, as the block length grows asymptotically large, full diversity gain and full multiplexing gain (in terms of capacity with outage) can be obtained simultaneously with reasonable complexity by encoding diagonally across antennas [10, 11]. For finite block lengths, it is not possible to achieve full diversity and full multiplexing gains simultaneously, in which case there is a tradeoff between these gains. It is well-known

that, in the MIMO system with L_t-transmit and L_r-receive antennas, if all transmit and receive antennas are used for diversity, the error probability will be proportional to $\text{SNR}^{L_t L_r}$. Moreover, some of these antennas can be used to increase data rates at the expense of diversity gain. It is also possible to adapt the diversity and multiplexing gains relative to channel conditions. Specifically, in poor channel states, more antennas can be used for diversity gain; whereas, in good states, more antennas can be used for multiplexing gain.

1.2.2.4 Smart Antennas

From the previous sections, the multiple antennas at the transmitter and/or receiver can provide diversity gain as well as increased data rates through multiplexing gain. Alternatively, sectorization or phased array techniques can be used to provide directional antenna gain at the transmit or receive antenna array. This directionality can increase the signalling range, reduce delay-spread (or, equivalently, ISI) and flat-fading, and suppress interference between users. In particular, interference typically arrives at the receivers from different directions. Thus, directional antennas can exploit these differences to null or attenuate interference arriving from given directions, thereby increasing system capacity. The reflected multipath components of the transmitted signal also arrive at the receiver from different directions, and can also be attenuated, thereby reducing ISI and flat-fading. The benefits of directionality that can be obtained with multiple antennas must be weighted against their potential diversity or multiplexing benefits, giving rise to multiplexing/diversity/directionality tradeoffs. Whether it is best to use the multiple antennas to increase data rates through multiplexing, increase robustness to fading through diversity, or reduce ISI and interference through directionality is a complex tradeoff decision that depends on the overall system design.

The most common directive antennas are sectorized or phased (directional) antenna arrays, and the radiation patterns for these antennas along with an omnidirectional antenna radiation pattern are shown in Fig.1.2.

Directional antennas (or smart antennas) typically use antenna arrays coupled with phased array techniques to provide directional gain, which can be tightly controlled with sufficiently many antenna elements. Phased array techniques work by adapting the phase of each antenna element in the array, which changes the angular locations of the antenna beams (angles with large gain) and nulls (angles with small gain), via the use of weight vector, as

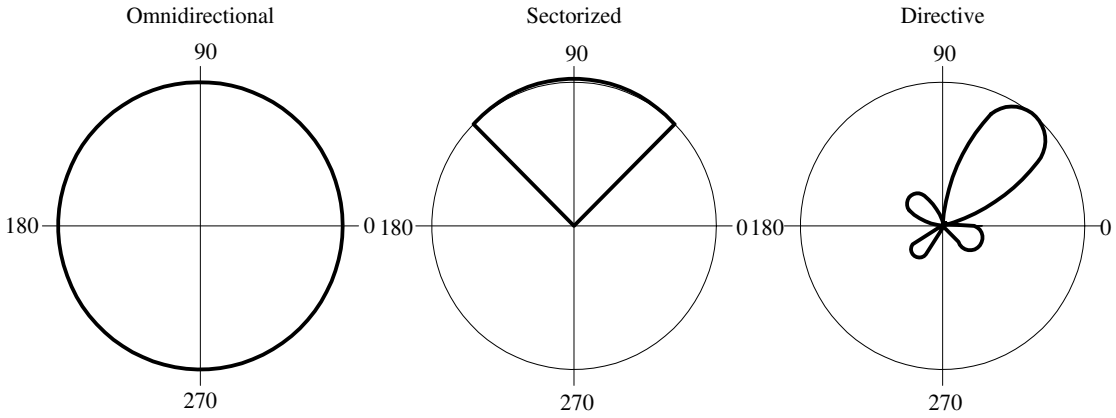

Figure 1.2 Antenna radiation patterns for omnidirectional, sectorized, and directive antennas.

shown in Fig.1.3 In Fig.1.3, $\mathbf{w} = [w_0, \ldots, w_{M-1}]^T$ denotes the weight vector and M denotes a number of array antenna's elements. For the array antenna with M elements, $M-1$ nulls can be formed to significantly reduce the received power of $M-1$ separate interferers. If there are $M_I < M-1$ interferers, then the M_I interferers can be cancelled out using M_I+1 antennas in a phased array, and the remaining $M-M_I-1$ antennas can be used for diversity gain. Note that directional antennas must know the angular location of the designed and interfering signals to provide high or low gains in the appropriate directions. Tracking of user locations can be a significant impediment in highly mobile systems, which is why cellular base stations use sectorization instead of directional antennas. The complexity of array antenna processing along with the required real estate of an array antenna make the use of smart antennas in small, lightweight, low-power handheld devices unlikely in the near future. However, base stations and access points already use the array antenna in many cases.

From Fig.1.3, the smart antennas basically consists of three major parts: an array antenna, an array processor, and a demodulator. The most important part for the smart antennas is the array processor, in which the adaptive algorithm module plays a major role in controlling the weight vector $\mathbf{w}$. The adaptive algorithms for adjusting the weight vector can be divided into two approaches: a non-blind approach, in which the training signal is used to provide a prior knowledge of the location of the desired signal, and a blind approach, in which no training signal is employed. For the non-blind adaptive algorithm approach, many methods had been proposed, e.g. the minimum mean square error (MMSE),

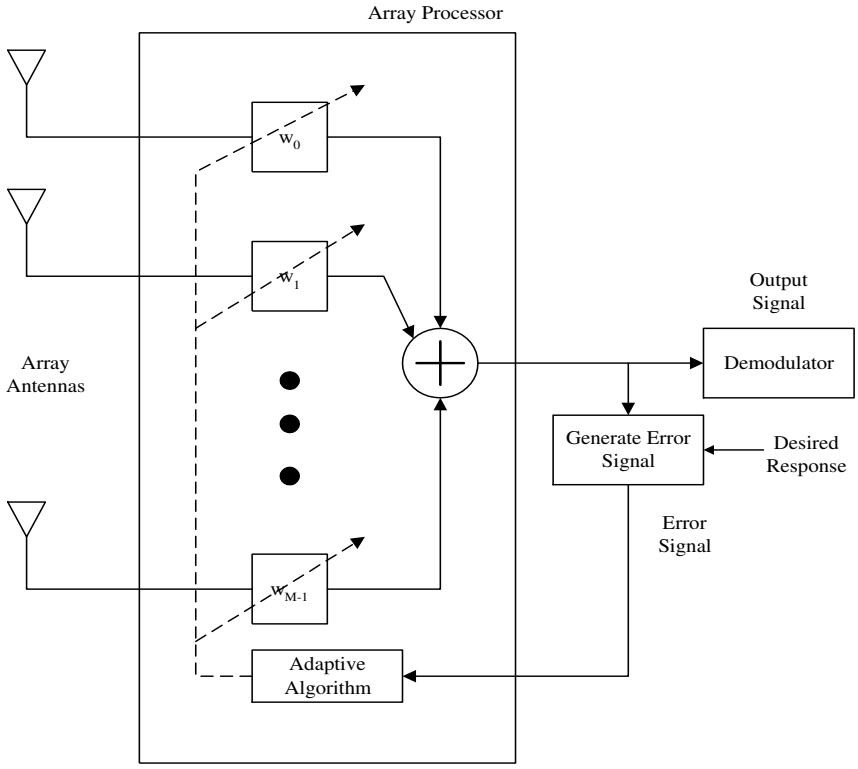

Figure 1.3 The smart antenna system.

the maximum signal-to-noise ratio (Max SNR), the linear constraint minimum variance distortionless response (LCMV) methods [12]. For the blind approach, the well-known constant modulus algorithm (CMA) is the most popular method. More details about the basic operation of the smart antennas can be found in [12]. The performance advantage of the blind approach is the enhanced bandwidth efficiency since no training signal is transmitted. However, this benefit comes at the expense of an additional complexity as well as the performance loss, in some cases.

1.2.3 Space-Time Modulation and Coding

Beside the MIMO communication systems, space-time modulation and coding are of interest and importance because they can provide an effective signalling and codes that can achieve a full diversity gain. Since the signal design extends over both space (via the multiple antennas) and time (via multiple symbol times), it is typically referred to as a *space-time code*. Most space-time codes are designed for quasi-static channels where the channel is constant over a block of certain symbol times, and the channel is assumed unknown at the

transmitter.

Optimal decoding of the received signal requires maximum likelihood (ML) demodulation. If the symbols modulated onto each of the L_t-transmit antennas are chosen from an alphabet of size $|\Upsilon|$, then because of the cross-coupling between transmitted symbols at the receiver antennas, ML demodulation requires an exhaustive search over all $|\Upsilon|^{L_t}$ possible input vector of L_t symbols.

It has been shown in [13] that the pairwise error probability decreases as $\text{SNR}^{L_\Delta L_r}$, where Δ denotes the $L_t \times L_r$ difference matrix between any two code words and L_Δ is the rank of Δ. The maximum achievable diversity gain through coherent combining of L_t-transmit and L_r-receive antennas is $L_t L_r$. Thus, to obtain this maximum diversity gain, the space-time code must be designed such that Δ has full rank equal to L_t. This design criterion is referred to as the *rank criterion*. Another design criterion is the *determinant criterion*. It has been shown that a high coding gain [13] can be achieved by maximizing the minimum of the determinant of Δ over all input matrix pairs. By applying such criteria in designing the space-time code, hence, there are two major space-time codes: space-time trellis code and space-time block code. More details about how to design and analyze these space-time codes can be found in [13, 14].

As previously mentioned, it can be seen that the MIMO communication systems provide a significant performance enhancement to the wireless communications, including the increased rates through multiplexing gain, the enhanced error probability through diversity gain, and the cancellation of ISI and interference through smart antennas. At the first step, the MIMO communication systems were developed for the flat fading channels, whereby no ISI occurs. In practice, most channels are frequency selective, therefore, such systems could suffer from ISI. Furthermore, this ISI severely affects the performances of the MIMO communication systems. Hence, an equalizer in time domain is needed to mitigate such problem. However, the design of equalizer for the MIMO communication systems is quite complicated due to the nature of a multi-dimensional signal processing inherent in these systems. Alternatively, the multicarrier modulation technique is quite promising for mitigating such problem due to its good performance and simplicity for implementation. This technique can be directly applied to the MIMO communication systems, known as the MIMO-OFDM communication systems. In the next text, the multicarrier modulation is presented.

1.3 Multicarrier Modulation

The basic idea of multicarrier modulation is to divide the transmitted bitstream into many different substreams and send these over many different subchannels. Typically, the subchannels are orthogonal under ideal propagation conditions. The data rate on each of the subchannels is much less than the total data rate, and the corresponding subchannel bandwidth is much less than the total system bandwidth. The number of substreams is chosen to insure that each subchannel has a bandwidth less than the coherence bandwidth of the channel, so the subchannels experience relatively flat fading. Thus, the ISI on each subchannel is small. The subchannels in multicarrier modulation need not be contiguous, so a large continuous block of spectrum is not needed for high rate multicarrier communications. Moreover, multicarrier modulation is efficiently implemented digitally. In this discrete implementation, i.e. an OFDM system, the ISI can be completely eliminated through the use of a cyclic prefix.

Multicarrier modulation is currently used in many wireless systems. However, it is not a new technique; it was first used for military high frequency (HF) radios in the late 1950's and early 1960's. Starting around 1990, multicarrier modulation has been adopted in many diverse wired and wireless applications, including digital audio and video broadcasting in Europe, digital subscriber lines (DSL) using discrete multitone, and the most recent generation of wireless LANs. Multicarrier modulation is also a candidate for the air interface in next generation cellular systems. Multicarrier techniques are common in high data rate wireless systems with moderate to large delay spread, as they have significant advantages over time-domain equalization. In particular, the number of taps required for an equalizer with good performance in a high data rate system is typically large. Thus, these equalizers are highly complex. Moreover, it is difficult to maintain accurate weights for a large number of equalizer taps in a rapidly varying channel. For these reasons, most emerging high rate wireless systems use either multicarrier modulation or spread spectrum instead of equalization to compensate for ISI.

1.3.1 Data Transmission using Multiple Carriers

The simplest form of multicarrier modulation divides the data stream into multiple substreams to be transmitted over different orthogonal subchannels centered at different subcarrier frequencies. The number of substreams is chosen to make the symbol time on each substream much greater than the delay spread of the channel or, equivalently, to make the substream bandwidth less than the channel coherence bandwidth.

Consider a linearly-modulated system with data rate R and passband bandwidth B. The coherence bandwidth for the channel is assumed to be $B_c < B$, so the signal experiences frequency-selective fading. The basic premise of multicarrier modulation is to break this wideband system into N linearly-modulated subsystems in parallel, each with subchannel bandwidth $B_N = B/N$ and data rate $R_N \approx R/N$. For N sufficiently large, the subchannel bandwidth $B_N = B/N \ll B_c$, which insures relatively flat fading on each subchannel. This can also be seen in the time domain: the system time T_N of the modulated signal in each subchannel is proportional to the subchannel bandwidth $1/B_N$. So $B_N \ll B_c$ implies that $T_N \approx 1/B_N \gg 1/B_c \approx T_m$, where T_m denotes the delay spread of the channel. Thus, if N is sufficiently large, the symbol time is much bigger than the delay spread, so each subchannel experiences little ISI degradation. Typically, the bit stream is divided into N substreams via a serial-to-parallel converter. The n^{th} substream is linearly-modulated (typically via quadrature amplitude modulation (QAM) or phase shift keying modulation (PSK)) relative to the subcarrier frequency f_n and occupies passband bandwidth B_N.

The subchannels can be divided to be non-overlapping subchannels. However, this strategy is spectrally inefficient, and near-ideal low pass filters is required to maintain the orthogonality of the subcarriers at the receivers. Moreover, it requires N independent modulators and demodulators, which entails significant expense, size, and power consumption. On the other hand, the subchannels can be divided to be overlapping subchannels, which make use of the spectrum more efficiently. It can be shown that the minimum frequency separation required for subcarriers to remain orthogonal over the symbol interval $[0, T_N]$ is $1/T_N$ [6]. Typically, a set of sinusoidal function in conjunction with an appropriate baseband pulse shape is chosen to form a set of (approximately) orthonormal basis functions. Given this orthonormal basis set, even if the subchannels overlap, the modulated signals

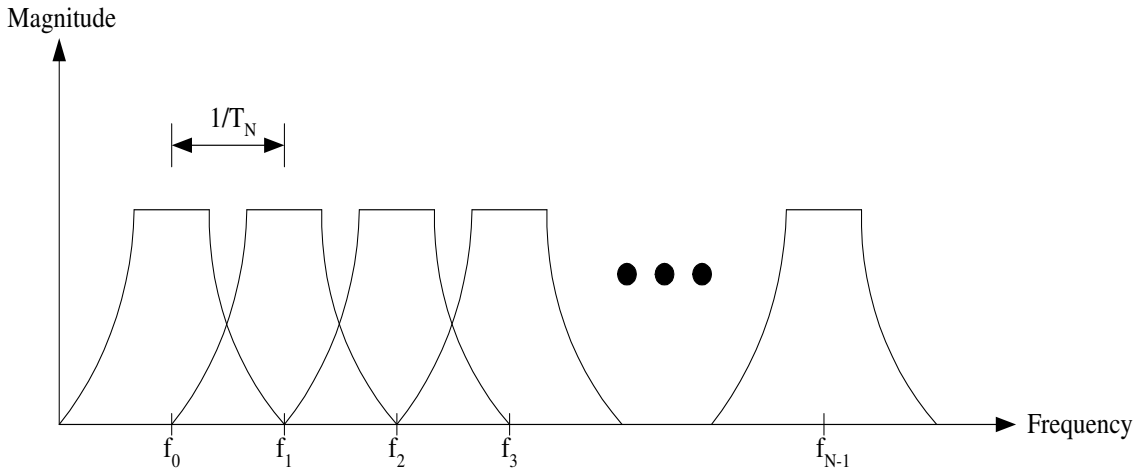

Figure 1.4 The frequency-domain multicarrier with overlapping subcarriers.

transmitted in each subchannel can be separated out in the receiver. In Fig.1.4, an illustration of the frequency-domain multicarrier with overlapping subcarriers is depicted. Note that $f_0, \ldots, f_{N-1}$ denote subcarriers of subchannels, respectively.

1.3.2 Discrete Implementation of Multicarrier

Although multicarrier modulation was invented in the 1950's, its requirement for separate modulators and demodulators on each subchannel was far too complex for most system implementations at the time. However, the development of simple and cheap implementations of the discrete Fourier transform (DFT) and the inverse DFT (IDFT) twenty years later, combined with the realization that multicarrier modulation can be implemented with these algorithms, ignited its widespread use.

Let $x[n],\ 0 \leq n \leq N-1$ be a discrete time input sequence. When the input data stream $x[n]$ is sent through a linear time-invariant discrete-time channel $h[n]$, the output $y[n]$ is the discrete-time convolution of the input and the channel impulse response, given as,

$$y[n] = h[n] * x[n] = \sum_k h[k]x[n-k]. \tag{1.2}$$

The N-point circular convolution of $x[n]$ and $h[n]$ is defined as

$$y[n] = h[n] \odot x[n] = \sum_k h[k]x[n-k]_N, \tag{1.3}$$

where $[n-k]_N$ denotes $[n-k]$ modulo N. In other words, $x[n-k]_N$ is a periodic version

of $x[n-k]$ with period N. It is easily verified that $y[n]$ in (1.3) is also periodic with period N. From the definition of the DFT, circular convolution in time leads to multiplication in frequency [6],

$$\text{DFT}\{y[n] = h[n] \odot x[n]\} = H[i]X[i], \ \leq i \leq N-1, \tag{1.4}$$

where $\odot$ denotes a circular convolution. Hence, if $H[i]$ is known, the data sequence $X[i]$ can be recovered by taking the IDFT of $Y[i]/H[i]$, which in turn, the original input sequence $x[n]$ is recovered. Unfortunately, the channel output is not a circular convolution but a linear convolution. However, the linear convolution between the channel input and channel impulse response can be turned into a circular convolution by adding a special prefix to the input called a *cyclic prefix*.

1.3.2.1 Cyclic Prefix

Consider a channel input sequence $x[n] = x[0], \ldots, x[N-1]$ of length N and a discrete-time channel with finite impulse response (FIR) $h[n] = h[0], \ldots, h[L]$ of length $L+1 = T_m/T_s$, where T_m denotes the the channel delay spread and T_s denotes the sampling time associated with the discrete time sequence. The cyclic prefix for $x[n]$ is defined as a $\{x[N-L], \ldots, x[N-1]\}$: it consists of the last L values of the $x[n]$ sequence. For each input sequence of length N, these last L samples are appended to the beginning of the sequence. This yields a new sequence $\tilde{x}[n], \ -L \leq n \leq N-1$, of length $N+L$, where $\tilde{x}[-L], \ldots, \tilde{x}[N-1] = x[N-L], \ldots, x[N-1], x[0], \ldots, x[N-1]$. Note that with this definition, $\tilde{x}[n] = x[n]_N$ for $-L \leq n \leq N-1$, which implies that $\tilde{x}[n-k] = x[n-k]_N$ for $-L \leq n-k \leq N-1$. At the receiver, the first L samples will be discarded in order to remove the redundancy resulted from the cyclic prefix.

1.3.2.2 Orthogonal Frequency Division Multiplexing

The OFDM implementation of multicarrier modulation, including a transmitter and receiver, is shown in Fig.1.5 and 1.6, respectively. The input data stream is modulated by a QAM modulator, resulting in a complex symbol stream $X[0], \ldots, X[N-1]$. This symbol stream is passed through a serial-to-parallel convertor, whose output is a set of N parallel QAM symbols $X[0], \ldots, X[N-1]$ corresponding to the symbols transmitted over each of the subcarriers. Thus, the N symbol output from the serial-to-parallel convertor are the

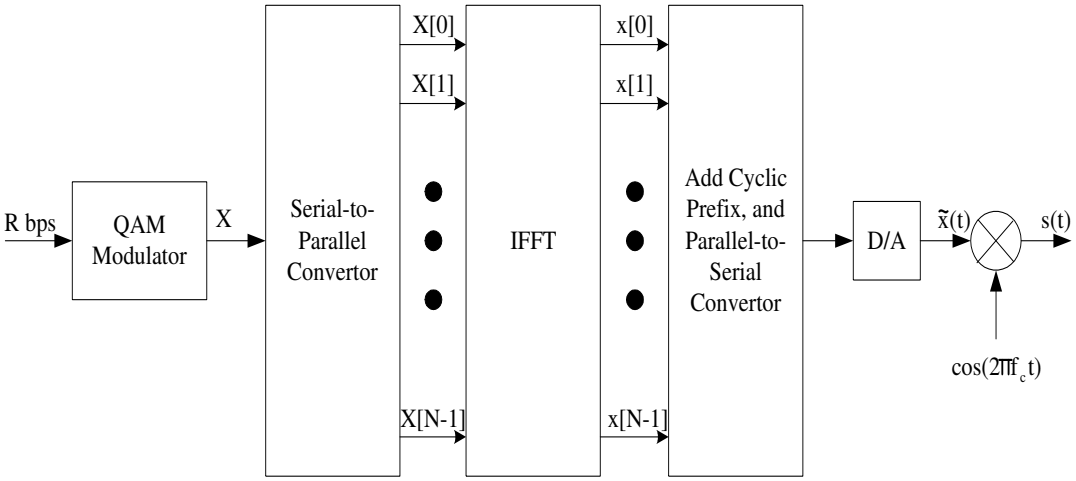

Figure 1.5 A transmitter of the OFDM system with IFFT/FFT implementation.

discrete frequency components of the OFDM modulator output $s(t)$. In order to generate $s(t)$, these frequency components are converted into time samples by performing an inverse DFT on these N symbols, which is efficiently implemented using the inverse fast Fourier transform (IFFT) algorithm. The IFFT yields the OFDM symbol consisting of the sequence $x[n] = x[0], \ldots, x[N-1]$ of length N, where

$$x[n] = \frac{1}{\sqrt{N}} \sum_{i=0}^{N-1} X[i] e^{j2\pi ni/N}, \ 0 \leq n \leq N-1, \tag{1.5}$$

where $j = \sqrt{-1}$. This sequence corresponds to samples of the multicarrier signal. The cyclic prefix is then added to the OFDM symbol, and the resulting time samples are ordered by the parallel-to-serial convertor and passed through a digital-to-analog (D/A) convertor, resulting in the baseband OFDM signal $\tilde{x}(t)$, which is then upconverted to frequency f_c.

The transmitted signal is filtered by the channel impulse response $h(t)$ and corrupted by the additive noise, so that the received signal is $y(t) = \tilde{x}(t) * h(t) + n(t)$. This signal is down converted to baseband and filtered to remove the high frequency components. The analog-to-digital (A/D) convertor samples the resulting signal to obtain $y[n] = \tilde{x}[n] * h[n] + n[n], \ -L \leq n \leq N-1$. The prefix of $y[n]$ consisting of the first L samples is then removed. This results in N time samples whose DFT in the absence of noise is $Y[i] = H[i]X[i]$. These time samples are serial-to-parallel converted and passed through a fast Fourier transform (FFT). This results in scaled versions of the original symbols $H[i]X[i]$, where $H[i] = H[f_i]$ is the flat-fading channel gain associated with the i^{th} subchannel. The FFT output is

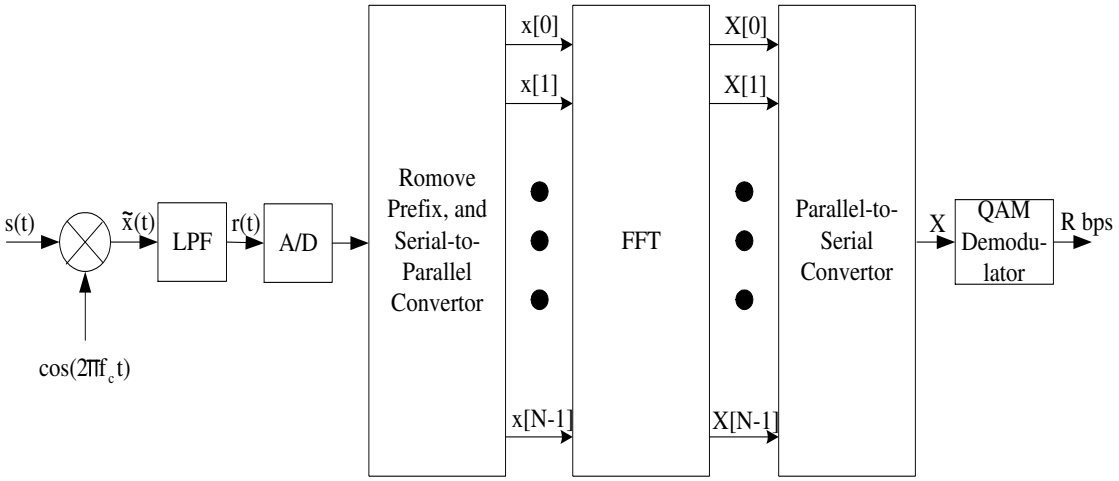

Figure 1.6 A receiver of the OFDM system with IFFT/FFT implementation.

parallel-to-serial converted and passed through a QAM demodulator to recover the original data, e.g. $X[i] = Y[i]/H[i]$.

1.4 Channel Estimation

For the wireless communication systems employing a coherent receiver, an accurate CSI is crucially needed. Thus, the issue of channel estimation is of most interest since the capacity of such systems as well as the error probability performance depends on this CSI estimate. An alternative way to cross over the channel estimation problem is to employ the differential modulation technique. However, this benefit of not explicitly performing the channel estimation comes at the expense of the 3-dB loss in a received SNR. In this section, an overview of channel estimation is presented. More specific details and approaches for channel estimation will be described in Chapter 3 and 4.

For the SISO communication systems, there are two ways to perform the channel estimation: blind channel estimation and non-blind channel estimation. Blind channel estimation doest not need any training (or pilot) signals for using as a prior information for channel estimation. Specifically, it actually exploits a special structure of the transmitted and received signals or the characteristics of channels, such as signal and noise subspaces of the received signal, a constant modulus property of the transmitted signal, and a cyclo-stationary property of the channels [15], for estimating the channels. The explicit benefit of the blind channel estimation is its enhanced bandwidth efficiency, since there is no bandwidth

efficiency loss caused by a transmission of training signals. However, the computational complexity of the blind channel estimation is a prohibitive cost. Moreover, when the dimensions of signal processing increases, e.g. as in the MIMO systems, the computational complexity of such channel estimation increases and cannot be affordable. On the other hand, non-blind channel estimation can be achieved by the use of the training signal. Despite the bandwidth efficiency loss, the non-blind channel estimation has several advantages. First, its computational complexity is not that high, in comparison to that of blind channel estimation, and can be affordable even for the MIMO systems. Second, its performance in terms of a mean square error (MSE) is excellent, mostly better than the that of blind channel estimation. Hence, the non-blind channel estimation is of particular interest. There are two approaches for designing the training signal: pilot-symbol assisted modulation (PSAM) approach [16] and pilot-embedding approach [17].

In the PSAM approach, the training signal is time-multiplexing onto the transmit data stream. At the receiver, this training signal is extracted from the received signal, and then is used for channel estimation. The interpolation technique can be adopted for improving an accuracy of the channel estimate. In summary, an extra time-slot is needed for sending this training signal, resulting in the bandwidth efficiency loss. In addition, this loss is proportional to the amount of the training signal used.

Alternatively, in the pilot-embedding approach, sequences of the training and data are added up together to form the transmit data stream. At the receiver, such soft estimation algorithms, e.g. Viterbi's algorithm, are used for recovering such training signal, and then, estimating the channels. The benefit of the pilot-embedding approach is the enhanced bandwidth efficiency, however, at the price of an increased computational complexity for channel estimation. Moreover, since these sequences are added up together, for a given power constraint, some power needs to be dedicated to the training. Hence, the power, i.e. the remaining power, dedicated to the data is then being reduced, resulting in an increasing error probability in the system.

There are many approaches for channel estimation, including a least square (LS) approach, an ML approach, and a linear minimum MSE (LMMSE) approach [18]. For the communication systems corrupted by the additive white Gaussian noise, the LS and ML channel estimation approaches behave similarly, and so does their performances [18]. For the

LMMSE channel estimation, a prior information about the channel correlation is exploited; as a result, its performance is the best [18]. However, this performance enhancement comes at the expense of the increased computational complexity of the estimation process. In addition, the approaches proposed for SISO systems can be well applied to the MIMO systems.

1.5 Multiuser Systems

In multiuser systems, the system resource must be divided among multiple users. It is well-know that signals of bandwidth B and time duration T occupy a signal space of dimension $2BT$. In order to support multiple users, the signal space of dimension $2BT$ of a multiuser system must be allocated to the different users. Allocation of signalling dimensions to specific user is called *multiple access*. Multiple access methods perform differently in different multiuser channels, and these methods will be applied to the two basic multiuser channels: downlink and uplink channels.

A multiuser channel refers to any channel that must be shared among multiple users. There are two different types of multiuser channels: the downlink and uplink channels. A downlink channel, also called a broadcast channel or forward channel, has one transmitter sending to many receivers. Since the signals transmitted to all users originate from the downlink transmitter, the transmitted signal is the sum of signals transmitted to all K users. Thus, the total signalling dimensions and power of the transmitted signal must be divided among the different users. Another important characteristic of the downlink is that both signal and interference are distorted by the same channel. An uplink channel, also called a multiple access channel or reverse channel, has many transmitters sending signals to one receiver, where each signal must be within the total system bandwidth B. In addition, the signals of different users in the uplink travel through different channels, the received powers associated with the different users will be different if their channel gains are different.

1.5.1 Multiple Access

Efficient allocation of signalling dimensions between users is a key design aspect of both uplink and downlink channels, since bandwidth is usually scarce. When dedicated channels are allocated to users, it is often called multiple access. Multiple access techniques

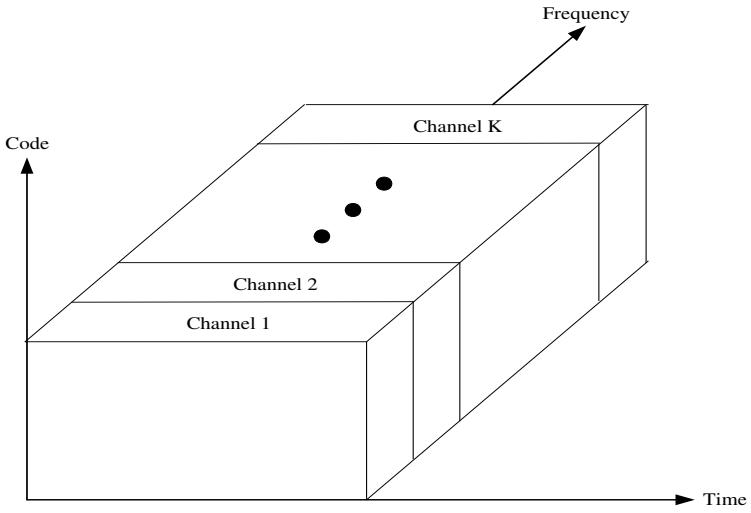

Figure 1.7 Frequency-Division Multiple Access.

divide up the total signalling dimensions into channels and then assign these channels to different users. The most common methods to divide up the signal space are along the time, frequency, and code axes. The different user channels are then created by an orthogonal or non- orthogonal division along these axes: frequency-division multiple access (FDMA) and time-division multiple access (TDMA) are orthogonal channelization methods whereas code-division multiple access (CDMA) can be orthogonal or non- orthogonal, depending on the code design.

1.5.1.1 Frequency-Division Multiple Access

In FDMA, the system signalling dimensions are divided along the frequency axis into nonoverlapping channels, and each user is assigned a different frequency channel, as shown in Fig.1.7. FDMA is the most common multiple access option for analog communication systems, where transmission is continuous. Multiple access in OFDM systems, called orthogonal frequency-division multiple access (OFDMA), implements FDMA by assigning different subcarriers to different users.

1.5.1.2 Time-Division Multiple Access

In TDMA, the system dimensions are divided along the time axis into nonoverlapping channels, and each user is assigned a different cyclically-repeating time slot, as shown in Fig.1.8. These TDMA channels occupy the entire system bandwidth, which is typically

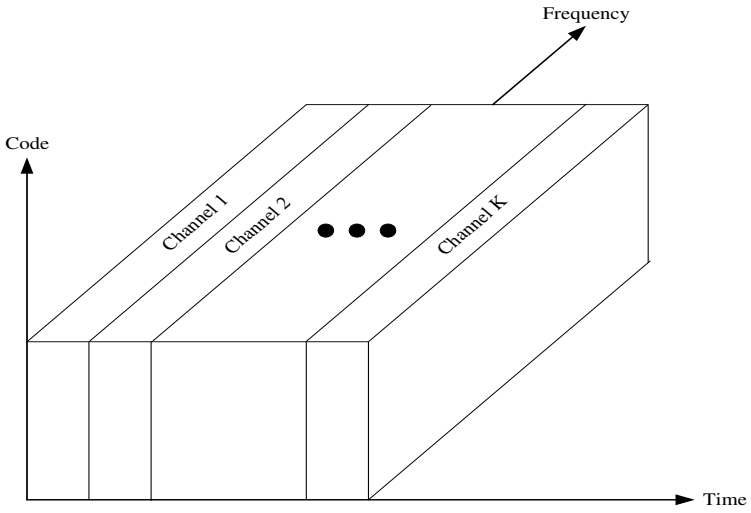

Figure 1.8 Time-Division Multiple Access.

wideband, so some form of ISI mitigation is required. A major difficulty of TDMA is the requirement for synchronization among different users in the uplink channels. To maintain orthogonal time slots in the received signals, the different uplink transmitters must synchronize such that after transmission through their respective channels, the received signals are orthogonal in time. Multipath can also destroy time-division orthogonality in both downlinks and uplinks if the multipath delays are a significant fraction of a time slot. TDMA is used in many digital cellular phone standards.

1.5.1.3 Code-Division Multiple Access

In CDMA, the information signals of different users are modulated by orthogonal or non-orthogonal spreading codes. The resulting spread signals simultaneously occupy the same time and bandwidth, as shown in Fig.1.9. The receiver uses the spreading code structure to separate out the different users. CDMA is used for multiple access in IS-95 digital cellular standards, with orthogonal spreading codes on the downlink and a combination of orthogonal and non-orthogonal codes on the uplink. It is also used in the wideband CDMA (W-CDMA) and CDMA 2000 digital cellular standards.

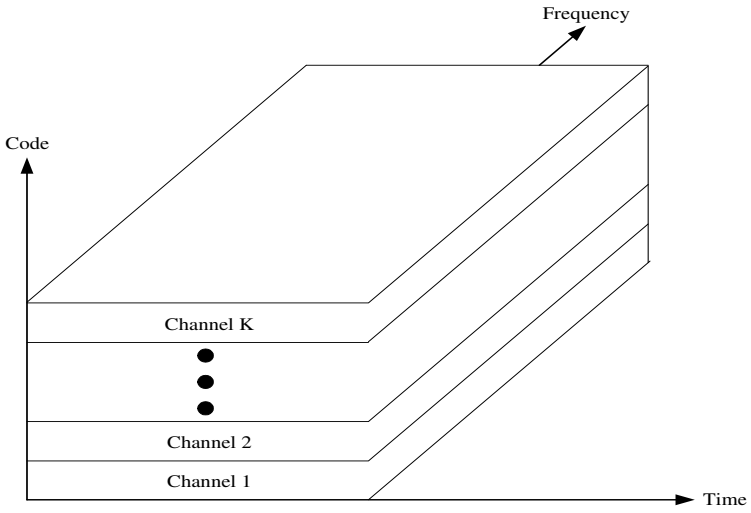

Figure 1.9 Code-Division Multiple Access.

1.6 Motivations and Scope of This Dissertation

In the future wireless communications, high data rate transmission services are highly demanded. As mentioned earlier, one of the promising communication schemes making such demand a reality is the MIMO communication system. In addition, several gains including multiplexing, diversity, and directionality gains inherent in the MIMO communication systems can significantly improve the system performances, e.g. the system capacity, the error probability, and the robustness to the interference. These performance advantages are the motivations for this dissertation. In this dissertation, the MIMO communication systems are considered. This dissertation studies the MIMO communication systems in two aspects: smart antenna system (or spatial interference cancellation scheme) and channel estimation.

It is well-known that the multiple access interference (MAI) can severely affect the performance of a CDMA system. Typically, the received signal consists of both the desired and the interference signals coming from different directions of arrival (DOA). Hence, the smart antenna system, i.e. a spatial filter, can be used to mitigate such interference by rejecting it as well as maintaining the desired signal in the desired direction. The advantages by employing such a system are the capacity improvement, the signal link enhancement, and the enhanced error probability. In the first part of this dissertation, the smart antenna system (or the spatial interference cancellation scheme), namely an interference-rejected

blind array processing (IRBAP), is proposed for interference canceling receivers in direct sequence (DS) CDMA systems. IRBAP only exploits the spreading codes of users as the information for its weight adjustment procedures. This proposed scheme is robust to the closely-separated-DOA in-beam interference signals, especially in the near-far effect situation. The theoretical analysis, including convergence analysis and error probability analysis, for IRBAP is conducted. Performance evaluation via computer simulations is also performed.

For the wireless communication systems employing coherent receivers, an accurate channel estimate is crucially needed. This demand motivates the studies in the second part of this dissertation. In the second part of this dissertation, channel estimation for the MIMO communication systems is investigated.

Firstly, the channel estimation for the MIMO communication systems with flat fading channels is considered. The novel pilot-embedding technique, called a data-bearing approach for pilot-embedding for joint channel estimation and data detection, is proposed by exploiting the null-space property and the orthogonality property of the data-bearer and pilot matrices. The unconstrained ML and LMMSE channel estimators are proposed. The ML data detection is also studied. MSE of channel estimation, Cramer-Rao lower bound (CRLB), and Chernoff's bound of bit error rate (BER) for space-time (ST) codes are analyzed for examining the performance of the proposed scheme. The optimum power allocation scheme for data and pilot parts is also investigated. Three data-bearer and pilot structures, including time-multiplexing (TM)-based, ST-block code (STBC)-based, and code-multiplexing (CM)-based, are proposed. Computer simulations are conducted for evaluating the performance of the proposed scheme.

Secondly, the channel estimation for the MIMO-OFDM communication systems with frequency-selective fading channels is considered. Since the multipath delay profile of such channels is arbitrary in such system, an effective channel estimator is needed. The generalization of a data-bearing approach for pilot-embedding to such system is proposed. The pilot-embedded data-bearing (PEDB) LS channel estimation and ML data detection are considered. Then, an LS FFT-based channel estimator is proposed to improve the performance of the PEDB-LS channel estimator. The effect of model mismatch error inherent in the proposed LS FFT-based channel estimator when considering non-integer

multipath delay profiles, and the performance analysis for such estimators are investigated, Under the framework of pilot embedding, an adaptive LS FFT-based channel estimator is proposed to improve the performance of that of LS FFT-based channel estimator. The optimum number of taps for this estimator is determined. Computer simulations are conducted for examining the performance of the proposed channel estimators.

In addition, the data-bearing approach for pilot embedding can be directly applied to the SISO communication system as well.

1.7 Outline

In chapter 2, the smart antenna system, i.e. IRBAP, is proposed for interference canceling receivers in DS-CDMA systems with flat-fading channels. In addition, the basic background for the interference canceling receivers and the basic blind beamforming is reviewed. Theoretical analysis, including convergence analysis and error probability analysis, for IRBAP is conducted. Performance evaluation via computer simulations is also performed. The results are summarized and discussed in the end of this chapter.

In chapter 3, a data-bearing approach for pilot-embedding frameworks for joint channel estimation and data detection in space-time coded MIMO systems with flat fading channels is proposed. The unconstrained ML and LMMSE channel estimators, and the ML data detection, are also proposed. MSE of channel estimation, CRLB, and Chernoff's bound of BER for ST codes are analyzed. The optimum power allocation scheme for data and pilot parts is also investigated. Three data-bearer and pilot structures, including TM-based, STBC-based, and CM-based, are proposed. Computer simulations are conducted for evaluating the performance of the proposed scheme. The results are summarized and discussed in the end of this chapter.

In chapter 4, the generalization of the data-bearing approach for pilot-embedding to the space-frequency coded MIMO-OFDM systems with frequency-selective fading channels is proposed. The PEDB-LS, LS FFT-based, and adaptive LS FFT-based channel estimators are proposed. In addition, the PEDB-ML data detection is also considered. The performance analysis for such channel estimators is conducted. Computer simulations are performed for examining the performance of the proposed channel estimators. The results are summarized and discussed in the end of this chapter.

In chapter 5, the dissertation is concluded, and the contributions of this dissertation as well as the future works are also mentioned.

1.8 Notation

For ease of later use, let $(\cdot)^T$ stands for the transpose of a matrix, $(\cdot)^*$ stands for the complex conjugate, $(\cdot)^H$ stands for the complex-conjugate transpose of a matrix, $tr\{\cdot\}$ stands for the trace of a square matrix, $(\cdot)^{-1}$ stands for a square matrix inversion, $\mathbf{I}$ stands for an identity matrix, and $\mathbf{0}$ stands for an all-zero-element matrix. In addition, bold character stands for a column vector, e.g. $\mathbf{x}$, and bold capital character stands a matrix, e.g. $\mathbf{X}$. List of all abbreviations are also illustrated in Appendix A.

CHAPTER II

AN INTERFERENCE-REJECTED BLIND ARRAY PROCESSING FOR INTERFERENCE CANCELING RECEIVERS IN CDMA SYSTEMS

This chapter presents the smart antenna system (or the spatial interference cancellation scheme) for DS-CDMA systems using a blind array processing, i.e. a blind beamforming. The basic background for the blind beamforming schemes in DS-CDMA systems are reviewed. Then the proposed smart antenna system, i.e. IRBAP, is presented. Furthermore, the performance analysis for IRBAP including convergence analysis, bit error rate analysis, and complexity comparison is also provided. For illustrating the performance of IRBAP, the simulation results in comparison with the analytical results are shown. In addition, the discussion and concluding remark are given in the end of this chapter.

2.1 Introduction

Many interference cancellation techniques have recently been proposed for wireless communications [19--26], where the smart antenna system or the beamforming is one of the most attractive and effective techniques. This technique plays a role of spatial filtering, where the received signal can be seen as a combination of users' plane waves impinging on an array antenna from different directions; as a result, the desired signal can be captured as well as the interference signals can be rejected by the selectivity and nulling capabilities of an array antenna [27].

The most important component of the smart antenna system is the adaptive algorithm used for adjusting the weight vectors. Different algorithms can be categorized as non-blind adaptive algorithms, where the receiver uses a pilot signal sent by the transmitter for its weight adjustment, and blind adaptive algorithms, where the receiver adjusts its weight vectors without using the pilot signal. The advantage of non-blind adaptive algorithm is low

computational complexity; however, this benefit comes at the price of channel bandwidth efficiency [12]. Consequently, the blind algorithm is more attractive than the non-blind adaptive algorithm for the benefit of no need of pilot signals, and hence, the bandwidth efficiency will be enhanced. Of particular interest in this chapter is to design the effective blind adaptive beamforming with an achievable low complexity.

One main class of blind adaptive algorithms in the literatures [24, 28--31] exploits the constant modulus property of the received signals. The idea is to capture the strongest constant modulus signal first and then subtract this captured signal from the overall received signals. Then in the next stage it will continue to capture the remaining signals and operate successively until the weakest signal is captured. This idea can be applied for multiuser detection purpose as well [32]. In a DS-CDMA system, several blind adaptive algorithms have been proposed, such as the Decision-Directed (DD) method, the CMA method, and the Despread-Respread (DR) method along with the LS technique [12, 33, 34]. These algorithms work well in the situation where power control is perfect and DOAs are well separated. However, in the near-far effect situations with closely separated DOAs, these algorithms fail to capture the desired signal because they do not have any interference cancellation processes for canceling the MAI. In addition, the blind adaptive beamforming exploiting 2-D RAKE receivers was proposed in [35--37]. Despite its capabilities of constructively combining the energy of desired signals coming from different DOAs and time delays while canceling the interference signals coming from the other DOAs, this scheme also suffers from the closely-separated-DOAs interference signals, relative to the desired signal's DOAs, under the near-far effect situations because of insufficiency of antenna array's degree of freedom. However, it works well in the well-separated-DOAs situation.

The interference canceling receivers using a blind array processing in the DS-CDMA system have been proposed in [19, 38], where the former proposed the optimum weight vector selection and the latter applied this receiver in the multipath environment. The iterative approach has been proposed in [19, 21], where the latter proposed to combine the parallel interference cancellation in order to cancel in-beam interference signals. One disadvantage of this iterative approach is that the user orders must be arranged from the strongest user to the weakest one. Consequently, this approach can not be suitably realized in the practical situations where the channels keep changing and the power control can not be

performed perfectly. However, it works reasonably well in a situation where the DOAs are well separated and the receiver's stages have been arranged from the strongest user down to the weakest one. Nevertheless, it does not work well in near-far effect situations. The reason lies in its optimization approach that does not consider the effect of the interfering users' DOA situations in the system. Therefore, in order to solve such issues, the development of a new optimization approach that takes into account both the closely- and well-separated-DOA situations is needed.

A goal of this chapter is to develop a blind beamforming scheme for interference canceling receivers in the DS-CDMA systems [22] which can resolve the near-far effect situation in both the closely- and well-separated-DOA situations without using pilot signals, and relax the user-power arrangement constraint. This chapter is organized as follows. In section 2.2, a signal model of the system is described. In section 2.3, interference canceling receivers are presented. In section 2.4, a basic blind beamforming for interference canceling receivers in CDMA systems is reviewed. In section 2.5, a blind beamforming for interference canceling receivers, i.e. IRBAP, is proposed; and an analysis of an LCMV optimum weight vector, convergence analysis, probability of error analysis, and complexity comparison and suboptimum approach are carried out. In section 2.6, the simulation results under several situations are shown, and the concluding remark is given in section 2.7.

2.2 Signal Model

Let consider a K-user DS-CDMA system where each user transmits data over a passband channel and the channel bandwidth is large enough in order to ignore the intersymbol interference. At the receiver, an M-element array antenna is used to receive the transmitted signals. The array antenna is assumed to operate in a frequency-nonselective slow-varying fading channel where the received signals at each element are identical except for phases. This channel model is valid when multipath reflectors are in the far field, relative to the receiver array antenna, [39, 40]. The model of the received signals is as follows [19, 25]:

$$\mathbf{x(t)} = \sum_{i} \sum_{k=1}^{K} \mathbf{a_k} h_k e_k b_{k,i} s_k(t - \tau_k - iT) + \mathbf{n(t)}, \tag{2.1}$$

where $\mathbf{x(t)} = [x_1(t), x_2(t), \ldots, x_M(t)]^T$ is the received signal vector at the M-element array antenna, $\mathbf{a_k} = [a_{1k}, a_{2k}, \ldots, a_{Mk}]^T$ is the steering vector for user k, e_k^2 is the received energy of the k^{th} user at each antenna element, $b_{k,i} \in \{-1, +1\}$ is the i^{th} symbol transmitted by user k, and h_k is the complex channel coefficient of the k^{th} user. And τ_k is the relative delay of the k^{th} user to the array reference, T is the symbol duration, and $\mathbf{n(t)}$ is the additive white Gaussian noise (AWGN) vector with zero-mean and variance σ^2 at the antenna elements.

The real-valued normalized signature waveforms $\{s_k(t)\}$,

$$s_k(t) = \sum_{n=0}^{P-1} s_{k,n} u(t - nT_c), \tag{2.2}$$

where $u(t)$ is the chip pulse waveform, P is the processing gain, and $T_c = \frac{T}{P}$ is the chip rate, are assumed to be linearly independent and with low cross-correlations.

In this chapter, the synchronous DS-CDMA case in which $\tau_k = 0$ is considered. Then sampling the received signals at the chip rate, the $M \times P$ received signal matrix can be expressed as follows:

$$\mathbf{X} = \sum_{k=1}^{K} \mathbf{a_k} h_k e_k b_k \mathbf{s}_k^T + \mathbf{N}. \tag{2.3}$$

For the sake of convenience, the time parameter t is omitted.

2.3 The Interference Canceling Receivers

A concept of interference canceling receivers [32] is employed to detect the user's symbol as shown in Fig.2.1. The interference canceling receivers operate successively and iteratively from the first stage, which captures the strongest signal, through the K^{th} stage, which captures the weakest signal. After capturing the desired signal at the j^{th} stage, the captured signal is then subtracted from the overall received signals $\mathbf{X}_{j-1}$ coming from the $(j-1)^{th}$ stage. The resulting signals of this subtraction are sent to the next stages, i.e. the $(j+1)^{th}$ stage and so on, consequently. The advantage of the interference canceling receivers compared with the joint multi-user detection, e.g. an MMSE receiver and a decorrelating receiver, is its simple structure that can be easily implemented [32]. In each stage of the interference canceling receivers, the blind beamforming or IRBAP is employed as the receiver described as follows.

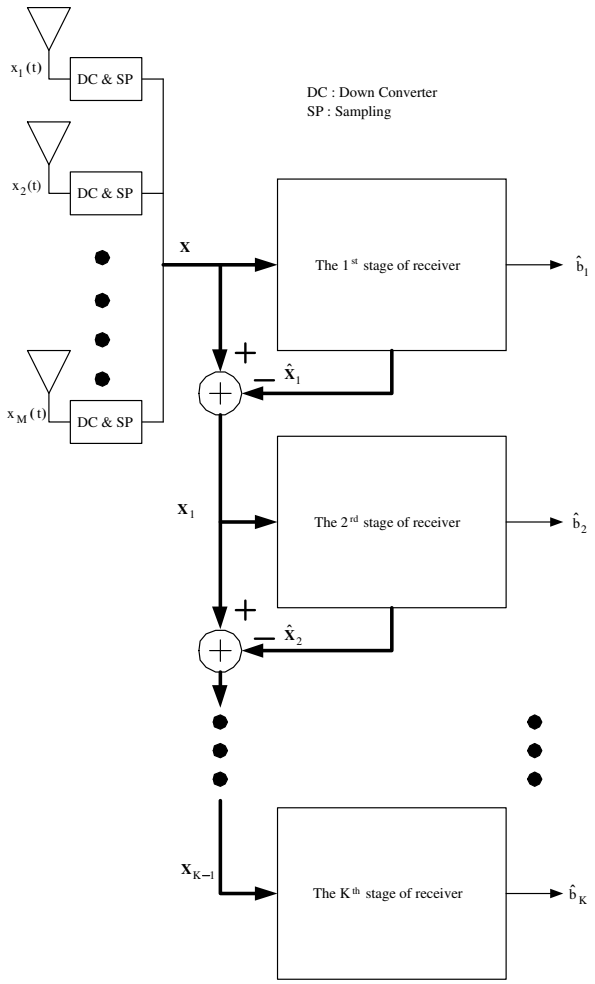

Figure 2.1 Block diagram of the successive interference canceling receivers

2.4 The Basic Blind Beamforming for Interference Canceling Receivers in DS-CDMA Systems

First of all, the basic blind beamforming without a channel equalizer for interference canceling receivers in DS-CDMA systems is reviewed. For this simple scenario, the channel is assumed static for a certain period of time, hence, the AWGN is only one source of noises and distortion in the systems. For the sake of exposition, at the first step of the state-of-the-art research, the channel gain is assumed to be unity, i.e. $h_k = 1,\ k = 1, \ldots, K$. The j^{th} stage of the basic blind beamforming without a channel equalizer for interference canceling receivers in DS-CDMA systems is illustrated in Fig.2.2.

Referring to [19], the decision variable y_j of the j^{th} stage, after down-converting, sampling, and matched-filtering processes, can be expressed as follows,

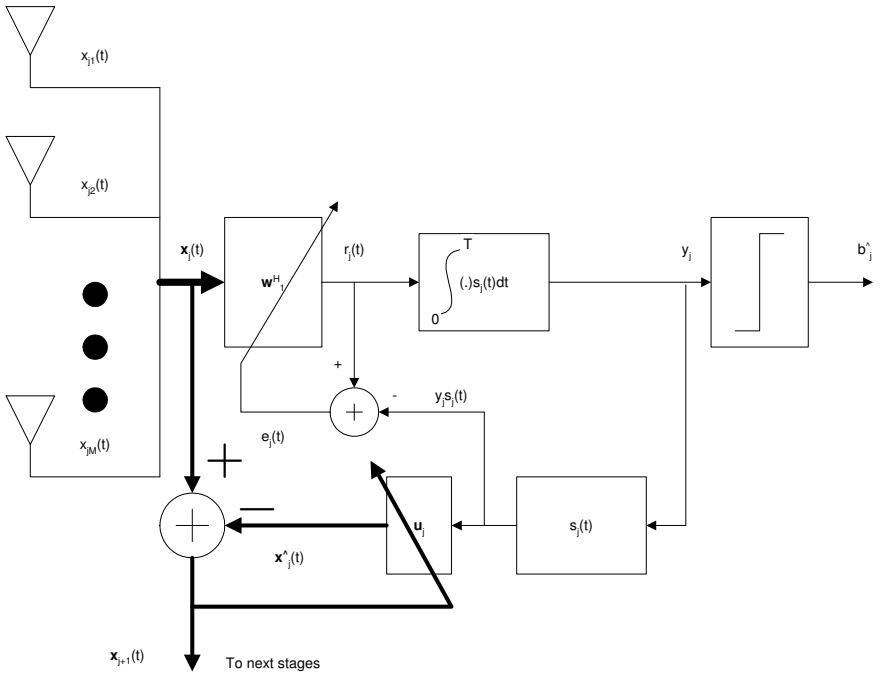

Figure 2.2: The j^{th} stage of a basic blind beamforming without a channel equalizer for interference canceling receivers

$$y_j = (\mathbf{w}_j^H \mathbf{a}_j) e_j b_j + \underbrace{\sum_{k=j+1}^{K} (\mathbf{w}_j^H \mathbf{a}_k) e_k b_k \rho_{jk}^s + \mathbf{w}_j^H \mathbf{N}_j \mathbf{s}_j}_{i_j}, \tag{2.4}$$

where $\mathbf{w}_j$ denotes a weight vector of the blind beamforming of the j^{th} stage, $\rho_{jk}^s = \int_0^T s_j(t) s_k(t) dt = \mathbf{s}_j^T \mathbf{s}_k$ denotes the cross-correlation between the signature waveforms j and k, $\mathbf{N}_j = \left(\mathbf{N}_1 - \sum_{l=1}^{j-1} i_l \mathbf{u}_l \mathbf{s}_l^T \right)$ denotes the $M \times P$ noise matrix of the j^{th} stage with $\mathbf{u}_l$ being a weight vector of the signal canceller of the l^{th} stage, and i_j denotes the MAI plus noises at the output of the j^{th} stage detector. The j^{th} stage input received signal matrix can be expressed as follows,

$$\mathbf{X}_j = \sum_{k=j+1}^{K} \mathbf{a}_k e_k b_k \mathbf{s}_k + \mathbf{N}_j. \tag{2.5}$$

For the signal canceller, the optimization approach for optimally determining the weight vector $\mathbf{u}_j$ is based on a minimization approach. Specifically, the objective of such a minimization approach is to minimize a squared-norm of the output received signal matrix $\mathbf{X}_{j+1}$ described as,

$$\min_{\mathbf{u}_j} tr \left\{ \mathrm{E} \left[\mathbf{X}_{j+1} \mathbf{X}_{j+1}^H \right] \right\} = \min_{\mathbf{u}_j} tr \left\{ \mathrm{E} \left[\left(\mathbf{X}_j - y_j \mathbf{u}_j \mathbf{s}_j^T \right) \left(\mathbf{X}_j - y_j \mathbf{u}_j \mathbf{s}_j^T \right)^H \right] \right\}. \tag{2.6}$$

After some algebraic manipulations, the closed form solution to (2.6) can be expressed as,

$$\mathbf{u}_j = \frac{\mathbf{R}_{s_j'}\mathbf{w}_j}{\mathbf{w}_j^H \mathbf{R}_{s_j'}\mathbf{w}_j}, \tag{2.7}$$

where $\mathbf{R}_{s_j'} = \mathrm{E}\left[\mathbf{X}_j \mathbf{s}_j \mathbf{s}_j^T \mathbf{X}_j^H\right]$.

For the blind beamforming, there are two optimization approaches for optimally determining the weight vector $\mathbf{w}_j$ summarized as follows.

2.4.1 Minimization Approach

From Fig.2.2, the error vector $\mathbf{e}_j$, that is a performance measure obtained by taking the difference between the spatially-matched received signal vector $\mathbf{r}_j$ and the reference signal vector $y_j\mathbf{s}_j$, can be expressed as,

$$\mathbf{e}_j^H = \mathbf{w}_j^H \mathbf{X}_j - (\mathbf{w}_j^H \mathbf{X}_j \mathbf{s}_j)\mathbf{s}_j^T = \mathbf{w}_j^H \mathbf{X}_j (\mathbf{I} - \mathbf{s}_j \mathbf{s}_j^T). \tag{2.8}$$

This optimization approach is based on the MMSE criterion of the error vector $\mathbf{e}_j$ expressed as follows,

$$\min_{\mathbf{w}_j} \mathrm{E}\left[\mathbf{e}_j^H \mathbf{e}_j\right] \qquad \text{subject to} \qquad \mathrm{E}\left[|y_j|^2\right] = 1, \tag{2.9}$$

where $\mathrm{E}\left[\mathbf{e}_j^H \mathbf{e}_j\right] = \mathbf{w}_j^H (\mathbf{R}_j - \mathbf{R}_{s_j'})\mathbf{w}_j$ with $\mathbf{R}_j = \mathrm{E}\left[\mathbf{X}_j \mathbf{X}_j^H\right]$, and $\mathrm{E}\left[|y_j|^2\right] = \mathbf{w}_j^H \mathbf{R}_{s_j'} \mathbf{w}_j$.

It is well known that a solution to (2.9) is the generalized eigenvector that corresponds to the smallest eigenvalue λ_{min} of the matrix pencil $(\mathbf{R}_j, \mathbf{R}_{\mathbf{s_j'}})$ described as follows,

$$\mathbf{R}_j \mathbf{w}_j = \lambda_{min} \mathbf{R}_{s_j'} \mathbf{w}_j. \tag{2.10}$$

2.4.2 Maximization Approach

An alternative way to obtain another optimum weight vector $\mathbf{w}_j$ is to employ the maximization approach, in which the output power of the decision variable y_j is maximized subject to a unit norm constraint for the weight vector $\mathbf{w}_j$. Mathematically, this maximization objective function can be described as follows,

$$\max_{\mathbf{w}_j} \mathrm{E}\left[|y_j|^2\right] = \mathbf{w}_j^H \mathbf{R}_{s_j'} \mathbf{w}_j \qquad \text{subject to} \qquad \mathbf{w}_j^H \mathbf{w}_j = 1. \tag{2.11}$$

Similarly, it is well known that the solution to (2.11) is the generalized eigenvector that corresponds to the largest eigenvalue λ_{max} of the matrix $\mathbf{R}_{s_j'}$ described as follows,

$$\mathbf{R}_{s_j'}\mathbf{w}_j = \lambda_{max}\mathbf{w}_j. \tag{2.12}$$

Since the environment keeps changing, e.g. the slow varying fading channels, an adaptive approach is more preferable. The stochastic gradient-based algorithms such as the least mean square (LMS) and the recursive least square (RLS) approaches can be employed for this adaptive approach. The normalized LMS algorithm for the weight vector $\mathbf{u}_j$ in (2.7) can be described as follows,

$$\mathbf{u}_j(n+1) = \mathbf{u}_j(n) + \mu_1 y_j^*(n)\frac{\mathbf{X}_{j+1}(n)}{\|\mathbf{X}_{j+1}(n)\|}\mathbf{s}_j, \tag{2.13}$$

where μ_1 denotes a step size and n denotes the iteration index.

The LMS algorithm in conjunction with a quadratic constraint for the weight vector $\mathbf{w}_j$ in (2.10) can be described as follows,

$$\mathbf{w}_j(n+1) = \mathbf{w}_j(n) + \mu_2 y_j^*(n)\left(\mathbf{X}_j(n)\mathbf{X}_j^H(n)\right)^{-1}\mathbf{X}_j(n)\mathbf{s}_j, \tag{2.14}$$

where μ_2 denotes a step size. Similarly, the LMS algorithm in conjunction with a quadratic constraint for the weight vector $\mathbf{w}_j$ in (2.12) can be described as follows,

$$\mathbf{w}_j(n+1) = \mathbf{w}_j(n) + \mu_3 y_j^*(n)\mathbf{X}_j(n)\mathbf{s}_j, \tag{2.15}$$

where μ_3 denotes a step size.

2.5 The Interference-Rejected Blind Array Processing for Interference Canceling Receivers in DS-CDMA Systems

The first stage IRBAP is shown in Fig.2.3, and its operation is described as follows. The IRBAP consists of three main parts: a blind array processing which is controlled by a weight vector $\mathbf{w}_1$, a signal canceler which is controlled by a weight vector $\mathbf{u}_1$, and a $(K-1)$-block interference rejection part. After spatially filtering the overall received signal matrix $\mathbf{X}$ by the weight vector $\mathbf{w}_1^H$, the spatially filtered signal $\mathbf{r}_1^H$ is then matched by the spreading sequence $\mathbf{s}_1$ of the first user in order to capture the first user's signal. This matched-filter output y_1 is then respread again by the first user's spreading sequence $\mathbf{s}_1$

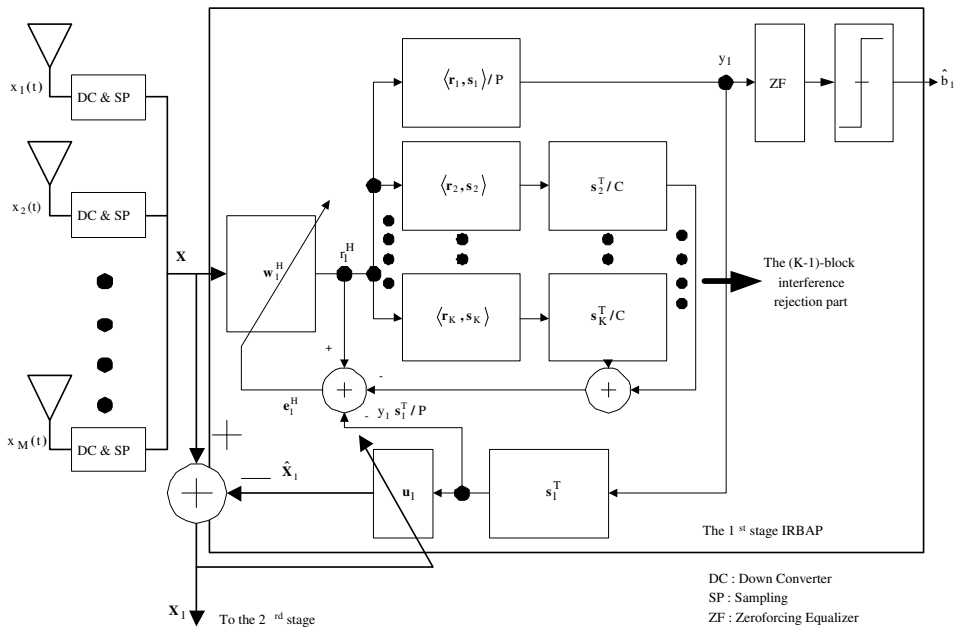

Figure 2.3 An Interference-Rejected Blind Array Processing for interference canceling receivers

in order to form the reference signal used to compare with the spatially filtered signal $\mathbf{r}_1^H$ for constructing an error signal $\mathbf{e}_1^H$. This error signal is used for the optimization process for finding the optimal weight vector $\mathbf{w}_1$ of a blind array processing. In addition, the first user's respread signal is also multiplied by the signal canceller's weight vector $\mathbf{u}_1$ and then subtracted from the overall received signal matrix $\mathbf{X}$ in order to eliminate an influence of the first user's captured signal in this overall received signal matrix, before this overall received signal matrix is being sent to the second stage. A concept of parallel interference cancellation for the $(K-1)$-block interference rejection part is employed as shown in Fig.2.3. The basic idea is that if the signature sequences of all users are assumed known to the system and the first user's signal at the first stage is being captured, other users' signal could be regarded as the interference signals, and hence, it has to be cancelled out from this stage. The $(K-1)$-block interference rejection part consists of $(K-1)$ blocks of the matched filter and the re-spreading block used to capture the interference signals and imitate these interference signals, respectively, by using the interfering users' signature sequence, e.g. $\mathbf{s}_2,\ \mathbf{s}_3, \ldots, \mathbf{s}_K$. Then these estimated interference signals are subtracted from the spatially filtered signal $\mathbf{r}_1^H$ resulting in rejecting the influence of MAI out of the error signal $\mathbf{e}_1^H$. Consequently, the weight vector adjustment process will operate without the effect of MAI. The j^{th} stage operates in a similar way as the first stage except the input received signals,

which is denoted by $\mathbf{X}_{j-1}$. The zeroforcing (ZF) equalizer [15] is employed, i.e. $\frac{1}{h_1}$, in order to compensate the channel effect, and a hard-limited detector is also employed as a detector. In addition, the channel coefficients are assumed perfectly known to the receiver. In practical applications, these channel coefficients will be estimated by using either the pilot or training, the known signal transmitted from the transmitter to the receiver, based channel estimation approach or the blind channel estimation approach [41, 42]. Throughout this chapter, the following assumptions are assumed.

- The synchronous DS-CDMA system is considered where each user transmits only at one direct path.
- The data symbols and the AWGN are mutually uncorrelated.
- The cross-correlation between each signature sequence is a small real-valued constant and the processing gain is much greater than this cross-correlation.
- The data symbol b_i is mutually uncorrelated and $\mathrm{E}[|b_i|^2] = 1$.

Similar to Fig.2.3, at the j^{th} stage, the matched-filter output y_j and the input received signal matrix $\mathbf{X}_j$, for the $(j+1)^{th}$ stage, can be described as follows,

$$y_j = \frac{1}{P}\int_0^T \mathbf{w}_j^H \mathbf{X}_{j-1} s_j(t) dt, \tag{2.16}$$

$$\mathbf{X}_j = \mathbf{X}_{j-1} - \mathbf{u}_j y_j \mathbf{s}_j^T, \tag{2.17}$$

where P is the processing gain or spreading factor. The error signal vector $\mathbf{e}_j^H$ in Fig.2.3 can be described as follows,

$$\mathbf{e}_j^H = \mathbf{w}_j^H \mathbf{X}_{j-1}[(\mathbf{I} - \frac{1}{C}\sum_{i\neq j} \mathbf{s}_i \mathbf{s}_i^T) - \frac{1}{P}\mathbf{s}_j \mathbf{s}_j^T], \tag{2.18}$$

where C is the real-valued parameter for adjusting the impact of the $(K-1)$-block interference rejection part. This is equivalent to the orthogonal projection of the weighted data vector onto the orthogonal subspace spanned by the temporal signatures of the desired and interference signals.

The problem to find the optimum weight vector of the blind array processing is a minimization problem since it is capable of placing null points toward the interfering users' DOA [19] as formulated below,

$$\min_{\mathbf{w}_j} \mathrm{E}[\mathbf{e}_j^H \mathbf{e}_j] \qquad \text{subject to} \qquad \mathrm{E}[|y_j|^2] = 1. \tag{2.19}$$

Substituting (2.18) into (2.19), the optimization problem can be rewritten as follows,

$$\min_{\mathbf{w}_j} \mathrm{E}[\mathbf{e}_j^H \mathbf{e}_j] = \mathbf{w}_j^H (\mathbf{R}_I - \frac{1}{P}\mathbf{R}_{s_j})\mathbf{w}_j \qquad \text{subject to} \qquad \frac{1}{P^2}\mathbf{w}_j^H \mathbf{R}_{s_j}\mathbf{w}_j = 1, \quad (2.20)$$

where $\mathbf{R}_I = \mathrm{E}[\mathbf{X}_{j-1}(\mathbf{I} - \frac{1}{C}\sum_{i\neq j}\mathbf{s}_i\mathbf{s}_i^T)\mathbf{X}_{j-1}^H]$ is the covariance matrix of the interference-rejected received signal matrix and $\mathbf{R}_{s_j} = \mathrm{E}[\mathbf{X}_{j-1}\mathbf{s}_j\mathbf{s}_j^T\mathbf{X}_{j-1}^H]$ is the covariance matrix of the matched received signal matrix.

The solution of this minimization problem is the well-known generalized eigenvector corresponding to the smallest eigenvalue of the matrix pencil $(\mathbf{R}_I, \frac{\mathbf{R}_{s_j}}{P})$, i.e. [19]

$$\mathbf{R}_I\mathbf{w}_j = \frac{\lambda_{min}}{P}\mathbf{R}_{s_j}\mathbf{w}_j. \quad (2.21)$$

Note that $\mathbf{R}_I$ contains the interference cancellation term, i.e. $(\mathbf{I} - \frac{1}{C}\sum_{i\neq j}\mathbf{s}_i\mathbf{s}_i^T)$, which is a major different between the proposed scheme and the existing work [19]. This interference cancellation term plays an important role in resisting the impact of the MAI in the near-far effect situation especially in the closely-separated-DOA situation. One can see that the constrained optimization in (2.20) is equivalent to the maximization problem that maximize the signal-to-interference-plus-noise (SINR) ratio given by [43, 44],

$$\text{SINR} = \frac{\mathbf{w}_j^H\mathbf{R}_{s_j}\mathbf{w}_j}{P^2(\mathbf{w}_j^H(\mathbf{R}_I - \frac{1}{P}\mathbf{R}_{s_j})\mathbf{w}_j)}, \quad (2.22)$$

by maintaining a distortionless array response to the desired signal, i.e. $\frac{1}{P^2}\mathbf{w}_j^H\mathbf{R}_{s_j}\mathbf{w}_j = 1$. In addition, the robust adaptive beamforming approaches for this maximization problem, in which the signal mismatch problem and steering vector errors are taken into account, have recently been investigated in [44--48]. In this chapter, the application of the blind adaptive beamforming to the DS-CDMA systems in the presence of the near-far effect and the in-beam interference signals is investigated. Since the environment keep changing due to the fading channel resulting in impossibly determining the exact $\mathbf{R}_I$ and $\mathbf{R}_{s_j}$ within a short period of time, the adaptive approach is prominently attractive to find the solution of (2.20). The LMS based adaptive algorithm with the quadratic constraint is given by [19, 48],

$$\mathbf{w}_j(n+1) \;=\; \mathbf{w}_j(n) + \mu[\mathbf{X}_{j-1}(n)(\mathbf{I} - \frac{1}{C}\sum_{i\neq j}\mathbf{s}_i\mathbf{s}_i^T)\mathbf{X}_{j-1}^H(n)]^{-1}\mathbf{X}_{j-1}(n)\mathbf{s}_j y_j^*(n) \quad (2.23)$$

where μ denotes the blind array processing's step size.

In a similar way to the blind array processing for interference canceling receivers [19], the optimum weight vector of the j^{th} signal canceller is determined by optimizing the

following unconstrained minimization problem

$$\arg\min_{\mathbf{u}_j} \mathrm{tr}\left\{\mathrm{E}[\mathbf{X}_j\mathbf{X}_j^H]\right\}, \tag{2.24}$$

with tr$\{\cdot\}$ being the trace of a matrix. The normalized LMS based adaptive algorithm is employed for the signal canceller in order to prevent a noise amplification when the input received signal matrix $\mathbf{X}_j$ is large as follows,

$$\mathbf{u}_j(n+1) = \mathbf{u}_j(n) + \mu_u \frac{\mathbf{X}_j(n)}{\|\mathbf{X}_j(n)\|}\mathbf{s}_j y_j^*(n), \tag{2.25}$$

where μ_u denotes the signal canceller's step size.

2.5.1 The Linear Constrained Minimum Variance Optimum Weight Vector

In this section, the LCMV optimum weight vector of the blind array processing and the corresponding optimum weight vector of signal canceller are derived for using as a benchmark in the convergence analysis and the simulation results.

Let define some parameters first: let $\rho_{i,j}^a = \frac{\mathbf{a}_i^H\mathbf{a}_j}{\|\mathbf{a}_i\|\|\mathbf{a}_j\|}$ be the correlation between the i^{th} and j^{th} user's array response vectors, and $n_j^{'} = \int_0^T \mathbf{w}_j^H\mathbf{N}s_j(t)dt$ be the matched AWGN at the j^{th} stage.

Let consider the matched filter output of the first stage given as

$$\begin{aligned} y_1 &= \frac{1}{P}\int_0^T \mathbf{w}_1^H\mathbf{X}s_1(t)dt \\ &= \mathbf{w}_1^H\mathbf{a}_1h_1e_1b_1 + i_1, \end{aligned} \tag{2.26}$$

where $i_1 = \frac{1}{P}\sum_{k=2}^K \mathbf{w}_1^H\mathbf{a}_kh_ke_kb_k\rho_{k,1}^s + \frac{n_1^{'}}{P}$ is the multiple access interference and noise term.

Canceling user 1 from the received signal matrix $\mathbf{X}$ in Fig.2.3, the input signal matrix for the second stage can be expressed as follows,

$$\begin{aligned} \mathbf{X}_1 &= \mathbf{X} - \mathbf{u}_1y_1\mathbf{s}_1^T \\ &= \underbrace{(\mathbf{a}_1 - \mathbf{u}_1\mathbf{w}_1^H\mathbf{a}_1)h_1e_1b_1\mathbf{s}_1^T}_{\mathbf{B}_1} + \mathbf{N} + \sum_{k=2}^K \mathbf{a}_kh_ke_kb_k\mathbf{s}_k^T - \mathbf{u}_1i_1\mathbf{s}_1^T. \end{aligned} \tag{2.27}$$

The matched filter output of the j^{th} stage, $j = 2, \ldots, K$, can be generally formulated as follows,

$$y_j = \mathbf{w}_j^H\mathbf{a}_jh_je_jb_j + i_j + \frac{1}{P}(\sum_{i=1}^{j-1}\mathbf{w}_j^H\mathbf{B}_i\mathbf{s}_j - \mathbf{w}_j^H\mathbf{u}_{j-1}Y_{j-1}\rho_{j-1,j}^s), \tag{2.28}$$

where

$$i_j = \frac{1}{P}\sum_{k=j+1}^{K} \mathbf{w}_j^H \mathbf{a}_k h_k e_k b_k \rho_{j,k}^s + \frac{n_j^{'}}{P} - \frac{1}{P}\sum_{i=1}^{j-1} i_i \mathbf{w}_j^H \mathbf{u}_i \rho_{j,i}^s \tag{2.29}$$

and the third term on the right hand side of (2.28) is the accumulated error caused by the signal cancellation operation and it is equal to zero if $j = 1$.

Let define the third term on the right hand side of (2.28) as Y_j where

$$Y_1 = 0,\ Y_2 = \frac{1}{P}\mathbf{w}_2^H \mathbf{B}_1 \mathbf{s}_2,\ \text{and}\ Y_j = \frac{1}{P}(\sum_{i=1}^{j-1} \mathbf{w}_j^H \mathbf{B}_i \mathbf{s}_j - \mathbf{w}_j^H \mathbf{u}_{j-1} Y_{j-1} \rho_{j-1,j}^s), \tag{2.30}$$

and

$$\mathbf{B}_j = (\mathbf{a}_j - \mathbf{u}_j \mathbf{w}_j^H \mathbf{a}_j) h_j e_j b_j \mathbf{s}_j^T. \tag{2.31}$$

From (2.28), the problem of interest can be formulated as finding the LCMV optimum weight vector of the blind array processing $\mathbf{w}_j^{LCMV}$ that solve the following linear-constrained minimization problem [49],

$$\min_{\mathbf{w}_j} \mathrm{E}\left[\|\mathbf{w}_j^H \mathbf{a}_j h_j e_j b_j\|^2\right] \qquad \text{subject to} \qquad \mathbf{w}_j^H \mathbf{a}_j = \|\mathbf{a}_j\|. \tag{2.32}$$

Intuitively, the objective of (2.32) is to minimize the variance of the desired signal while keeping the maximum array response to the direction of the desired signal's DOA. The solution of (2.32) is a well-known LCMV optimum solution given as

$$\mathbf{w}_j^{LCMV} = \frac{\mathbf{a}_j}{\|\mathbf{a}_j\|}. \tag{2.33}$$

Substituting (2.33) into (2.30), the corresponding optimum wight vector of the signal canceller $\mathbf{u}_j^{LCMV_{opt}}$ can be obtained by minimizing the MSE of the accumulated error Y_j, which is the dominant residue resulting from the signal cancellation operation in (2.28), as follows,

$$\min_{\mathbf{u}_j} \mathrm{E}\left[\|Y_j\|^2\right] \equiv \min_{\mathbf{u}_j} \mathrm{E}\left[\|\mathbf{B}_j\|^2\right] = \min_{\mathbf{u}_j} \mathrm{E}\left[\|(\mathbf{a}_j - \mathbf{u}_j \|\mathbf{a}_j\|) h_j e_j b_j \mathbf{s}_j^T\|^2\right]. \tag{2.34}$$

Obviously, the optimum solution for (2.34) that yields (2.34) to achieve its minimum value, which is zero, is given as

$$\mathbf{u}_j^{LCMV_{opt}} = \frac{\mathbf{a}_j}{\|\mathbf{a}_j\|}. \tag{2.35}$$

Note that (2.33) and (2.35) are also the optimum wight vectors of $\mathbf{w}_j$ and $\mathbf{u}_j$ in [19], respectively. Substituting (2.33) and (2.35) into (2.28) and (2.29), thus yielding

$$y_j^{LCMV} = \frac{\mathbf{a}_j^H \mathbf{a}_j}{\|\mathbf{a}_j\|} h_j e_j b_j + i_j = \underbrace{\|\mathbf{a}_j\| h_j e_j b_j}_{Signal} + \underbrace{i_j}_{Interference\ and\ noise}, \tag{2.36}$$

$$i_j \;=\; \frac{1}{P}\sum_{k=j+1}^{K}\|\mathbf{a}_k\|h_k e_k b_k \rho^s_{j,k}\rho^a_{j,k} + \frac{n_j^{'}}{P} - \frac{1}{P}\sum_{i=1}^{j-1} i_i \rho^s_{j,i}\rho^a_{j,i}. \tag{2.37}$$

Note that the LCMV optimum matched filter output y_j^{LCMV} consists of the desired signal and the MAI which depends on the cross-correlation of the array response as well as the cross-correlation of the signature sequences of the interfering users. Furthermore, it can be shown in the next section that (2.33) is also the solution to (2.20).

2.5.2 Convergence Analysis

In this chapter, the uniform linear array (ULA) is employed for the analysis and experiments. The array response vector of a half-wavelength M-element ULA arranged along the y-axis is formulated as follows,

$$\mathbf{a}_j = [1 \; e^{-j\alpha_j} \; e^{-2j\alpha_j} \; \ldots \; e^{-(M-1)j\alpha_j}]^T, \tag{2.38}$$

where $\alpha_j = \frac{2\pi d \sin\phi_j}{\nu} = \omega \sin\phi_j$ is the phase difference between each antenna element with ϕ_j being the DOA of the j^{th} user, d the inter-element spacing between each antenna element which is equal to a half-wavelength of the carrier frequency, and ν the wavelength of the carrier frequency. In this section, the convergence analysis of the weight vector of the blind array processing $\mathbf{w}_j$ in two different scenarios: the closely- and well-separated-DOA situations in the near-far effect environment is conducted. In addition, the result can apply directly to the balance power case, where all users' signals have the same power.

First of all, the underlying structure of the error signal (2.18) as well as the constraint of the optimization problem (2.20) have to be explored. Substituting (2.17), by using $\mathbf{u}_j$ in (2.35), into (2.18) and using the assumption (iii), in which it can approximate $\frac{\rho^s_{i,j}}{P} \approx 0, \; i \neq j$ without loss of generality, the optimization problem in (2.20) can be approximately expressed as follows,

$$\min_{\mathbf{w}_j} \mathrm{E}[\mathbf{e}_j^H \mathbf{e}_j] \;\approx\; \min_{\mathbf{w}_j}\{\sigma^2 \mathbf{w}_j^H [\mathrm{E}[\mathbf{N}\mathbf{N}^H] + \frac{K-3}{P}\mathrm{E}[\mathbf{N}(\sum_{i\neq j}\mathbf{s}_i\mathbf{s}_i^T)\mathbf{N}^H] + \mathrm{E}[\mathbf{N}\mathbf{s}_j\mathbf{s}_j^T\mathbf{N}^H]]\mathbf{w}_j\}. \tag{2.39}$$

From the fact that $\mathrm{E}[\mathbf{N}\mathbf{N}^H] = P\mathbf{I}$, $\mathrm{E}[\mathbf{N}\mathbf{s}_j\mathbf{s}_j^T\mathbf{N}^H] = P\mathbf{I}$, $\mathrm{E}[\mathbf{N}(\sum_{i\neq j}\mathbf{s}_i\mathbf{s}_i^T)\mathbf{N}^H] = (K-1)P\mathbf{I}$, and $\mathrm{E}[\|\mathbf{s}_j\|^2] = P, \; j = 1, 2, \ldots, K$, thus yielding

$$\min_{\mathbf{w}_j} \mathrm{E}[\mathbf{e}_j^H \mathbf{e}_j] \approx \min_{\mathbf{w}_j}\{\sigma^2 c \mathbf{w}_j^H \mathbf{w}_j\}, \tag{2.40}$$

where $c = 2P + (K-3)(K-1)$.

Using the assumption (ii) and the approximate $\frac{\rho_{i,j}^s}{P} \approx 0,\ i \neq j$, the constraint of (2.20) can be approximately described as follows,

$$\mathrm{E}[|y_j|^2] \approx |h_j|^2 e_j^2 \mathbf{w}_j^H \mathbf{a}_j \mathbf{a}_j^H \mathbf{w}_j + \frac{\sigma^2}{P} \mathbf{w}_j^H \mathbf{w}_j = 1. \tag{2.41}$$

Using (2.39) and (2.41), the Lagrangian function is formulated as follows [49],

$$J(\mathbf{w}_j, \lambda) = \sigma^2 c \mathbf{w}_j^H \mathbf{w}_j + \mathbf{Re}\{\lambda^*(|h_j|^2 e_j^2 \mathbf{w}_j^H \mathbf{a}_j \mathbf{a}_j^H \mathbf{w}_j + \frac{\sigma^2}{P} \mathbf{w}_j^H \mathbf{w}_j - 1)\}. \tag{2.42}$$

The optimization problem (2.20) is equivalently equal to minimize the Lagrangian function (2.42). From (2.42), differentiating the Lagrangian function with respect to $\mathbf{w}_j^*$ and equate $\frac{\partial J(\mathbf{w}_j, \lambda)}{\partial \mathbf{w}_j^*}$ to zero, the Lagrange multiplier λ^* can be expressed as follows,

$$\lambda^* = \frac{-\sigma^2 c \mathbf{w}_j^H \mathbf{w}_j}{|h_j|^2 e_j^2 \mathbf{w}_j^H \mathbf{a}_j \mathbf{a}_j^H \mathbf{w}_j + \frac{\sigma^2}{P} \mathbf{w}_j^H \mathbf{w}_j}. \tag{2.43}$$

Substituting (2.43) into (2.42), the Lagrangian function can be expressed as a function of $\mathbf{w}_j$ as follows,

$$J(\mathbf{w}_j) = \frac{\sigma^2 c \|\mathbf{w}_j\|^2}{|h_j|^2 e_j^2 \|\mathbf{a}_j^H \mathbf{w}_j\|^2 + \frac{\sigma^2}{P} \|\mathbf{w}_j\|^2}. \tag{2.44}$$

Without loss of generality, let declare the weight vector $\mathbf{w}_j$ as a normalized complex-valued vector. Consequently, the minimization problem to (2.44) is equivalent to the maximization problem described as follows,

$$\max_{\mathbf{w}_j} \|\mathbf{a}_j^H \mathbf{w}_j\|^2. \tag{2.45}$$

The solution to (2.45) is readily obtained from the Cauchy-Schwarz inequality given by

$$(< \mathbf{a}_j, \mathbf{w}_j >)^2 \leq \|\mathbf{a}_j\|^2 \|\mathbf{w}_j\|^2 \tag{2.46}$$

with equality if and only if $\mathbf{w}_j$ is a multiple of $\mathbf{a}_j$. Therefore, the solution of (2.45) is given by

$$\mathbf{w}_j^{close} = \frac{\mathbf{a}_j}{\|\mathbf{a}_j\|}. \tag{2.47}$$

It is worth noticing that $\|\mathbf{a}_j^H \mathbf{w}_j\|^2$ is the radiation pattern of the half-wavelength M-element ULA [27] described as follows,

$$\|\mathbf{a}_j^H \mathbf{w}_j\|^2 = \frac{\sin^2(M\frac{\alpha}{2})}{M^2 \sin^2(\frac{\alpha}{2})}, \tag{2.48}$$

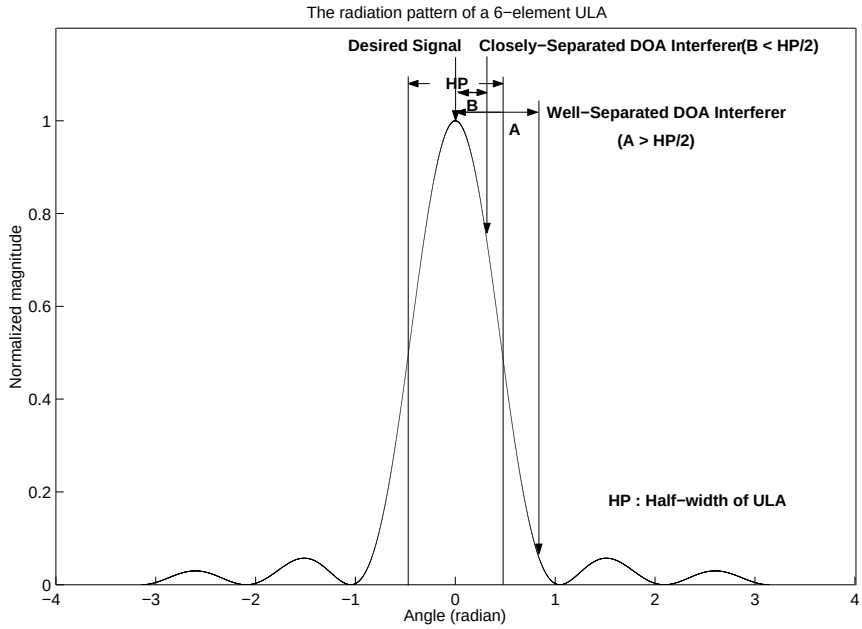

Figure 2.4: The illustration of the closely- and well-separated-DOA situations when two users' signals impinge on the 6-element ULA with two different DOAs.

in which the principle maximum occurs at $\alpha = 0$. Hence, (2.47) yields the maximum array response to the desired signal's DOA.

It is worth noticing that this solution is the same as the LCMV optimum solution in (2.33). In the case of the well-separated-DOA situation as illustrated in Fig.2.4, where the difference between the strongest interference signal's DOA and the desired signal's DOA is larger than a half of the half-width of the M-element ULA, it is worth to exploit the nulling capability of the array antenna to nullify this strongest interference signal. The benefit for exploiting the nulling capability is revealed from the improvement of the average BER of the IRBAP. Firstly, let consider the error signal of the IRBAP $\mathbf{e}_j^H$ when the interference rejection part is not employed, which directly results in subsuming the minimization method of the existing work [19]. This error signal can be approximately expressed as follows,

$$\mathbf{e}_j^H \approx \sum_{k=1,k\neq j}^{K} h_k e_k b_k \mathbf{w}_j^H \mathbf{a}_k \mathbf{s}_k^T + \frac{1}{P}\mathbf{w}_j^H \mathbf{N}(\mathbf{I} - \mathbf{s}_j \mathbf{s}_j^T). \tag{2.49}$$

By using the assumption (ii) and (iv), the optimization problem (2.20) can be reformulated as follows,

$$\min_{\mathbf{w}_j} \mathrm{E}[\mathbf{e}_j^H \mathbf{e}_j] \approx \min_{\mathbf{w}_j} \{P \sum_{k=1,k\neq j}^{K} |h_k|^2 e_k^2 \mathbf{w}_j^H \mathbf{a}_k \mathbf{a}_k^H \mathbf{w}_j + \sigma^2 (P-1)\mathbf{w}_j^H \mathbf{w}_j\}. \tag{2.50}$$

The constraint is similar to (2.41). Similarly, the Lagrangian function can be formulated by using (2.50) and (2.41) as follows,

$$J(\mathbf{w}_j, \lambda) = P \sum_{k=1, k\neq j}^{K} |h_k|^2 e_k^2 \mathbf{w}_j^H \mathbf{a}_k \mathbf{a}_k^H \mathbf{w}_j + \sigma^2 (P-1) \mathbf{w}_j^H \mathbf{w}_j$$
$$+ \mathbf{Re}\{\lambda^* (|h_j|^2 e_j^2 \mathbf{w}_j^H \mathbf{a}_j \mathbf{a}_j^H \mathbf{w}_j + \frac{\sigma^2}{P} \mathbf{w}_j^H \mathbf{w}_j - 1)\}. \tag{2.51}$$

In this situation, an assumption that there exists the strongest interference signal, let say the s^{th} signal, in the overall received signal $\mathbf{X}_{j-1}$ of the j^{th} stage is imposed; and this interference signal dominates the influence of all interference signals. The solution that minimizes the Lagrangian function (2.51) can be found as follows.

From (2.51), similarly, differentiating the Lagrangian function with respect to $\mathbf{w}_j^*$ and equate $\frac{\partial J(\mathbf{w}_j, \lambda)}{\partial \mathbf{w}_j^*}$ to zero, the Lagrange multiplier λ^* can be expressed as follows,

$$\lambda^* = \frac{-(P \sum_{k=1, k\neq j}^{K} |h_k|^2 e_k^2 \mathbf{w}_j^H \mathbf{a}_k \mathbf{a}_k^H \mathbf{w}_j + \sigma^2 (P-1) \mathbf{w}_j^H \mathbf{w}_j)}{|h_j|^2 e_j^2 \mathbf{w}_j^H \mathbf{a}_j \mathbf{a}_j^H \mathbf{w}_j + \frac{\sigma^2}{P} \mathbf{w}_j^H \mathbf{w}_j}. \tag{2.52}$$

Substituting (2.52) into (2.51), the Lagrangian function can be expressed as a function of $\mathbf{w}_j$ as follows,

$$J(\mathbf{w}_j) = \frac{P \sum_{k=1, k\neq j}^{K} |h_k|^2 e_k^2 \|\mathbf{a}_k^H \mathbf{w}_j\|^2 + \sigma^2 (P-1) \|\mathbf{w}_j\|^2}{|h_j|^2 e_j^2 \|\mathbf{a}_j^H \mathbf{w}_j\|^2 + \frac{\sigma^2}{P} \|\mathbf{w}_j\|^2}. \tag{2.53}$$

By the assumption that there exists the s^{th} strongest interference signal, (2.53) can be approximated as follows,

$$J(\mathbf{w}_j) \approx \frac{P |h_s|^2 e_s^2 \|\mathbf{a}_s^H \mathbf{w}_j\|^2 + \sigma^2 (P-1) \|\mathbf{w}_j\|^2}{|h_j|^2 e_j^2 \|\mathbf{a}_j^H \mathbf{w}_j\|^2 + \frac{\sigma^2}{P} \|\mathbf{w}_j\|^2}. \tag{2.54}$$

Similarly, let declare the weight vector $\mathbf{w}_j$ in a similar form as (2.47). It is obvious that $\|\mathbf{a}_s^H \mathbf{w}_j\|^2$ and $\|\mathbf{a}_j^H \mathbf{w}_j\|^2$ are the radiation patterns; as a result, the solution of (2.54) is related to the principle maximum and nulls of the array antenna. Intuitively, the solution of (2.54) is to direct the nearest null toward the strongest interference signal's DOA, i.e. minimize $\|\mathbf{a}_s^H \mathbf{w}_j\|^2$ with respect to $\mathbf{w}_j$, meanwhile maintaining the desired signal's DOA close to the principle maximum, i.e. maximize $\|\mathbf{a}_j^H \mathbf{w}_j\|^2$ with respect to $\mathbf{w}_j$, as much as possible.

The solution of (2.54) is the phase-shifted version of (2.47) by the amount of phase shift described as follows [27],

$$\Delta\phi_{st}^j = \min_n \{-(\phi_j - \arcsin(\sin \phi_s^j \pm \frac{2n\pi}{M}))\}, \; n = 1, 2, \ldots, M-1, \tag{2.55}$$

where ϕ_j denotes the desired signal's DOA and ϕ_s^j denotes the strongest interference signal's DOA at the j^{th} stage. In the in-beam interference situation, where the desired signal's DOA and the strongest interference signal's DOA are within the main beam of the M-element ULA, the phase shift in (2.55) is given by

$$\Delta\phi_{st}^j = -(\phi_j - \arcsin(\sin\phi_s^j \pm \frac{2\pi}{M})), \tag{2.56}$$

where the first null is exploited. Accordingly, by using (2.56), the solution of (2.54) can be described as follows,

$$\mathbf{w}_j^{well} \;=\; [1 \; e^{-j\theta_j} \; e^{-2j\theta_j} \; \ldots \; e^{-(M-1)j\theta_j}]^T/\sqrt{M}, \tag{2.57}$$

where $\theta_j = \omega\sin(\phi_j + \Delta\phi_{st}^j) = \omega(\sin(\phi_s^j) \pm \frac{2\pi}{M})$.

It is worth mentioning that this solution does not provide the benefit to the IRBAP in the case of the closely-separated-DOA situation as illustrated in Fig.2.4, where the difference between the desired signal's and the strongest interference signal's DOAs is smaller than a half of the half-width of the M-element ULA. The reason is that the IRBAP places the first null toward the strongest interference signal's DOA which is closely located near the desired signal's DOA; as a result, the desired signal is also affected by this null leading to the significant decrease in SINR, and hence, the average BER significantly increases. At this point, the real-valued parameter C corresponding to each particular situation can be determined as follows,

$$C = \begin{cases} \infty, \; |\phi_j - \phi_s^j| > \frac{HP}{2} & \text{(for the well-separated-DOA situation)} \\ P, \; \text{Otherwise} & \text{(for the closely-separated-DOA situation)} \end{cases} \tag{2.58}$$

It is worth mentioning that the operation modes of IRBAP can be categorized based on three different situations as follows. Firstly, in the closely-separated-DOA situation (see also Fig.2.4) where the differences between the signal's DOA of all users are smaller than $\frac{\text{HP}}{2}$, the interference rejection part is employed, i.e. $C = P$; as a result, the asymptotic solution of the weight vector of the blind array processing $\mathbf{w}_j^{close}$ is the LCMV beamforming's optimum weight vector in (2.33). Secondly, in the well-separated-DOA situation (see also Fig.2.4) where the differences between the signal's DOA of all users are larger than $\frac{\text{HP}}{2}$, the interference rejection part is not employed , i.e. $C = \infty$; as a result, the asymptotic solution of the weight vector of the blind array processing $\mathbf{w}_j^{well}$ is the same as the the solution of the minimization method in [19], in which the nulling capability of the ULA is exploited.

Finally, in the mixed-separated-DOA situation where some of the signal's DOAs are closely separated and the others are well separated, the IRBAP employs the interference rejection operation, by using the signature sequences of the interfering users as the key parameters for constructing the interference rejection part, for a group of signals which are closely distributed relatively to the desired signal's DOA, meanwhile, for those signals which their DOAs are well distributed relatively to the desired signal's DOA, the interference rejection operation is not employed. Hence, the IRBAP is able to exploit the nulling capability for nulling the well-separated-DOA interference signals while maintaining its main beam direct toward the desired signal's DOA without being annoyed by the closely-separated-DOA interference signals; as a result, the IRBAP is more robust to the in-beam interference signals than the existing approaches in [19]. Furthermore, the average BER is significantly improved, especially in the nonordering-user-power arrangement, as will be shown in Section 2.6.

2.5.3 Bit Error Rate Analysis

In this section, the BER of the IRBAP is analyzed for using as a benchmark in the simulation section (Section 2.6). First, the SINR of the decision variable of the j^{th} stage z_j is explored, and then the Gaussian approximation is used to evaluate the BER of the IRBAP by assuming the channel gain is fixed for a certain period of time. In addition, $\phi_j,\ j = 1, 2, \ldots, K$ are assumed perfectly known for the sake of exposition.

From a relationship that (2.57) is a generalized form of (2.47) with a phase shift, a generalized form of the weight vector of the signal canceller $\mathbf{u}_j$ can also be determined by substituting (2.57) into (2.30), and thus, the minimization problem in (2.34) can be reformulated as follows,

$$\min_{\mathbf{u}_j} \mathrm{E}\left[\|Y_j\|^2\right] = \min_{\mathbf{u}_j} \mathrm{E}\left[\|(\mathbf{a}_j - \mathbf{u}_j \mathbf{w}_j^{H_{well}} \mathbf{a}_j) h_j e_j b_j \mathbf{s}_j^T\|^2\right]. \tag{2.59}$$

It is straightforward that the optimum solution for (2.59) that yields (2.59) to achieve its minimum value, which is zero, is given as

$$\mathbf{u}_j^{well} = \frac{\mathbf{a}_j}{\mathbf{w}_j^{H_{well}} \mathbf{a}_j}, \tag{2.60}$$

where $\mathbf{w}_j^{H_{well}} \mathbf{a}_j = g(\phi_j, \phi_s^j) e^{-j\frac{\omega}{2}(\sin\phi_j - \sin\phi_s^j \mp \frac{2\pi}{M})}$ and $g(\phi_j, \phi_s^j) = \frac{\sin(\frac{\omega M}{2}(\sin\phi_j - \sin\phi_s^j \mp \frac{2\pi}{M}))}{\sqrt{M}\sin(\frac{\omega}{2}(\sin\phi_j - \sin\phi_s^j \mp \frac{2\pi}{M}))}$.

Substituting the generalized weight vectors $\mathbf{w}_j^{well}$ and $\mathbf{u}_j^{well}$ in (2.57) and (2.60), respectively, into (2.28), the decision variable of the j^{th} stage can be expressed as follows,

$$\begin{aligned} z_j &= \frac{y_j}{h_j} \\ &= g(\phi_j, \phi_s^j) e_j b_j e^{-j\frac{\omega}{2}(\sin\phi_j - \sin\phi_s^j \mp \frac{2\pi}{M})} + i_j, \end{aligned} \tag{2.61}$$

where

$$\begin{aligned} i_j &= \frac{1}{P}\sum_{k=j+1}^{K}\{\frac{h_k}{h_j} e_k b_k \rho_{j,k}^s g(\phi_k, \phi_s^j) e^{j(\frac{\omega}{2}(\sin\phi_s^j - \sin\phi_k \pm \frac{2\pi}{M}))}\} + \frac{n_j^{'}}{Ph_j} \\ &\quad - \frac{1}{Ph_j}\sum_{i=1}^{j-1}\{\frac{i_i \rho_{j,i}^s g(\phi_i, \phi_s^j)}{g(\phi_i, \phi_s^i)} e^{j(\frac{\omega}{2}(\sin\phi_s^j - \sin\phi_s^i)}\}. \end{aligned} \tag{2.62}$$

Firstly, the signal power from the first term on the right hand side of (2.61) by given e_j is computed as follows,

$$\begin{aligned} \text{Signal power} &= \mathrm{E}[\|g(\phi_j, \phi_s^j) e_j b_j e^{-j\frac{\omega}{2}(\sin\phi_j - \sin\phi_s^j \mp \frac{2\pi}{M})}\|^2] \\ &= g^2(\phi_j, \phi_s^j) e_j^2. \end{aligned} \tag{2.63}$$

Secondly, the interference and noise power ς_j from the second term on the right hand side of (2.61) are computed by given $\{e_j\},\ j = 1, 2, \ldots, K$ as follows,

$$\begin{aligned} \varsigma_j &= \frac{1}{P^2}\sum_{k=j+1}^{K}\left|\frac{h_k}{h_j}\right|^2 e_k^2 g^2(\phi_k, \phi_s^j)\mathbf{Var}[\rho_{j,k}^s] + \frac{1}{P^2|h_j|^2}\sum_{i=1}^{j-1}\frac{\varsigma_i g^2(\phi_i, \phi_s^j)}{g^2(\phi_i, \phi_s^i)}\mathbf{Var}[\rho_{j,i}^s] \\ &\quad + \frac{1}{P^2|h_j|^2}\mathrm{E}[\|\mathbf{w}_j^H \mathbf{N}\mathbf{s}_j\|^2]. \end{aligned} \tag{2.64}$$

If the spreading factor $P >> 1$, then the signature cross-correlation $\rho_{j,k}^s$ has a zero mean and variance $\frac{1}{P}$ [32]. In addition, $\frac{1}{P^2}\mathrm{E}[\|\mathbf{w}_j^H \mathbf{N}\mathbf{s}_j\|^2] = \sigma^2$. Hence, the closed form expression for (2.64) can be expressed as follows:

$$\varsigma_j = \frac{1}{P^3}\sum_{k=j+1}^{K}\left|\frac{h_k}{h_j}\right|^2 e_k^2 g^2(\phi_k, \phi_s^j) + \frac{1}{P^3|h_j|^2}\sum_{i=1}^{j-1}\frac{\varsigma_i g^2(\phi_i, \phi_s^j)}{g^2(\phi_i, \phi_s^i)} + \frac{\sigma^2}{|h_j|^2}. \tag{2.65}$$

Using (2.63) and (2.65), the SINR of the decision variable z_j is given by

$$\text{SINR} = \frac{g^2(\phi_j, \phi_s^j) e_j^2}{\varsigma_j} \tag{2.66}$$

The hard-limited detector is employed as a detector described as follows,

$$\widehat{b}_j = \text{sign}(\text{Re}\{z_j\}), \tag{2.67}$$

where sign$(\cdot)$ stands for the sign operator, and Re$\{\cdot\}$ stands for the real operator.

In the AWGN channel, the probability of error of the matched filter output can be computed by using the Gaussian approximation as follows [50],

$$P_e^j = Q(\sqrt{\frac{g^2(\phi_j, \phi_s^j)e_j^2}{\varsigma_j}}), \tag{2.68}$$

where $Q(\cdot)$ is the Q-function defined as $Q(z) = \int_z^\infty \frac{1}{\sqrt{2\pi}} e^{\frac{-y^2}{2}} dy$.

Note that $(\sin\phi_j - \sin\phi_s^j),\ j = 1, 2, \ldots, K$ in $g^2(\phi_j, \phi_s^j)$ plays a major role in the probability of error of the IRBAP. The probability of error expression for the weight vector in (2.47) is obtained when $(\sin\phi_j - \sin\phi_s^j) = \pm\frac{2\pi}{M},\ j = 1, 2, \ldots, K$, corresponding to the closely-separated-DOA situation.

2.5.4 Complexity Comparison and Suboptimum Approach

It is worth noticing that the IRBAP imposes more complexity in term of a hardware requirement, which is linear with the number of users in the system, than the original adaptive blind array processing [19]. The extra hardware requirement depends on the signal's DOA situations described as follows. In the closely-separated-DOA situation, at the first stage as shown in Fig.2.3 at the $(K-1)$-block interference rejection part, the IRBAP requires $(K-1)$ more blocks of the matched filter and the re-spreading block than the original one. Similarly, at the second stage, the IRBAP only requires the $(K-2)$ extra blocks of the matched filter and the re-spreading block since the first signal is captured can cancelled from the overall received signal at the first stage, and hence, the third stage only requires the $(K-3)$ extra blocks of the matched filter and the re-spreading block and so on. At the final stage, the IRBAP does not use the interference rejection part anymore. Consequently, in the K-user DS-CDMA system, the IRBAP has $\frac{K}{2}(K+1)$ more blocks of the matched filter and the re-spreading block than the original one. This increasing complexity results in the significant improvement in the probability of error especially for the closely-separated-DOA situation.

However, in the well-separated-DOA situation, the IRBAP can be reduced to the original scheme because the $(K-1)$-block interference rejection part is not needed in this situation by setting $C = \infty$. In the mixed-separated-DOA situation, the IRBAP only requires the extra matched filter and the re-spreading blocks for constructing the interference rejection part

correspondingly equal to a number of users whose DOAs are closely distributed relatively to the desired signal's DOA. Hence, in this situation, the extra hardware requirement for IRBAP is always less than $\frac{K}{2}(K+1)$ blocks. In terms of the convergence rate of the adaptive algorithm (see (2.23)), the IRBAP yields a faster convergence rate than the original scheme in the nonordering-user-power closely-separated-DOA situation because it operates adaptively without the influence of the MAI. By observing from the simulation results, in average, the IRBAP needs about 100 iterations at SNR = 3 dB to converge in both nonordering-user-power well-separated-DOA and nonordering-user-power closely-separated-DOA situations in the AWGN channel. In comparison with the original scheme, the original scheme needs about 100 iterations to converge in the nonordering-user-power well-separated-DOA situation; however, in the nonordering-user-power closely-separated-DOA situation, it cannot form the main beam toward the desired signal's DOA resulting in failing to capture the desired signal. As a result, the convergence rate of the original scheme cannot be determined in the nonordering-user-power closely-separated-DOA situation. Obviously, the IRBAP provides the added benefits in terms of convergence rate and stability to the wireless communication system although these benefits come at the price of the linearly increasing complexity. Furthermore, the IRBAP provides robustness to the fading channel environment and the Near-Far effect scenario because of the user-power-arrangement independent property as shown in the simulation results (in section 2.6).

The suboptimum approach that can reduce the extra hardware requirement for the IRBAP can be described as follows. If the instantaneous power of all users' signal is assumed known and the j^{th} signal at the j^{th} stage is being captured, the signature sequences of the interfering users whose DOAs are closely distributed relatively to the j^{th} signal's DOA and their signal strength are stronger than the j^{th} signal can only be used to construct the interference rejection part. According to this suboptimum approach, the extra hardware requirement for the IRBAP is always less than or equal to $\frac{K}{2}(K+1)$ blocks of the matched filter and the re-spreading block in all DOA situations.

2.6 Simulation Results

In this section, the BER performance of IRBAP in DS-CDMA systems is studied. In the simulations, the number of users in the system is $K = 5$ users, the spreading code is

the Gold Code with length $N = 31$, the $M = 6$ element ULA with inter-element spacing $d = \frac{\lambda}{2}$ is employed, and the signal powers are not equal in order to realize the Near-Far effect scenario. From [27] and the aforementioned parameters, it can be shown that the nulls occur at $\alpha = n60^{\circ},\ n = 1, 2, \ldots, 5$ and the half-width is equal to $HP \approx 19^{\circ}$.

The channel models are the AWGN channel and the slow-varying Rayleigh fading channel, and the synchronous CDMA system is employed. The modulation scheme is BPSK with a carrier frequency $f_c = 900MHz$, and the step size of the blind array processing and the signal canceller are 0.03 and 0.08, respectively. In the slow-varying Rayleigh fading channel, Jakes' model [51] with Doppler's shift 20 Hz is employed, and each user undergoes the spatially independent fading channel with unit variance. In addition, the user data are generated randomly with equi-probability $b_{k,i} \in \{-1, +1\}$. The performance of the proposed scheme is compared with the minimization and maximization methods in [19], and the blind RLS based space-time adaptive 2-D RAKE receivers in [37]. For fair comparison, the received signals are sampled at the chip rate for all schemes. In addition, the number of non-overlapped sliding windows is set to be 31 per bit, and the forgetting factors to be 1 for the scheme as in [37].

For the sake of convenience, let declare the notations used in the simulation results as follows:

- No BF Gaussian is the single-element conventional receiver case in the AWGN channel;
- No BF Gaussian+Rayleigh is the single-element conventional receiver case in the AWGN and slow-varying Rayleigh fading channels;
- Theoretical Gaussian is the theoretical bit error probability of the IRBAP in (2.68) in the AWGN channel;
- Min. Gaussian is the minimization algorithm [19] in the AWGN channel;
- Min. Gaussian+Rayleigh is the minimization algorithm [19] in the AWGN and slow-varying Rayleigh fading channels;
- Max. Gaussian is the maximization algorithm [19] in the AWGN channel;
- Max. Gaussian+Rayleigh is the maximization algorithm [19] in the AWGN and slow-varying Rayleigh fading channels;

- Blind RLS Gaussian is the blind RLS based space-time adaptive 2-D RAKE receivers [37] in the AWGN channel;
- Blind RLS Gaussian+Rayleigh is the blind RLS based space-time adaptive 2-D RAKE receivers [37] in the AWGN and slow-varying Rayleigh fading channels;
- Proposed Gaussian is the IRBAP with zero-weight initialization in the AWGN channel;
- Proposed Gaussian+Rayleigh is the IRBAP with zero-weight initialization in the AWGN and slow-varying Rayleigh fading channels;

Two cases are examined, where each of which has three different DOA situations. In the first case, the receiver stages are arranged from capturing the strongest user down to the weakest user, and in the second case, they are not. Three different DOA situations including the closely-separated-DOA situation, the well-separated-DOA situation, and the mixed-separated-DOA situation are studied. The performance measures used in the experiments are the average BER of all users versus the Signal-to-Noise ratio (SNR), and the beam pattern of the 6-element ULA.

2.6.1 The Ordering User-Power Arrangement

Table 2.1: Directions of arrival and amplitudes of all users for ordering user-power arrangement in the closely- and well-separated-DOA situations.

User	1	2	3	4	5
Directions of Arrival	ϕ_1	$\phi_1 + \triangle\phi$	$\phi_1 + 2\triangle\phi$	$\phi_1 + 3\triangle\phi$	$\phi_1 + 4\triangle\phi$
Amplitude	10	5	1.5	1	1

The initial parameters of the first experiment are shown in table 2.1, where ϕ_1 is the uniformly distributed random variable within the interval $0 \leq \phi_1 + k\triangle\phi \leq \pi,\ k = 1, 2, \ldots, 4$, where $|\phi_j - \phi_i| < 9.5^\circ,\ i, j \in \{1, 2, \ldots, 5\}$. First, the closely-separated DOA scenario is studied, where $\triangle\phi = 2^\circ,\ C = P$, and the phase shifts for calculating the theoretical average BER are equal to zero for all stages. The graph of average BER versus SNRs averaging over 100 independent runs, 10000 iterations, and $K = 5$ users is shown in Fig.2.5. It is clear that the proposed IRBAP yields a better performance than the existing work in [19] and [37]. For instance, in the AWGN channel, compared with the IRBAP, the minimization method of the existing work needs about 1 dB more SNR for a 10^{-3} BER, whereas the maximization

method of the existing work needs about 7 dB more SNR. Furthermore, the IRBAP yields BER close to that of the theoretical BER. In the AWGN and slow-varying Rayleigh fading channels, at BER=10^{-3}, the minimization and maximization methods of the existing work need about 0.8 dB and 4 dB, respectively, more SNR than the IRBAP. In addition, the blind RLS based approach performs poorly because it does not employ any interference cancellation, and it does not have enough degree of freedom to cancel the severe in-beam interference signals.

Secondly, the situation that all users' DOAs are well separated is studied. The initial parameters are the same as shown in table 2.1 except that $\triangle\phi = 30^\circ,\ C = \infty$, and the phase shifts for calculating the theoretical average BER are calculated according to (2.57). The graph of average BER versus SNRs averaging over 100 independent runs, 10000 iterations, and $K = 5$ users is shown in Fig.2.6. Notice that the IRBAP and the minimization method of the existing work provide the same BER performance, which is close to that of the theoretical BER in the AWGN channel. The maximization method of the existing work needs about 6 dB, in the AWGN channel, and 2 dB, in the AWGN and slow-varying Rayleigh fading channels, respectively, more SNR than the IRBAP at BER=10^{-3}. It is worth noticing that the blind RLS based approach performs the best where its BER coincides with the theoretical bound in the AWGN channel; meanwhile, in the AWGN and slow-varying Rayleigh fading channels, it performs worse than the IRBAP in low SNR regimes but comparable to the IRBAP in high SNR regimes.

Finally, the situation that the first three users' DOAs are closely separated and the two remaining users' DOAs are well separated is studied. The initial parameters are shown in table 2.2.

Table 2.2: Directions of arrival and amplitudes of all users for ordering user-power arrangement in the mixed-separated-DOA situation.

User	1	2	3	4	5
Directions of Arrival	ϕ_1	$\phi_1 + \triangle_1\phi$	$\phi_1 + 2\triangle_1\phi$	$\phi_1 + 3\triangle_2\phi$	$\phi_1 + 4\triangle_2\phi$
Amplitude	10	5	1.5	1	1

In this experiment, $\triangle_1\phi = 2^\circ$, where $|\phi_j - \phi_i| < 9.5^\circ,\ i, j \in \{1, 2, 3\}$ and $\triangle_2\phi = 60^\circ$, where $|\phi_j - \phi_i| > 9.5^\circ,\ i, j \in \{4, 5\}$. In addition, the value of C's for the first three stages

are set to be equal to P and the phase shifts are equal to zeros; meanwhile, the value of C's for the remaining two stages are set to be equal to infinity and the phase shifts are calculated according to (2.57). The graph of average BER versus SNRs averaging over 100 independent runs, 10000 iterations, and $K = 5$ users is shown in Fig.2.7. Notice that, in the AWGN channel at BER = 10^{-3}, the minimization method of the existing work needs to use the SNR more than the IRBAP about 0.6 dB, whereas the maximization method of the existing work needs 6 dB more SNR than IRBAP. Furthermore, the IRBAP provides the BER closely to that of the theoretical BER. In the AWGN and slow-varying Rayleigh fading channels, at BER=10^{-3}, the minimization and maximization methods of the existing work need about 2 dB and 4 dB, respectively, more SNR than the IRBAP. In addition, the blind RLS based approach still suffers from the severe in-beam interference signals resulting in a poor BER.

From the above experimental results, it is worth noticing that the probability of error of the proposed scheme is close to that of the theoretical probability of error. On the other hand, the maximization method in the existing work [19] has a poor probability of error performance in all situations whereas the minimization method has the best result in the well-separated-DOA situation. These phenomena also support the derivations in section 2.5.2.

2.6.2 The Non-ordering User-Power Arrangement

In these experiments, the situation that the strongest user is not located at the first stage is investigated, which results in the severe condition where the average BER will increase inevitably.

Table 2.3: Directions of arrival and amplitudes of all users for non-ordering user-power arrangement in the closely- and well-separated-DOA situations.

User	1	2	3	4	5
Directions of Arrival	ϕ_1	$\phi_1 + \triangle_1\phi$	$\phi_1 + 2\triangle_1\phi$	$\phi_1 + 3\triangle_2\phi$	$\phi_1 + 4\triangle_2\phi$
Amplitude	1	10	1.5	1	5

The initial parameters of the first experiment are shown in table 2.3, where ϕ_1 is the uniformly distributed random variable within the interval $0 \leq \phi_1 + k\triangle\phi \leq \pi,\ k = 1, 2, \ldots, 4$, where $|\phi_j - \phi_i| < 9.5^\circ,\ i, j \in \{1, 2, \ldots, 5\}$. First the closely-separated DOA scenario is studied,

where $\triangle\phi = 2°,\ C = P$, and the phase shifts for calculating the theoretical average BER are equal to zero for all stages. The graph of average BER versus SNRs averaging over 100 independent runs, 10000 iterations, and $K = 5$ users is shown in Fig.2.8. It is clear that the proposed IRBAP yields a much better performance than the existing work in [19] and [37]. For instance, in the AWGN channel, compared with the IRBAP, the minimization method of the existing work needs about 11 dB more SNR for a 10^{-3} BER, whereas the maximization method of the existing work needs about 7 dB more SNR than IRBAP. Furthermore, the IRBAP yields BER close to that of the theoretical BER. In the AWGN and slow-varying Rayleigh fading channels, at BER=10^{-3}, the maximization method of the existing work needs about 3 dB more SNR than the IRBAP, whereas the minimization method of the existing work diverges at BER=10^{-2}.

Secondly, the situation that all users' DOAs are well separated is studied. The initial parameters are the same as shown in table 2.1 except that $\triangle\phi = 30°,\ C = \infty$, and the phase shifts for calculating the theoretical average BER are calculated according to (2.57). The graph of average BER versus SNRs averaging over 100 independent runs, 10000 iterations, and $K = 5$ users is shown in Fig.2.9. Notice that the IRBAP and the minimization method of the existing work provide the same BER performance, which is close to that of the theoretical BER. The maximization method of the existing work needs about 6 dB more SNR than the IRBAP, at BER=10^{-3}, in the AWGN channel; meanwhile, in the AWGN and slow-varying Rayleigh fading channels, it has a poor BER, e.g. BER=4×10^{-2} at SNR = 20, resulting from the fact that this method is not capable of nulling the interference signals [19].

Finally, the situation that the first three users' DOAs are closely separated and the two remaining users' DOAs are well separated is studied. The initial parameters are shown in table 2.4.

Table 2.4: Directions of arrival and amplitudes of all users for non-ordering user-power arrangement in the mixed-separated-DOA situation.

User	1	2	3	4	5
Directions of Arrival	ϕ_1	$\phi_1 + \triangle_1\phi$	$\phi_1 + 2\triangle_1\phi$	$\phi_1 + 3\triangle_2\phi$	$\phi_1 + 4\triangle_2\phi$
Amplitude	1	10	1.5	1	5

In this experiment, $\triangle_1\phi = 2°$, where $|\phi_j - \phi_i| < 9.5°,\ i, j \in \{1, 2, 3\}$ and $\triangle_2\phi = 60°$, where $|\phi_j - \phi_i| > 9.5°,\ i, j \in \{4, 5\}$, is set. In addition, the value of C's for the first three

stages are set to be equal to P and the phase shifts are equal to zeros; meanwhile, the value of C's for the remaining two stages are set to be equal to infinity and the phase shifts are calculated according to (2.57). The graph of average BER versus SNRs averaging over 100 independent runs, 10000 iterations, and $K = 5$ users is shown in Fig.2.10. Notice that, in the AWGN channel at BER = 10^{-3}, the minimization method of the existing work needs to use the SNR more than the IRBAP about 10 dB, whereas the maximization method of the existing work needs about 6 dB more SNR than IRBAP. Furthermore, the IRBAP provides the BER closely to that of the theoretical BER. In the AWGN and slow-varying Rayleigh fading channels, at BER=10^{-3}, the maximization method of the existing work needs about 3 dB more SNR than the IRBAP, whereas the minimization method of the existing work diverges at BER=10^{-2}.

Likewise, the blind RLS based approach performs the best in the well-separated-DOAs situation; however, it suffers from the severe in-beam interference signals in the closely- and mixed-separated-DOAs situations.

In the above results, it is worth noticing that the average probabilities of error of all users are greater than the results in the ordering user-power situation, especially in the AWGN and slow-varying Rayleigh fading channels. However, the proposed scheme still has lower average probabilities of error in both the AWGN channel and the AWGN and slow-varying Rayleigh fading channels. It is also worth noticing that, in high SNR regions, the theoretical BER and the BER of the IRBAP are more different than low SNR regions because the Gaussian approximation does well in the low SNR regions whereas it yields a poor approximation in the high SNR regions; and since the adaptive algorithms for adjusting weight vectors of the blind array processing and the signal canceller are employed, the detection and signal cancellation errors are inevitably occurred, especially in the transient state of the adaptation processes, resulting in higher probability of error than the theoretical result.

In Fig.2.11, the average BER versus the number of users in the nonordering-user-power mixed-separated-DOA situation, in the AWGN and slow-varying Rayleigh fading channels, at SNR = 8 dB is plotted. In addition, the number of users in the system are varying from 4 to 20 users; all users' DOA are uniformly distributed around the 6-element ULA within $[0, \pi]$; and the user's signal amplitude is randomly assigned in the range of [1,10]. At

BER=2.2×10^{-3}, it is worth noticing that the IRBAP can accommodate about 3 and 5 more users than the minimization method of the existing work and the single-element conventional receiver, respectively. Furthermore, when the number of users increases, the average BER of the IRBAP and the minimization method of the existing work gradually increase, whereas the average BER of the single-element conventional receiver rapidly increases. Obviously, the IRBAP always yields a better performance than the minimization method of the existing work and the single-element conventional receiver.

In Fig.2.12, the beam patterns of the first stage in the ordering-user-power closely-separated-DOA situation at SNR = 8 dB and the DOAs of 5 users are $30°$, $32°$, $34°$, $36°$, and $38°$, respectively, in the AWGN and slow-varying Rayleigh fading channels are shown. The signal amplitude of 5 users are shown in table 2.1. Notice that the IRBAP and the blind RLS based approach always direct its main beam toward the first user's DOA, whereas the minimization method of the existing work places a null toward the other users' DOA while maintaining the main beam as close to the desired signal's DOA as possible. Since the user arrangement is in the descending order, the minimization of the existing work is still able to preserve most of the desired signal's strength by slightly placing the null closely to its desired signal's DOA resulting in a slightly decrease in SINR, and hence, a slightly increase in the average BER as shown in Fig.2.5.

In Fig.2.13, the beam patterns of the first stage in the nonordering-user-power closely-separated-DOA situation at SNR = 8 dB and the DOAs of 5 users are $30°$, $32°$, $34°$, $36°$, and $38°$, respectively, in the AWGN and slow-varying Rayleigh fading channels are shown. The signal amplitude of 5 users are shown in table 2.3. Notice that the IRBAP always directs its main beam toward the first user's DOA, whereas the minimization method of the existing work and the blind RLS based approach place a null toward the other users' DOA without maintaining the main beam as close to the desired signal's DOA as possible. This phenomenon is due to the nonordering-user-power arrangement resulting in a significant decrease in SINR, and hence, a significant increase in the average BER as shown in Fig.2.8.

It is worth noticing that the results in Fig.2.12 and Fig.2.13 strongly support the derivations in Section 2.5.2.

2.7 Concluding Remark

In this chapter, the IRBAP which improves the performances of the wireless communication system in terms of the probability of error and the stability was proposed. Although the IRBAP required more complexity, which is linear with the number of users in the system, than the original scheme, the IRBAP did provide significant benefits, especially in the closely-separated-DOA situation. From the simulation results, the SNR improvement of the IRBAP over the original scheme, e.g. the minimization method, was significant in both the nonordering-user-power closely-separated-DOA and the nonordering-user-power mixed-separated-DOA situations. For instance, in the AWGN channel, the SNR difference was about 0.6 dB in the ordering-user-power mixed-separated-DOA situation, and 10 dB in the nonordering-user-power mixed-separated-DOA situation, at BER=10^{-3}. Furthermore, the probability of error curves of the IRBAP were quit close to that of the theoretical BER. In the AWGN and slow-varying Rayleigh fading channels, the SNR difference was about 2 dB in the ordering-user-power mixed-separated-DOA situation, at BER=10^{-3}; however, in the nonordering-user-power mixed-separated-DOA situation, the minimization method of the existing work diverged at BER=10^{-2} whereas the IRBAP still yielded a good BER.

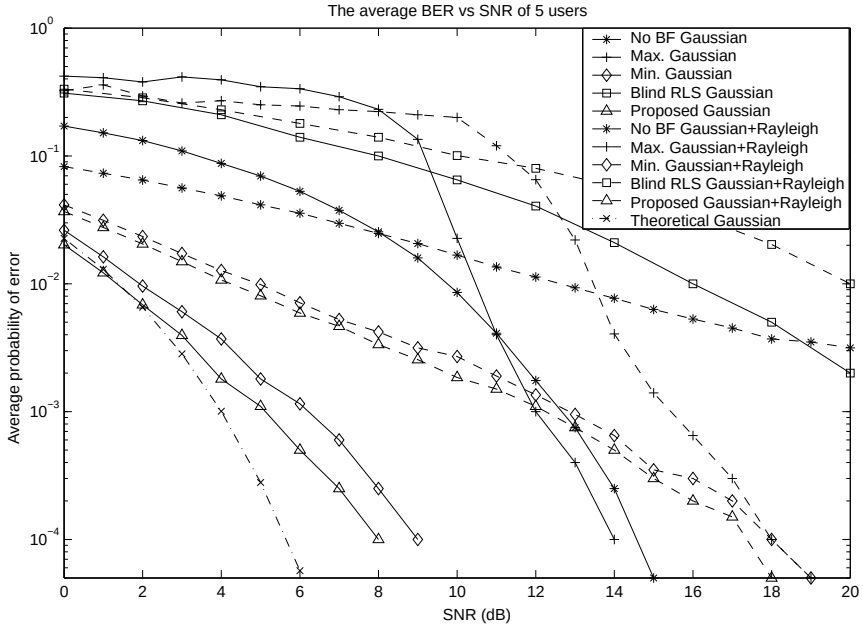

Figure 2.5: The graph of average BER versus SNRs averaging over 100 independent runs, 10000 iterations, and 5 users in the ordering-user-power closely-separated-DOA situation.

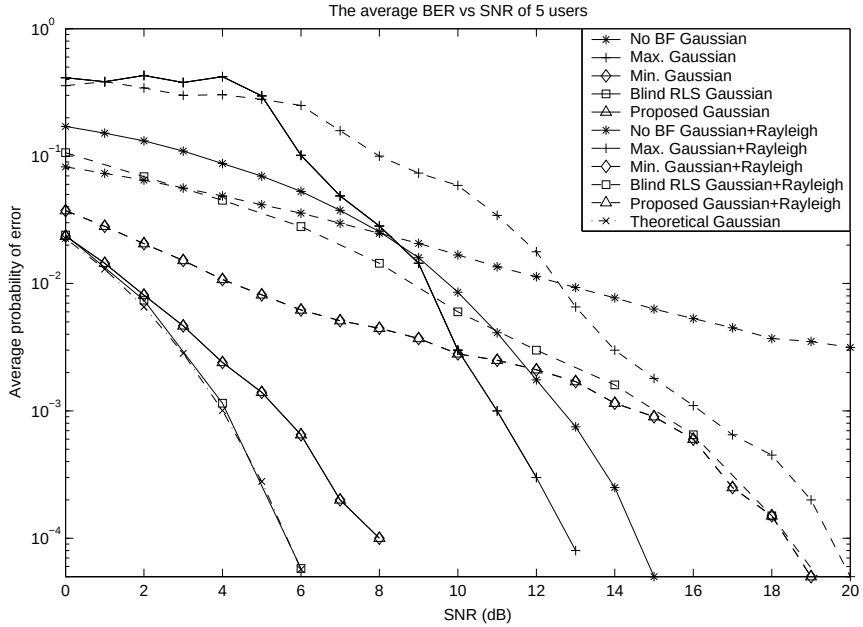

Figure 2.6: The graph of average BER versus SNRs averaging over 100 independent runs, 10000 iterations, and 5 users in the ordering-user-power well-separated-DOA situation.

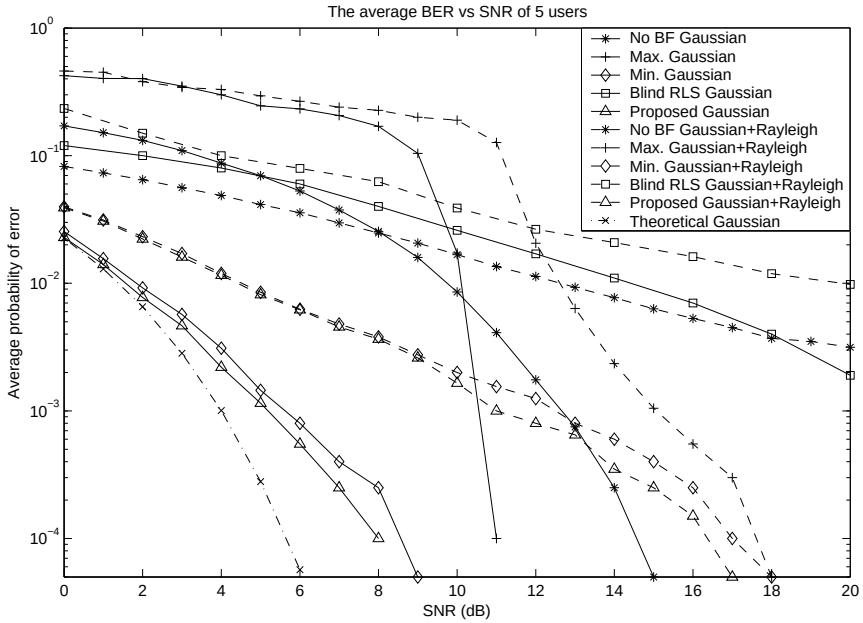

Figure 2.7: The graph of average BER versus SNRs averaging over 100 independent runs, 10000 iterations, and 5 users in the ordering-user-power mixed-separated-DOA situation.

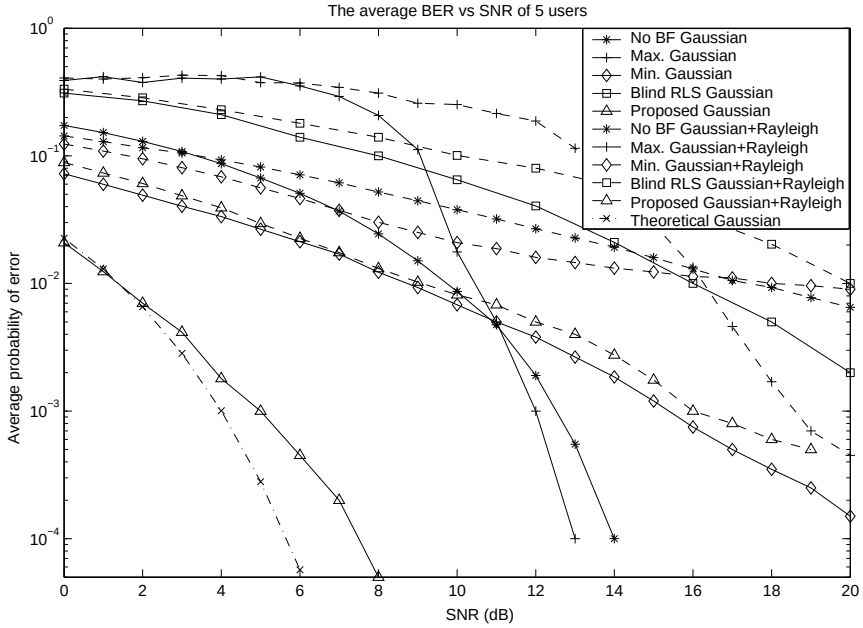

Figure 2.8: The graph of average BER versus SNRs averaging over 100 independent runs, 10000 iterations, and 5 users in the nonordering-user-power closely-separated-DOA situation.

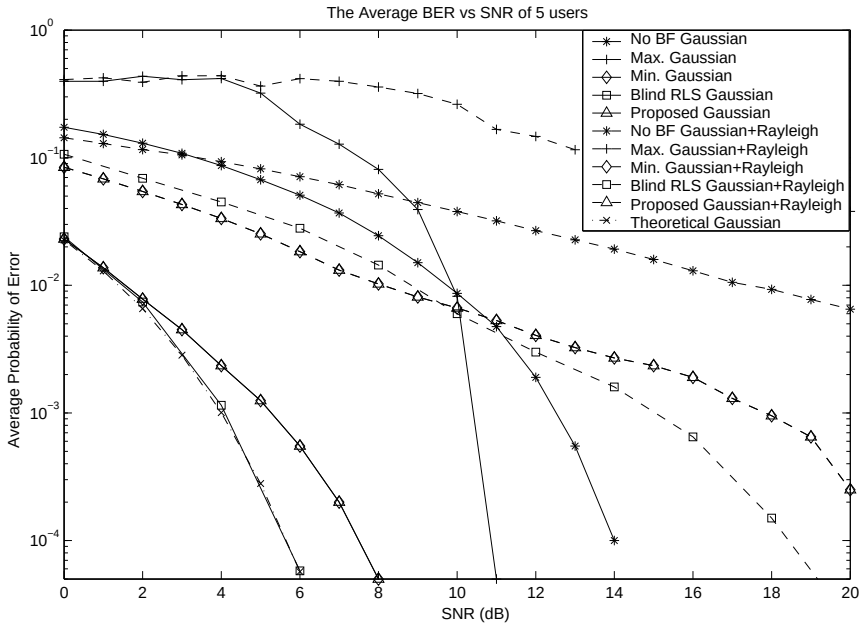

Figure 2.9: The graph of average BER versus SNRs averaging over 100 independent runs, 10000 iterations, and 5 users in the nonordering-user-power well-separated-DOA situation.

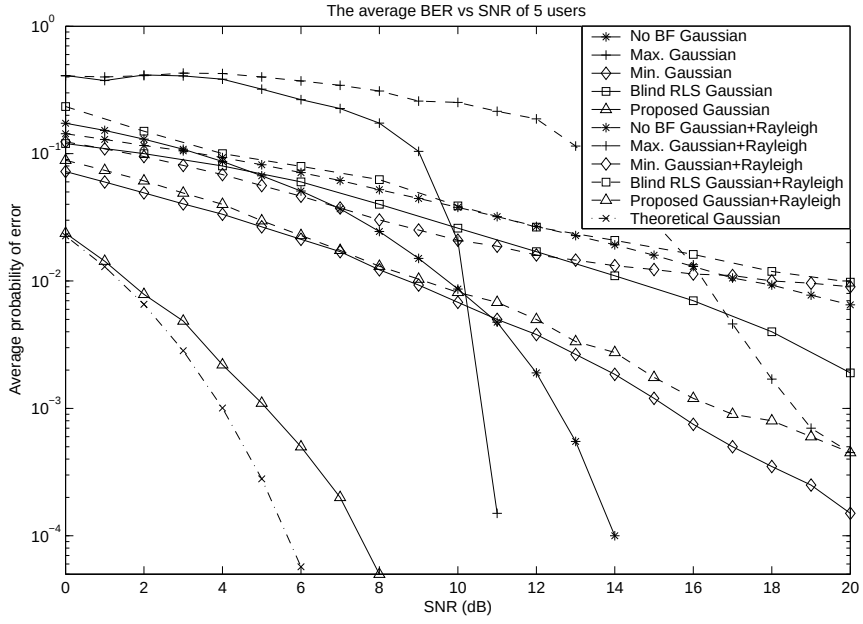

Figure 2.10: The graph of average BER versus SNRs averaging over 100 independent runs, 10000 iterations, and 5 users in the nonordering-user-power mixed-separated-DOA situation.

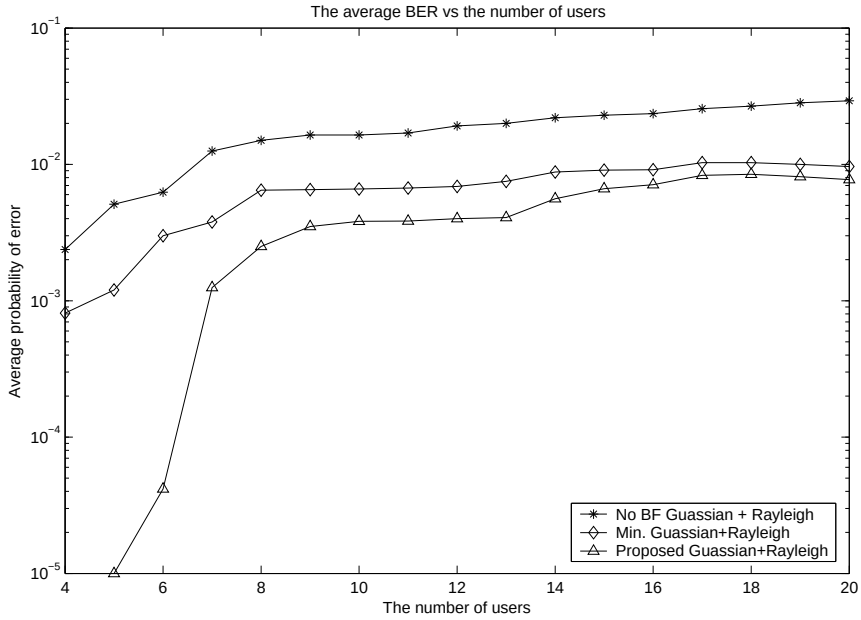

Figure 2.11: The graph of average BER versus the number of users at SNR = 8 dB averaging over 100 independent runs, 10000 iterations, in the nonordering-user-power mixed-separated-DOA situation.

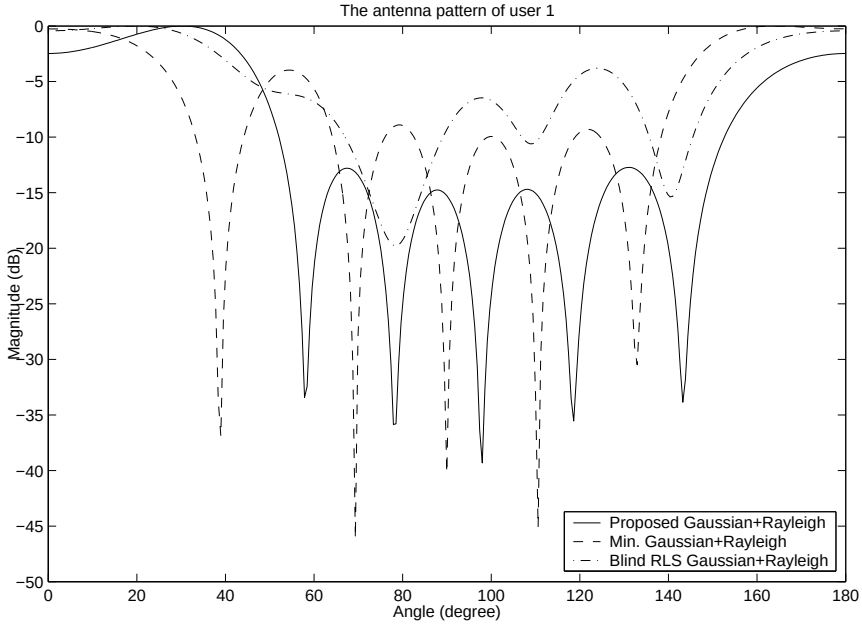

Figure 2.12: The graph of a beampattern of the first user at SNR = 8 dB and DOA = 30° in the ordering-user-power closely-separated-DOA situation.

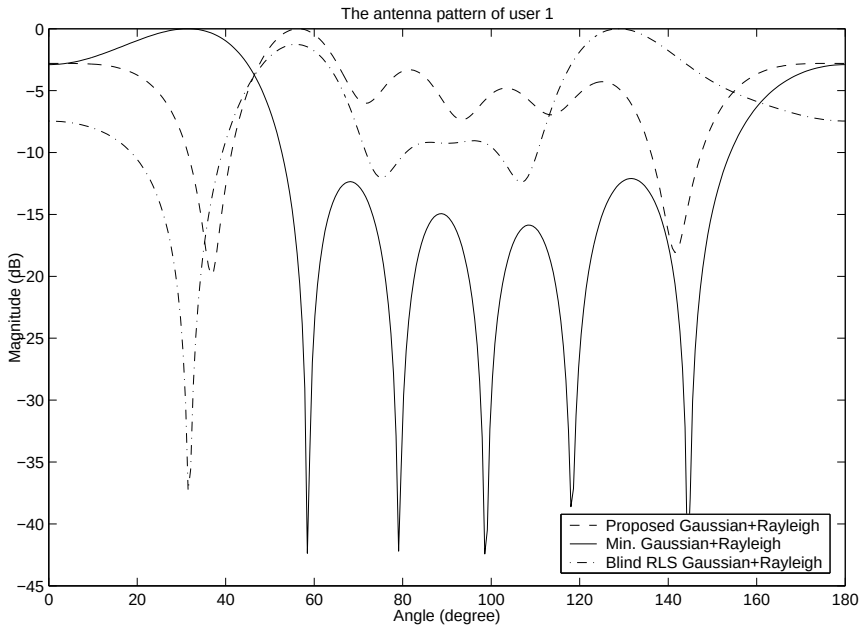

Figure 2.13: The graph of a beampattern of the first user at SNR = 8 dB and DOA = 30° in the nonordering-user-power closely-separated-DOA situation.

CHAPTER III

A DATA-BEARING APPROACH FOR PILOT-EMBEDDING FRAMEWORKS IN SPACE-TIME CODED MIMO SYSTEMS

In the previous chapter, the smart antenna system, i.e. IRBAP, for DS-CDMA systems has been presented. In this chapter, a channel estimation for space-time coded MIMO communications systems with flat fading channels is examined. The basic background concerning the state-of-the-art channel estimation techniques is reviewed. Then, channel and system models to be considered are presented. Further, a data-bearing approach for pilot-embedding frameworks, including required properties, channel estimation process, possible data bearer and pilot matrices, and data detection process, is proposed. Performance analysis as well as an optimum power allocation for the proposed scheme is also studied. Simulation results in comparison with analytical results, and concluding remark are given in the end of this chapter.

3.1 Introduction

MIMO communication systems provide prominent benefits to wireless communications due to the high capacity and reliability they can offer [2, 5]. Recently, the ST codes have been proposed in [13, 14, 52] for MIMO communications, in which the BER of the systems is significantly improved without increasing transmission power by exploiting transmit diversity [13].

A major challenge in wireless ST communications employing a coherent detector is the CSI acquisition [13, 14]. Typically, the CSI is acquired or estimated by using a pilot or training signal, a known signal transmitted from the transmitter to the receiver. This technique has been widely applied because of its feasibility for implementation with low computational complexity [16].

Two main pilot-aided channel estimation techniques have been proposed in both SISO and MIMO systems: the PSAM technique and the pilot-embedding technique. In the SISO

system, the PSAM technique has been intensively studied in [16] for frequency-nonselective fading channels, and was recently extended to MIMO systems [53--58]. In this technique, firstly, a pilot signal is time-multiplexed into a transmit data stream, and then, at the receiver side, this pilot signal is extracted from the received signal to acquire the channel state information. Furthermore, an interpolation technique by averaging channel estimates over a certain time period is employed in order to improve the accuracy of the channel estimates. The disadvantage of this technique is the sparse pilot arrangement that results in poor tracking of channel variations. In addition, the denser the pilot signals, the poorer the bandwidth efficiency.

The pilot-embedding, also referred as pilot-superimposed technique, has been proposed for the SISO systems [17] and for the MIMO systems [59--61], where a sequence of pilot signals is added directly to the data stream. Some soft-decoding methods, such as Viterbi's algorithm [17, 60], are employed for channel estimation and data detection. This technique yields better bandwidth efficiency, since it does not sacrifice any separate time slots for transmitting the pilot signal. The disadvantages of this technique lie in the higher computational complexity of the decoder and the longer delay in channel estimation process.

The purpose of this chapter is to design a novel pilot-embedding approach for ST coded MIMO systems with affordable computational cost and better fast-fading channel acquisition. The basic idea is to simplify channel estimation and data detection processes by taking advantages of the null-space and orthogonality properties of the data-bearer and pilot matrices. The data-bearer matrix is used for projecting the ST data matrix onto the orthogonal subspace of the pilot matrix. By the virtue of the null-space and orthogonality properties, in the proposed data-bearing approach for pilot-embedding, a block of data matrix is added into a block of pilot matrix, that are mutually orthogonal to each other. The benefit that is able to be expected from this approach is better channel estimation performance, since the estimator can take into account the channel variation in the transmitted data block. In addition, a low computational complexity channel estimator is also expected.

Now, the MIMO channel and system models are ready to be described. The MIMO communication system with L_t transmit antennas and L_r receive antennas is considered, as shown in Fig.3.1. In general, for a given block index t, a ST symbol matrix $\mathbf{U}(t)$ is an $L_t \times M$ codeword matrix transmitted across the transmit antennas in M time slots. The

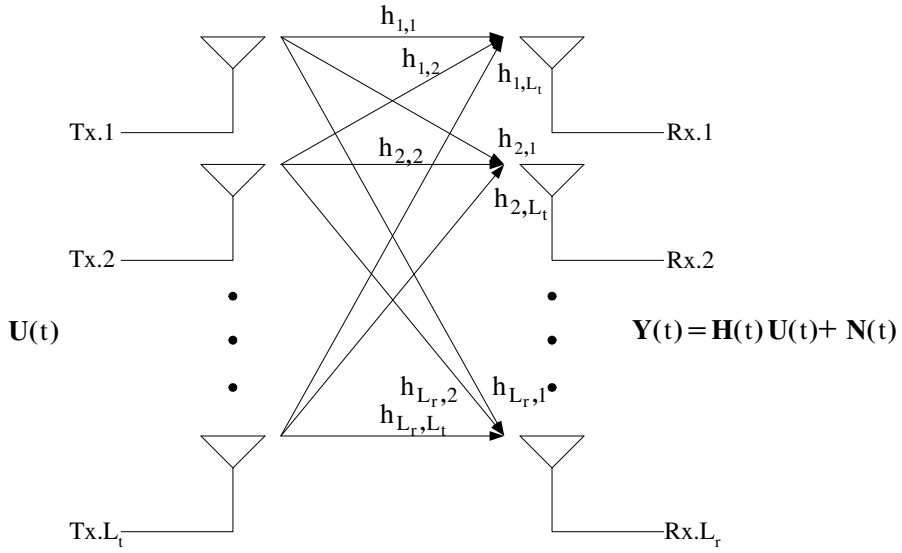

Figure 3.1 A ST MIMO communication system with L_t-transmitter and L_r-receiver.

received symbol matrix $\mathbf{Y}(t)$ at the receiver front-end can be expressed as follows [60],

$$\mathbf{Y}(t) = \mathbf{H}(t)\mathbf{U}(t) + \mathbf{N}(t), \tag{3.1}$$

where $\mathbf{H}(t)$ is the $L_r \times L_t$ channel coefficient matrix and the $L_r \times M$ additive noise matrix $\mathbf{N}(t)$ is complex white Gaussian distributed with zero mean and variance $\frac{\sigma^2}{2}\mathbf{I}_{(L_r M \times L_r M)}$ per real dimension. The elements of $\mathbf{H}(t)$ are assumed to be independent complex Gaussian random variables with zero mean and variance 0.5 per real dimension. Or equivalently, an independent Rayleigh fading channel is assumed. In this chapter, a quasi-static flat Rayleigh fading channel, where $\mathbf{H}(t)$ remains constant over each symbol block but it changes block-by-block independently, is first examined. Then, the proposed scheme will be further examined in a nonquasi-static flat Rayleigh fading channel, where $\mathbf{H}(t)$ is not constant over each symbol block. The problems now are to estimate the channel coefficient matrix $\mathbf{H}(t)$ and the ST symbol matrix $\mathbf{U}(t)$ by using the pilot or training signal embedded in $\mathbf{U}(t)$.

The rest of this chapter is organized as follows. The proposed data-bearing approach for pilot-embedding frameworks is presented in Section 3.2, including general properties needed, channel estimation process, possible data bearer and pilot matrices, and data detection process. Performance analysis for the proposed scheme is carried out in Section 3.3, in terms of channel estimation and data detection. In Section 3.4, the issue of optimum block power allocation for data and pilot parts is addressed. The simulation results are given in

Section 3.5, and the chapter is concluded in Section 3.6.

3.2 The Proposed Data-Bearing Approach for Pilot-Embedding

In this section, the proposed data-bearing approach for pilot-embedding, including the pilot and data extraction procedures, channel estimation, possible data bearer and pilot matrices, and data detection, is presented. The motivation of pursuing pilot-embedding by distributing the pilot signal onto the ST data is to capture the variation of the channel at every instant for achieving a better channel estimate. Without loss of generality, we describe our data matrix $\mathbf{Z}(t) \in \mathbb{C}^{L_t \times M}$ as follows,

$$\mathbf{Z}(t) = \mathbf{D}(t)\mathbf{A}, \tag{3.2}$$

where $\mathbf{D}(t) \in \mathbb{C}^{L_t \times N}$ is the ST data matrix, and $\mathbf{A} \in \mathbb{R}^{N \times M}$ is the data-bearer matrix with N being the number of data time slots. In this implementation, the ST data matrix $\mathbf{D}(t)$ is assumed to maintain the energy constraint $\mathrm{E}[\|\mathbf{D}(t)\|^2] = L_t$ with $\|\cdot\|$ being the Frobenius norm. The proposed pilot-embedded ST symbol matrix $\mathbf{U}(t)$ can be expressed as follows,

$$\mathbf{U}(t) = \mathbf{Z}(t) + \mathbf{P} = \mathbf{D}(t)\mathbf{A} + \mathbf{P}, \tag{3.3}$$

where $\mathbf{P} \in \mathbb{R}^{L_t \times M}$ is the pilot matrix. Unlike the pilot-embedding technique previously proposed in [60] where the pilot-embedded ST symbol matrix $\mathbf{U}(t)$ is expressed as $\mathbf{U}(t) = \mathbf{D}(t) + \mathbf{P}$, the major difference of our proposed scheme in (3.3) is the exploitation of the data-bearer matrix $\mathbf{A}$, which plays the major role along with the pilot matrix $\mathbf{P}$ in the channel estimation and data detection processes.

By the data-bearing approach for pilot-embedding, the data bearer matrix $\mathbf{A}$ and the pilot matrix $\mathbf{P}$ are required to satisfy the following properties:

$$\mathbf{A}\mathbf{P}^T = \mathbf{0} \in \mathbb{R}^{N \times L_t}, \tag{3.4}$$

$$\mathbf{P}\mathbf{A}^T = \mathbf{0} \in \mathbb{R}^{L_t \times N}, \tag{3.5}$$

$$\mathbf{A}\mathbf{A}^T = \beta\mathbf{I} \in \mathbb{R}^{N \times N}, \tag{3.6}$$

$$\mathbf{P}\mathbf{P}^T = \alpha\mathbf{I} \in \mathbb{R}^{L_t \times L_t}, \tag{3.7}$$

where β is a real-valued data-power factor for controlling the value of data-part power, α is a real-valued pilot-power factor for controlling the value of pilot-part power, $\mathbf{0}$ stands for an

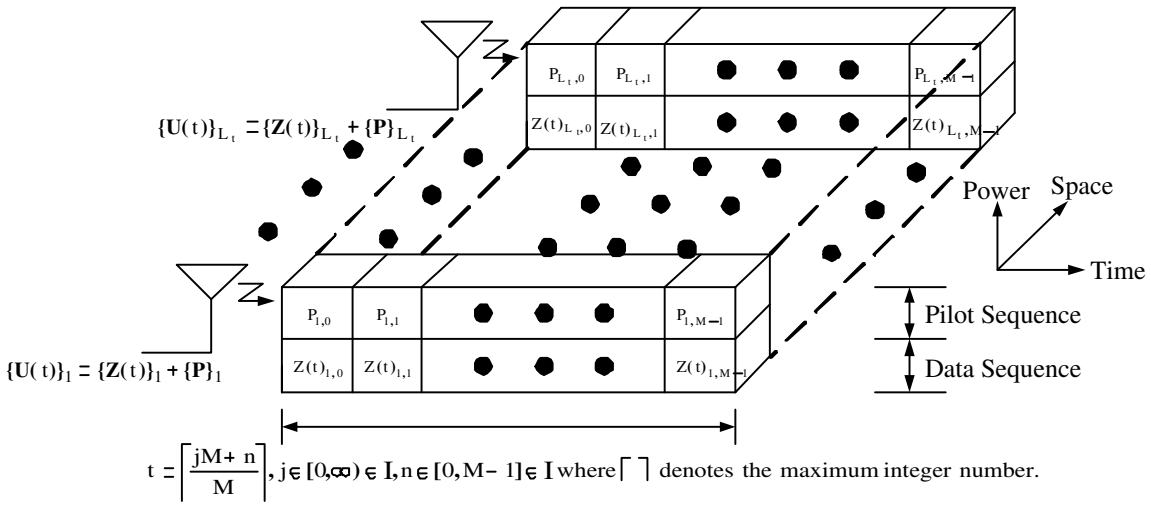

Figure 3.2 The proposed pilot-embedded ST symbol block structure.

all-zero-element matrix, and $\mathbf{I}$ stands for an identity matrix. The key concept of the pilot-embedding approach is the exploitation of the null-space properties [62], i.e. the properties (3.4) and (3.5), and the orthogonality properties [62], i.e. the properties (3.6) and (3.7), about the data-bearer matrix $\mathbf{A}$ and the pilot matrix $\mathbf{P}$. Obviously, in (3.3), the data-bearer matrix $\mathbf{A}$ plays a major role in projecting the ST data matrix $\mathbf{D}(t)$ onto the orthogonal subspace of the pilot matrix $\mathbf{P}$. From (3.6) and (3.7), it implies that $\text{Rank}(\mathbf{A}) = N$ and $\text{Rank}(\mathbf{P}) = L_t$ with $\text{Rank}(\cdot)$ being the rank of a matrix. In order to satisfy the null-space properties in (3.4) and (3.5), the minimum number of the column in $\mathbf{A}$ and $\mathbf{P}$ must be equal to the sum of the rank of $\mathbf{A}$ and $\mathbf{P}$ [63]. Consequently, the number of time slots M of the pilot-embedded ST symbol matrix $\mathbf{U}(t)$ must satisfy the following inequality

$$\text{Rank}(\mathbf{A}) + \text{Rank}(\mathbf{P}) \leq M. \tag{3.8}$$

It is worth noticing that $N < M$ because the excessive time slot, i.e. $M - N$, will be used for providing a room to embed pilot signals.

The proposed pilot-embedded ST symbol block structure is demonstrated in Fig.3.2. The proposed pilot-embedded ST symbol block $\mathbf{U}(t)$ consists of two main parts: data sequences $\{\mathbf{Z}(t)\}_i$ and pilot sequences $\{\mathbf{P}\}_i$, where i stands for a row index, $i = 1, \ldots, L_t$. Substituting (3.3) into (3.1), the received symbol matrix $\mathbf{Y}(t)$ in (3.1) can be rewritten as follows,

$$\mathbf{Y}(t) = \mathbf{H}(t)(\mathbf{D}(t)\mathbf{A} + \mathbf{P}) + \mathbf{N}(t). \tag{3.9}$$

There are at least three possible structures of data-bearer and pilot matrices, in which

the elements of these matrices are real numbers, that satisfy the properties (3.4)-(3.7) as follows.

3.2.0.1 Time-Multiplexing Based Matrices

The structures of these matrices are given as

$$\mathbf{A} = \sqrt{\beta}\left[\mathbf{0}_{(N\times L_t)}; \mathbf{I}_{(N\times N)}\right],$$
$$\mathbf{P} = \sqrt{\alpha}\left[\mathbf{I}_{(L_t\times L_t)}; \mathbf{0}_{(L_t\times N)}\right],\ M = N + L_t. \tag{3.10}$$

In this structure, the $L_t \times L_t$ identity matrix $\mathbf{I}$ is used as a pilot or training symbol. In addition, PSAM belongs to this category [16], because it employs the time-multiplexing structure for pilot and data allocation, and has been used in many literatures [54]- [57]. Therefore, the existing PSAM technique is subsumed in the proposed general idea in (3.3).

3.2.0.2 ST-Block-Code Based Matrices

The structures of these matrices are given as

$$\mathbf{A} = \sqrt{\beta}\left[\mathbf{0}_{(N\times \tau)}; \mathbf{I}_{(N\times N)}\right],$$
$$\mathbf{P} = \sqrt{\alpha}\left[\text{STBC}_{(L_t\times \tau)}; \mathbf{0}_{(L_t\times N)}\right],\ M = N + \tau, \tag{3.11}$$

where τ is the number of time slots used for transmitting one ST block code. In addition, $\tau \geq L_t$ depending on the structure of the chosen ST block code. In this structure, the major difference from the TM-based structure is that it employs the normalized known ST block code [14] as the pilot symbol instead of using the identity matrix. It also inherits the time-multiplexing structure in pilot and data allocation. This kind of data bearer and pilot matrices have been used in [53], for instance.

3.2.0.3 Code-Multiplexing Based Matrices

The structures of these matrices are given as

$$\mathbf{A} = \sqrt{\beta}\text{WH}[1:N]_{(N\times M)},$$
$$\mathbf{P} = \sqrt{\alpha}\text{WH}[N+1:M]_{(L_t\times M)},\ M = N + L_t, \tag{3.12}$$

where $\text{WH}[x:y]$ denotes a sub-matrix created by splitting the $M \times M$ normalized Walsh-Hadamard matrix [64] starting from x^{th}-row to y^{th}-row. Unlike the time-multiplexing

structure employed for pilot and data allocation in the TM-based and the STBC-based structures, in this structure, the code-multiplexing structure is employed instead. Because of the even distribution inherited from the code-multiplexing structure over the transmitted ST symbol block, the superior channel estimation performance over the other two structures could, therefore, be expected. The disadvantage of this structure is the limitation of dimensionality of Walsh-Hadamard matrix, which has a dimension proportionally to $2^n,\ n \in \mathbb{I}$. In addition, this structure provides an instructive example of the proposed general idea in (3.3) for pilot-embedding.

It is worth mentioning that the proposed data-bearing approach for pilot-embedding frameworks subsumes the general idea of the existing pilot-based techniques, i.e. PSAM and pilot-embedding techniques. In addition, the designed criteria in (3.6) and (3.7), and the above three examples satisfy the optimal designed criteria in [57], i.e. the optimal training data and the optimal training interval length, respectively. In what follows, the problems of channel estimation and ST data detection in conjunction with the aforementioned data-bearing approach are further considered.

3.2.1 Channel Estimation

The channel estimation of the proposed data-bearing approach for pilot-embedding frameworks can be achieved by first simply post-multiplying the received symbol matrix $\mathbf{Y}(t)$ in (3.9) by the transpose of the pilot matrix $\mathbf{P}^T$ for extracting the pilot part. Using (3.4) and (3.7), and dividing the result by α, thus yielding

$$\frac{\mathbf{Y}(t)\mathbf{P}^T}{\alpha} = \mathbf{H}(t) + \frac{\mathbf{N}(t)\mathbf{P}^T}{\alpha}. \tag{3.13}$$

Denoting $\mathbf{y}(t)$,$\mathbf{n}(t)$, and $\mathbf{h}(t)$ as the vectorized version of $\frac{\mathbf{Y}(t)\mathbf{P}^T}{\alpha}$,$\frac{\mathbf{N}(t)\mathbf{P}^T}{\alpha}$, and $\mathbf{H}(t)$ respectively, i.e. the equation (3.13) can be rewritten as follows,

$$\mathbf{y}(t) = \mathbf{h}(t) + \mathbf{n}(t). \tag{3.14}$$

For the pilot-projected noise vector $\mathbf{n}(t)$, using the following relationship [65]

$$\mathbf{vec}(\mathbf{ABC}) = (\mathbf{C}^T \otimes \mathbf{A})\mathbf{vec}(\mathbf{B}), \tag{3.15}$$

where $\otimes$ is the Kronecker product, we have

$$\mathbf{n}(t) = \frac{1}{\alpha}(\mathbf{I} \otimes \mathbf{N}(t))\mathbf{vec}(\mathbf{P}^T) \tag{3.16}$$

where the size of $\mathbf{I} \otimes \mathbf{N}(t)$ is $L_t L_r \times L_t M$. In the above, the Kronecker product of the matrices $\mathbf{A}$ and $\mathbf{B}$ is defined as

$$\mathbf{A} \otimes \mathbf{B} = \begin{pmatrix} a_{1,1}\mathbf{B} & & a_{1,c}\mathbf{B} \\ & \ddots & \\ a_{r,1}\mathbf{B} & & a_{r,c}\mathbf{B} \end{pmatrix}, \tag{3.17}$$

where c and r stand for the numbers of column vectors and row vectors of the matrix $\mathbf{A}$, respectively. From the white Gaussian-distributed assumption of $\mathbf{N}(t)$, the mean vector and the covariance matrix of the pilot-projected noise vector $\mathbf{n}(t)$ are determined as follows,

$$\boldsymbol{\mu}_{\mathbf{n}(t)} = \frac{1}{\alpha}\mathrm{E}[(\mathbf{I} \otimes \mathbf{N}(t))\mathbf{vec}(\mathbf{P}^T)] = \mathbf{0}_{(L_t L_r \times 1)}, \tag{3.18}$$

$$\begin{aligned} \mathbf{V}_{\mathbf{n}(t)} = \ & \tfrac{1}{\alpha^2}\mathrm{E}[((\mathbf{I} \otimes \mathbf{N}(t))\mathbf{vec}(\mathbf{P}^T))((\mathbf{I} \otimes \mathbf{N}(t))\mathbf{vec}(\mathbf{P}^T))^H] = \tfrac{\sigma^2}{2\alpha^2}\mathrm{Diag}\left(B_i\right), \\ & B_i = \textstyle\sum_{j=1}^{M} |P_{i,j}|^2 \mathbf{I}_{(L_r \times L_r)},\ i \in \{1, \ldots, L_t\},\ \text{per real dimension}, \end{aligned} \tag{3.19}$$

where $P_{i,j}$ is the i^{th}-row j^{th}-column element of the pilot matrix $\mathbf{P}$, Diag$(\cdot)$ stands for the diagonal matrix created by concatenating submatrices $B_i,\ i \in 1, \ldots, L_t$, into the diagonal elements.

From (3.7), it implies that $\sum_{j=1}^{M} |P_{i,j}|^2 = \alpha,\ \forall i$. Hence, we can rewrite (3.19) as follows,

$$\mathbf{V}_{\mathbf{n}(t)} = \frac{\sigma^2}{2\alpha}\mathbf{I}_{(L_t L_r \times L_t L_r)},\ \text{per real dimension}. \tag{3.20}$$

Obviously, the pilot-projected noise vector $\mathbf{n}(t)$ is a complex white Gaussian vector, hence, the log-likelihood function $\ln(p(\mathbf{y}(t)|\mathbf{h}(t)))$ is given by [18]

$$\ln(p(\mathbf{y}(t)|\mathbf{h}(t))) = \ln\left(\frac{1}{\pi^L det(\mathbf{V}_{\mathbf{n}(t)})}\right) - (\mathbf{y}(t) - \mathbf{h}(t))^H \mathbf{V}_{\mathbf{n}(t)}^{-1}(\mathbf{y}(t) - \mathbf{h}(t)), \tag{3.21}$$

where $L = L_r L_t$.

3.2.1.1 Unconstrained Maximum-Likelihood Channel Estimator

It is straightforward to show that the maximum-likelihood estimator [18] maximizing the log-likelihood function $\ln(p(\mathbf{y}(t)|\mathbf{h}(t)))$ is as follows,

$$\hat{\mathbf{h}}(t) = \max_{\mathbf{h}(t)}\{\ln(p(\mathbf{y}(t)|\mathbf{h}(t)))\} = \mathbf{y}(t) \text{ or } \hat{\mathbf{H}}(t) = \frac{\mathbf{Y}(t)\mathbf{P}^T}{\alpha}, \tag{3.22}$$

meaning that the unconstrained ML estimator is the pilot-projected received vector $\mathbf{y}(t)$ itself.

3.2.1.2 Linear Minimum Mean-Squared Error Channel Estimator

The performance of the unconstrained ML channel estimator in (3.22) is further improved by employing the L-tap LMMSE channel interpolation. The L-tap LMMSE channel estimator can be expressed as follows,

$$h_{j,i}^{LMMSE}(t) = \mathbf{w}_{j,i}^{H}\hat{\mathbf{h}}_{j,i}^{L}(t), \tag{3.23}$$

where $h_{j,i}^{LMMSE}(t)$ denotes the j^{th}-row i^{th}-column element of the LMMSE-estimated channel matrix, $\mathbf{w}_{j,i} = [w_{j,i}(0)\cdots w_{j,i}(L-1)]^T$ denotes the L-tap finite impulse response (FIR) linear filter's weight vector, and $\hat{\mathbf{h}}_{j,i}^{L}(t) = [\hat{h}_{j,i}(t)\cdots\hat{h}_{j,i}(t-L+1)]^T$ denotes the L-element input vector constructed from the j^{th}-row i^{th}-column element of the ML-estimated channel matrix in (3.22) taking values in the time interval $[t-L+1, t]$. The optimization criterion, assuming the channels are WSS, for the L-tap LMMSE channel estimator is given by

$$J(\mathbf{w}_{j,i}) = \arg\min_{\mathbf{w}_{j,i}} \mathrm{E}\left[\|h_{j,i}(t) - \mathbf{w}_{j,i}^{H}\hat{\mathbf{h}}_{j,i}^{L}(t)\|^2\right], \tag{3.24}$$

where $h_{j,i}(t)$ denotes the j^{th}-row i^{th}-column element of the true channel matrix $\mathbf{H}(t)$ in (3.1).

The optimum LMMSE weight vector $\mathbf{w}_{j,i}^{opt}$ is given by

$$\mathbf{w}_{j,i}^{opt} = \mathbf{R}_{\hat{\mathbf{h}}_{j,i}^{L}(t)}^{-1}\mathbf{p}_{\hat{\mathbf{h}}_{j,i}^{L}(t)}, \tag{3.25}$$

where $\mathbf{R}_{\hat{\mathbf{h}}_{j,i}^{L}(t)} = \mathrm{E}[\hat{\mathbf{h}}_{j,i}^{L}(t)\hat{\mathbf{h}}_{j,i}^{H_L}(t)]$ and $\mathbf{p}_{\hat{\mathbf{h}}_{j,i}^{L}(t)} = \mathrm{E}[h_{j,i}^{*}(t)\hat{\mathbf{h}}_{j,i}^{L}(t)]$. According to (3.14), (3.20), (3.22), and the uncorrelatedness of the channel and noise coefficients, the L-tap LMMSE channel estimator can be further rewritten as

$$h_{j,i}^{LMMSE}(t) = \left[(\mathbf{R}_{\mathbf{h}_{j,i}^{L}(t)} + \frac{\sigma^2}{\alpha}\mathbf{I}_{L\times L})^{-1}\mathbf{p}_{\mathbf{h}_{j,i}^{L}(t)}\right]^{H}\hat{\mathbf{h}}_{j,i}^{L}(t), \tag{3.26}$$

where $\mathbf{R}_{\mathbf{h}_{j,i}^{L}(t)} = \mathrm{E}[\mathbf{h}_{j,i}^{L}(t)\mathbf{h}_{j,i}^{H_L}(t)]$ and $\mathbf{p}_{\hat{\mathbf{h}}_{j,i}^{L}(t)} = \mathrm{E}[h_{j,i}^{*}(t)\mathbf{h}_{j,i}^{L}(t)] = \mathbf{p}_{\mathbf{h}_{j,i}^{L}(t)}$. The performance analysis for the unconstrained ML channel estimator will be considered in section 3.3.1.1. In addition, the performance analysis for the LMMSE channel estimator can be found in [57].

3.2.2 Data Detection

The data detection procedure is further performed. Firstly, the data part in the received symbol matrix $\mathbf{Y}(t)$ is extracted by post-multiplying the received symbol matrix $\mathbf{Y}(t)$ by

the transpose of the data-bearer matrix $\mathbf{A}^T$. Using (3.5) and (3.6), we have

$$\frac{\mathbf{Y}(t)\mathbf{A}^T}{\beta} = \mathbf{H}(t)\mathbf{D}(t) + \frac{\mathbf{N}(t)\mathbf{A}^T}{\beta}. \tag{3.27}$$

Defining $\mathbf{n}^{'}(t)$ as the vector version of $\frac{\mathbf{N}(t)\mathbf{A}^T}{\beta}$. From (3.6), it implies that $\sum_{j=1}^{M} |A_{i,j}|^2 = \beta,\ \forall i$. Then similar to (3.18) and (3.19), the mean vector and the covariance matrix of the data-bearer-projected noise vector $\mathbf{n}^{'}(t)$ are determined as follows,

$$\boldsymbol{\mu}_{\mathbf{n}^{'}(t)} = \mathbf{0}_{(L_r N \times 1)}, \tag{3.28}$$

$$\mathbf{V}_{\mathbf{n}^{'}(t)} = \frac{\sigma^2}{2\beta}\mathbf{I}_{(L_r N \times L_r N)} \text{ per real dimension.} \tag{3.29}$$

The ML receiver is employed for decoding the transmitted ST data matrix $\mathbf{D}(t)$ by using the estimated channel coefficient matrix $\hat{\mathbf{H}}(t)$ obtained in either (3.22) or (3.26) as the channel state information. Due to the i.i.d. white Gaussian distribution of $\mathbf{n}^{'}(t)$, the ML receiver computes the decision metric and decides the codeword that minimizes this decision metric as in [13],

$$\{\hat{d}_t^i\} = \min_{\{d_t^i\}} \left\{ \sum_{t=1}^{N} \sum_{j=1}^{L_r} |y_t^j - \sum_{i=1}^{L_t} \hat{h}_{j,i} d_t^i|^2 \right\},\ \forall d_t^i,\ i \in \{1, \ldots, L_t\},\ t \in \{1, \ldots, N\}, \tag{3.30}$$

where y_t^j denotes the j^{th}-row t^{th}-column element of the data-bearer-projected received symbol matrix $\frac{\mathbf{Y}(t)\mathbf{A}^T}{\beta}$, $\hat{h}_{j,i}$ denotes the j^{th}-row i^{th}-column element of the estimated channel coefficient matrix $\hat{\mathbf{H}}(t)$, and $\hat{d}_t^i$ denotes the i^{th}-row t^{th}-column element of the estimated ST data matrix $\hat{\mathbf{D}}(t)$.

The performance analysis for the ST data detection is discussed in section 3.3.1.2. Note that the null-space and orthogonality properties of the data-bearer matrix $\mathbf{A}$ and the pilot matrix $\mathbf{P}$ play the major role in the pilot and the data extraction for channel estimation and data detection, respectively. In addition, the ranks of the data-bearer matrix $\mathbf{A}$ and the pilot matrix $\mathbf{P}$ also determine the minimum number of time slots, obtained in (3.8), of the pilot-embedded ST symbol matrix $\mathbf{U}(t)$.

3.3 The Performance Analysis for The Proposed Scheme

In this section, the performances of the data-bearing approach for pilot-embedding frameworks are analyzed, including both the unconstrained ML channel estimation and data

detection performance, under two different scenarios, i.e. quasi-static and nonquasi-static flat Rayleigh fading channels. This analysis will be used as the theoretical benchmarks for later comparisons in Section 3.5.

3.3.1 Quasi-static Flat Rayleigh Fading Channels

3.3.1.1 Channel Estimation Performance Analysis

The channel estimation error is first analyzed, and then it will be compared to the Cramer-Rao lower bound (CRLB), which is a lower bound of the conditional variance of the channel estimation error.

3.3.1.1.1) Channel Estimation Error: A channel estimation error vector can be evaluated as follows,

$$\tilde{\mathbf{h}}(t) = \mathbf{h}(t) - \hat{\mathbf{h}}(t). \tag{3.31}$$

Substituting (3.22) into (3.31), the variance matrix of the channel estimation error is given by

$$\text{Var}\left[\tilde{\mathbf{h}}(t)\right] = \text{E}\left[(\mathbf{h}(t) - \mathbf{h}(t) - \mathbf{n}(t))(\mathbf{h}(t) - \mathbf{h}(t) - \mathbf{n}(t))^H\right] = \mathbf{V}_{\mathbf{n}(t)}. \tag{3.32}$$

The mean-squared error (MSE) of the channel estimation is given by

$$\text{MSE} \;=\; \text{tr}\left\{\text{Var}\left[\tilde{\mathbf{h}}(t)\right]\right\} = \frac{\sigma^2 L_t L_r}{\alpha}, \tag{3.33}$$

where tr$\{\cdot\}$ stands for the trace operator of a matrix.

It is worth noticing that the MSE of the channel estimation is inversely proportional to the pilot-power factor α; as a result, more power allocated to the pilot part resulting in lower MSE of the channel estimation.

3.3.1.1.2) Unbiasedness and Cramer-Rao Lower Bound: Since the proposed estimator achieves the CRLB because it is the maximum-likelihood estimator in the presence of the AWGN [18], it can be shown that the estimator is unbiased. Using (3.18), the unbiasedness of the proposed pilot-embedded channel estimator is evaluated by

$$\text{E}[\hat{\mathbf{h}}(t)] = \text{E}\left[\mathbf{h}(t) + \mathbf{n}(t)\right] = \boldsymbol{\mu}_{\mathbf{h}(t)}. \tag{3.34}$$

The CRLB for an unbiased estimator is defined as [18]

$$\text{Cov}\left[\hat{\mathbf{h}}(t) - \mathbf{h}(t)|\mathbf{h}(t)\right] = \left[-\text{E}\left[\frac{\partial^2 \ln(p(\mathbf{y}(t)|\mathbf{h}(t)))}{\partial \mathbf{h}^2(t)}\right]\right]^{-1} = \mathbf{V}_{\mathbf{n}(t)}. \tag{3.35}$$

The trace of the CRLB matrix in (3.35) is given by

$$\mathrm{tr}\left\{\mathrm{Cov}\left[\hat{\mathbf{h}}(t)-\mathbf{h}(t)|\mathbf{h}(t)\right]\right\}=\frac{\sigma^2 L_t L_r}{\alpha}. \tag{3.36}$$

Therefore, one can see that the channel estimator achieves the desired properties of a good estimator that is unbiased, and achieves the CRLB.

3.3.1.2 Data Detection Performance Analysis

The probability of error of the proposed scheme in data detection is further analyzed. A Chernoff's upper bound of the probability of transmitting a codeword $\mathbf{d} \triangleq (d_1^1 d_1^2 \cdots d_1^{L_t} \cdots d_N^1 d_N^2 \cdots d_N^{L_t})^T$ and deciding in favor of a different codeword $\mathbf{e} \triangleq (e_1^1 e_1^2 \cdots e_1^{L_t} \cdots e_N^1 e_N^2 \cdots e_N^{L_t})^T$ at the maximum-likelihood receiver is given by [50]

$$P\left(\mathbf{d}\rightarrow\mathbf{e}|\hat{h}_{j,i},\ j=1,\ldots,L_r,\ i=1,\ldots,L_t\right)\leq\exp\left(\frac{-m^2\left(\mathbf{d},\mathbf{e}\right)}{4N_0}\right), \tag{3.37}$$

where $m^2\left(\mathbf{d},\mathbf{e}\right)=\sum_{j=1}^{L_r}\sum_{t=1}^{N}|\sum_{i=1}^{L_t}\hat{h}_{j,i}(d_t^i-e_t^i)|^2$ and $N_0=\frac{\sigma^2}{N}\left(\frac{N}{\beta}+\frac{L_t}{\alpha}\right)$ is the noise variance of the noise term in the decision metric (3.30), when the estimated channel coefficient matrix $\hat{\mathbf{H}}(t)$ expressed in (3.22) and the data-bearer-projected received symbol matrix $\frac{\mathbf{Y}(t)\mathbf{A}^T}{\beta}$ obtained in (3.27) are substituted. More specifically, since the pilot-projected noise vector $\mathbf{n}(t)$ and the data-bearer-projected noise vector $\mathbf{n}'(t)$ are i.i.d Gaussian distributed with zero mean and variance matrices were shown in (3.20) and (3.29), respectively, the noise variance N_0 is the combination of the total variances of these noise vectors divided by the number of receive antennas L_r and the data time slots N, given by $N_0=\frac{\sigma^2}{L_r N}\left(\frac{NL_r}{\beta}+\frac{L_t L_r}{\alpha}\right)$.

From (3.37) and the derivations in [13], the Chernoff's upper bound of the probability of error can be rewritten as follows,

$$P\left(\mathbf{d}\rightarrow\mathbf{e}|\hat{h}_{j,i},\ j=1,\ldots,L_r,\ i=1,\ldots,L_t\right)\leq\prod_{j=1}^{L_r}\exp\left\{-\frac{1}{4N_0}\sum_{i=1}^{L_t}\lambda_i|Q_{j,i}|^2\right\}, \tag{3.38}$$

where λ_i is the eigenvalue of the code-error matrix $\mathbf{C}(\mathbf{d},\mathbf{e})$ defined as $C_{p,q}=\mathbf{x}_q^H\mathbf{x}_p$ where $\mathbf{x}_p=(d_1^P-e_1^P,\ldots,d_N^P-e_N^P)^T$, $Q_{j,i}\in(Q_{j,1},\ldots,Q_{j,L_t})=\mathbf{\Omega}_j^T\mathbf{V}^H$, where $\mathbf{\Omega}_j=(\hat{h}_{j,1},\ldots,\hat{h}_{j,L_t})^T$ and $\mathbf{V}$ is the eigenmatrix whose rows correspond to the eigenvectors of $\mathbf{C}(\mathbf{d},\mathbf{e})$. Since $\mathbf{V}$ is unitary, then, $Q_{j,i}$ are independent complex Gaussian random variables with zero mean and variance is given by

$$\begin{aligned}\sigma_Q^2 &= \mathrm{E}\left[h_{j,i}h_{j,i}^*\right]+\mathrm{E}\left[N_{j,i}(t)N_{j,i}(t)^*\right]\\ &= 0.5+\frac{\sigma^2}{2\alpha}\ \text{per real dimension},\end{aligned} \tag{3.39}$$

where $N_{j,i}(t)$ is the j^{th}-row i^{th}-column element of the pilot-projected noise matrix $\mathbf{N}_1(t)$ in (3.13). Thus, $|Q_{j,i}|$ are independent Rayleigh distributions with pdf

$$p(|Q_{j,i}|) = \frac{2|Q_{j,i}|}{\sigma_Q^2} \exp\left(-\frac{|Q_{j,i}|^2}{\sigma_Q^2}\right) \tag{3.40}$$

for $|Q_{j,i}| \geq 0$.

The Chernoff's upper bound of the average probability of error can be computed by averaging (3.38) with respect to independent Rayleigh distributions of $|Q_{j,i}|$ to arrive at

$$\begin{aligned} P(\mathbf{d} \to \mathbf{e})_{\hat{\mathbf{H}}(t)} &\leq \prod_{i=1}^{L_t} \left(\frac{1}{1 + \frac{\sigma_Q^2 \lambda_i}{\frac{4}{N}\left(\frac{N}{\beta} + \frac{L_t}{\alpha}\right)\sigma^2}} \right)^{L_r} \\ &\leq \left(\prod_{i=1}^{L_t} \lambda_i \right)^{-L_r} \left(\frac{\sigma_Q^2}{\frac{4}{N}\left(\frac{N}{\beta} + \frac{L_t}{\alpha}\right)\sigma^2} \right)^{-L_t L_r}, \end{aligned} \tag{3.41}$$

assuming that full rank ST codes are employed, which can be relaxed in general.

In comparison to the case that the channel coefficient matrix $\mathbf{H}(t)$ is exactly available to the maximum-likelihood receiver, the average probability of error is given in [13] as,

$$P(\mathbf{d} \to \mathbf{e})_{\mathbf{H}(t)} \leq \left(\prod_{i=1}^{L_t} \lambda_i \right)^{-L_r} \left(\frac{P_s}{4\sigma^2} \right)^{-L_t L_r}, \tag{3.42}$$

where P_s is the normalized power allocated to the data part when the channel coefficients are known.

Notice that the noise variance N_0 is affected by the variances of the channel estimation error, i.e. $\frac{\sigma^2}{\alpha}$, and the data-bearer-projected noise, i.e. $\frac{\sigma^2}{\beta}$; therefore, it completely reveals the underlined effects of pilot- and data-power factors in the probability of error. Hence, this probability of error can be reasonably used as a cost function for optimum power allocation purpose.

Defining the probability of error upper bound (PEUB) mismatch factor between the estimated channel coefficient case and the ideal channel coefficient case as follows,

$$\begin{aligned} \eta &= \ln\left(\frac{P(\mathbf{d} \to \mathbf{e})_{\hat{\mathbf{H}}(t)}}{P(\mathbf{d} \to \mathbf{e})_{\mathbf{H}(t)}} \right) \\ &= L_t L_r \ln\left(\frac{P_s\left(\frac{N}{\beta} + \frac{L_t}{\alpha}\right)}{N(1 + \frac{\sigma^2}{\alpha})} \right). \end{aligned} \tag{3.43}$$

This PEUB mismatch factor is used for performance measure in order to optimally allocate the powers to the data and pilot parts. In other words, this factor is minimized when the power is allocated optimally. The advantage of using this PEUB mismatch factor as a cost function for optimum power allocation inherits directly from its expression that takes both the channel estimation error and the effect of the data-bearer-projected noise into account. In addition, the use of the PEUB mismatch factor as a cost function for the optimum power allocation is better than using the channel estimation error as the cost function merely, because, under the constant power constraint, despite the fact that assigning a larger power to the pilot part yields better channel coefficient estimates, i.e. a lower channel estimation error; the remaining smaller amount of power given to the data part yields a poorer probability of error in decoding. Hence, this power tradeoff is essential for the overall performances of the pilot-embedded MIMO system, e.g. channel estimation error and the probability of detection error.

3.3.2 Nonquasi-static Flat Rayleigh Fading Channels

When the channel changes rapidly, the assumption of quasi-static fading channels is no longer held anymore. Appropriate channel estimation approaches have to be designed and analyzed for combatting such channel situations. In what follows, the performance of the proposed scheme for nonquasi-static flat Rayleigh fading channels is investigated. For the sake of exposition, a half-block fading channel model, in which the channel coefficient matrix $\mathbf{H}(t)$ symmetrically changes once within one ST symbol block, i.e. there exists $\mathbf{H}_1(t)$ and $\mathbf{H}_2(t)$ in the t^{th}-block ST symbol matrix, is studied. With $\mathbf{P} = [\mathbf{P}_1; \mathbf{P}_2]$ and $\mathbf{A} = [\mathbf{A}_1; \mathbf{A}_2]$, the received symbol matrix in (3.9) can be rewritten as follows,

$$\mathbf{Y}(t) = [\mathbf{H}_1(t)(\mathbf{D}(t)\mathbf{A}_1 + \mathbf{P}_1); \mathbf{H}_2(t)(\mathbf{D}(t)\mathbf{A}_2 + \mathbf{P}_2)] + \mathbf{N}(t), \tag{3.44}$$

where $\mathbf{H}_1(t)$, $\mathbf{A}_1$ and $\mathbf{P}_1$ denote the first part of the channel coefficient, the data bearer, and the pilot matrices, respectively; $\mathbf{H}_2(t)$, $\mathbf{A}_2$ and $\mathbf{P}_2$ denote the second part of the channel coefficient, the data bearer, and the pilot matrices, respectively. In addition, the readers are reminded about the properties of matrices $\mathbf{A}$ and $\mathbf{P}$ in (3.4)-(3.7). First, the ML channel estimation in (3.22) is computed. From the received symbol matrix in (3.44), it is post multiplied by $\mathbf{P}^T$, divided the result by α, and rearranged the terms, the channel estimate

can be expressed as follows

$$\hat{\mathbf{H}}(t) = \frac{1}{\alpha}[\mathbf{H}_1(t)\mathbf{D}(t)\mathbf{A}_1\mathbf{P}_1^T + \mathbf{H}_2(t)\mathbf{D}(t)\mathbf{A}_2\mathbf{P}_2^T] + \frac{1}{\alpha}[\mathbf{H}_1(t)\mathbf{P}_1\mathbf{P}_1^T + \mathbf{H}_2(t)\mathbf{P}_2\mathbf{P}_2^T] + \mathbf{N}_1(t), \tag{3.45}$$

where $\mathbf{N}_1(t) = \frac{\mathbf{N}(t)\mathbf{P}^T}{\alpha}$. Next, the data extraction is computed by post multiplying (3.44) by $\mathbf{A}^T$, dividing the result by β, and rearranging the terms to arrive at

$$\mathbf{Y}_1(t) = \frac{1}{\beta}[\mathbf{H}_1(t)\mathbf{D}(t)\mathbf{A}_1\mathbf{A}_1^T + \mathbf{H}_2(t)\mathbf{D}(t)\mathbf{A}_2\mathbf{A}_2^T] + \frac{1}{\beta}[\mathbf{H}_1(t)\mathbf{P}_1\mathbf{A}_1^T + \mathbf{H}_2(t)\mathbf{P}_2\mathbf{A}_2^T] + \mathbf{N}_2(t), \tag{3.46}$$

where $\mathbf{N}_2(t) = \frac{\mathbf{N}(t)\mathbf{A}^T}{\beta}$

As an illustrating example, the case where $L_t = 2,\ L_r = 2,\ \tau = 2,\ N = 2,$ and $M = N + L_t = 4$ is investigated.

- *TM- & STBC-Based Matrices:*

According to (3.10) and (3.11), respectively, the data-bearer and pilot matrices can be designed as follows,

$$\mathbf{A}_{TM} = \sqrt{\beta}\begin{pmatrix} \underbrace{\begin{matrix} 0 & 0 \\ 0 & 0 \end{matrix}}_{\mathbf{A}_{T_1}} & \underbrace{\begin{matrix} 1 & 0 \\ 0 & 1 \end{matrix}}_{\mathbf{A}_{T_2}} \end{pmatrix}, \qquad \mathbf{P}_{TM} = \sqrt{\alpha}\begin{pmatrix} \underbrace{\begin{matrix} 1 & 0 \\ 0 & 1 \end{matrix}}_{\mathbf{P}_{T_1}} & \underbrace{\begin{matrix} 0 & 0 \\ 0 & 0 \end{matrix}}_{\mathbf{P}_{T_2}} \end{pmatrix}$$

and

$$\mathbf{A}_{STBC} = \sqrt{\beta}\begin{pmatrix} \underbrace{\begin{matrix} 0 & 0 \\ 0 & 0 \end{matrix}}_{\mathbf{A}_{S_1}} & \underbrace{\begin{matrix} 1 & 0 \\ 0 & 1 \end{matrix}}_{\mathbf{A}_{S_2}} \end{pmatrix}, \qquad \mathbf{P}_{STBC} = \sqrt{\alpha}\begin{pmatrix} \underbrace{\begin{matrix} \frac{1}{\sqrt{2}} & -\frac{1}{\sqrt{2}} \\ \frac{1}{\sqrt{2}} & \frac{1}{\sqrt{2}} \end{matrix}}_{\mathbf{P}_{S_1}} & \underbrace{\begin{matrix} 0 & 0 \\ 0 & 0 \end{matrix}}_{\mathbf{P}_{S_2}} \end{pmatrix}. \tag{3.47}$$

From the matrix design in (3.47), it can be shown that

$$\mathbf{A}_{T_1}\mathbf{P}_{T_1}^T = \mathbf{A}_{T_2}\mathbf{P}_{T_2}^T = \mathbf{P}_{T_2}\mathbf{P}_{T_2}^T = \mathbf{A}_{T_1}\mathbf{A}_{T_1}^T = \mathbf{0}_{(2\times 2)},$$
$$\mathbf{P}_{T_1}\mathbf{P}_{T_1}^T = \alpha\mathbf{I}_{(2\times 2)},\ \text{and}\ \mathbf{A}_{T_2}\mathbf{A}_{T_2}^T = \beta\mathbf{I}_{(2\times 2)}. \tag{3.48}$$

Similarly, for the STBC-based matrices, the derivation in (3.48) is also applied, except the notation. Substituting (3.48) into (3.45) and (3.46), thus yielding, respectively,

$$\hat{\mathbf{H}}_{TM\&STBC}(t) = \mathbf{H}_1(t) + \mathbf{N}_1(t). \tag{3.49}$$

$$\mathbf{Y}_{1_{TM\&STBC}}(t) = \mathbf{H}_2(t)\mathbf{D}(t) + \mathbf{N}_2(t). \tag{3.50}$$

- *CM Matrices:*

According to (3.12), the data-bearer and pilot matrices can be designed as follows,

$$\mathbf{A}_{CM} = \sqrt{\beta}\begin{pmatrix} \underbrace{\begin{matrix}\frac{1}{2} & \frac{1}{2}\\ \frac{1}{2} & -\frac{1}{2}\end{matrix}}_{\mathbf{A}_{C_1}} & \underbrace{\begin{matrix}\frac{1}{2} & \frac{1}{2}\\ \frac{1}{2} & -\frac{1}{2}\end{matrix}}_{\mathbf{A}_{C_2}} \end{pmatrix}, \qquad \mathbf{P}_{CM} = \sqrt{\alpha}\begin{pmatrix} \underbrace{\begin{matrix}\frac{1}{2} & \frac{1}{2}\\ \frac{1}{2} & -\frac{1}{2}\end{matrix}}_{\mathbf{P}_{C_1}} & \underbrace{\begin{matrix}-\frac{1}{2} & -\frac{1}{2}\\ -\frac{1}{2} & \frac{1}{2}\end{matrix}}_{\mathbf{P}_{C_2}} \end{pmatrix} \tag{3.51}$$

In a similar way to (3.48), it can be shown that

$$\begin{gathered}\mathbf{P}_{C_1}\mathbf{P}_{C_1}^T = \mathbf{P}_{C_2}\mathbf{P}_{C_2}^T = \tfrac{\alpha}{2}\mathbf{I}_{(2\times 2)},\ \mathbf{A}_{C_1}\mathbf{A}_{C_1}^T = \mathbf{A}_{C_2}\mathbf{A}_{C_2}^T = \tfrac{\beta}{2}\mathbf{I}_{(2\times 2)},\\ \mathbf{A}_{C_1}\mathbf{P}_{C_1}^T = \tfrac{\sqrt{\beta\alpha}}{2}\mathbf{I}_{(2\times 2)},\ \text{and}\ \mathbf{A}_{C_2}\mathbf{P}_{C_2}^T = -\tfrac{\sqrt{\beta\alpha}}{2}\mathbf{I}_{(2\times 2)}.\end{gathered} \tag{3.52}$$

Substituting (3.52) into (3.45) and (3.46), thus yielding, respectively,

$$\hat{\mathbf{H}}_{CM}(t) = \frac{1}{2}[\mathbf{H}_1(t) + \mathbf{H}_2(t)] + \frac{1}{2}\sqrt{\frac{\beta}{\alpha}}[\mathbf{H}_1(t) - \mathbf{H}_2(t)]\mathbf{D}(t) + \mathbf{N}_1(t). \tag{3.53}$$

$$\mathbf{Y}_{1_{CM}}(t) = \frac{1}{2}[\mathbf{H}_1(t) + \mathbf{H}_2(t)]\mathbf{D}(t) + \frac{1}{2}\sqrt{\frac{\alpha}{\beta}}[\mathbf{H}_1(t) - \mathbf{H}_2(t)] + \mathbf{N}_2(t). \tag{3.54}$$

3.3.2.1 Channel Estimation Performance Analysis

In the following analysis, the channel estimation error for the TM-, STBC-, CM-based matrices are analyzed and compared to one another.

3.3.2.1.1) TM- & STBC-Based Matrices: According to (3.49) and (3.50), the channel estimate in (3.49) is used to decode the ST data matrix $\mathbf{D}(t)$ in (3.50). Therefore, the channel estimation error can be expressed by, in the matrix form,

$$\tilde{\mathbf{H}}_{TM\&STBC}(t) = \mathbf{H}_2(t) - \hat{\mathbf{H}}_{TM\&STBC}(t). \tag{3.55}$$

Without loss of generality, $\mathbf{H}_2(t)$ can be modelled as a linear combination of $\mathbf{H}_1(t)$ and the increment channel matrix $\Delta\mathbf{H}(t)$, i.e. $\mathbf{H}_2(t) = \mathbf{H}_1(t) + \Delta\mathbf{H}(t)$, then substituting this linear channel model into (3.49) and (3.55) yielding

$$\tilde{\mathbf{H}}_{TM\&STBC}(t) = \Delta\mathbf{H}(t) - \mathbf{N}_1(t). \tag{3.56}$$

From the uncorrelated assumption between the channels and noise, the $\text{MSE}_{TM\&STBC}$ of the channel estimation in (3.56) can be expressed as follows,

$$\text{MSE}_{TM\&STBC} = \text{MSE}_{quasi} + \text{E}[\|\Delta\mathbf{H}(t)\|^2], \tag{3.57}$$

where $\text{MSE}_{quasi} = \frac{\sigma^2 L_t L_r}{\alpha}$ in (3.33).

3.3.2.1.2) CM-Based Matrices: According to (3.53) and (3.54), similarly, the channel estimate in (3.53) is used to decode the data matrix $\mathbf{D}(t)$ in (3.54). Therefore, the channel estimation error can be expressed by, in the matrix form,

$$\tilde{\mathbf{H}}_{CM}(t) = \frac{1}{2}[\mathbf{H}_1(t) + \mathbf{H}_2(t)] - \hat{\mathbf{H}}_{CM}(t). \tag{3.58}$$

For the orthogonal ST block code [14] which is normalized to have $\mathrm{E}[\|\mathbf{D}(t)\|^2] = L_t$, $\mathbf{H}_2(t) = \mathbf{H}_1(t) + \Delta\mathbf{H}(t)$ is first substituted into (3.53) and (3.58), and by using the uncorrelatedness assumption between the channels and noise, the MSE of the channel estimation can be expressed as follows,

$$\text{MSE}_{CM} = \text{MSE}_{quasi} + \frac{\xi^2}{4}\mathrm{E}[\|\Delta\mathbf{H}(t)\|^2], \tag{3.59}$$

where $\xi = \sqrt{\frac{\beta}{\alpha}}$.

Notice that, in high SNR regimes where $\text{MSE}_{quasi} = 0$, if the equal power allocation, i.e. $\xi = 1$, is employed, the MSE_{CM} in (3.59) is four times less than the $\text{MSE}_{TM\&STBC}$ in (3.57). In comparison, the ratio between MSE_{CM} and $\text{MSE}_{TM\&STBC}$ can be shown as follows,

$$10\log\left(\frac{\text{MSE}_{CM}}{\text{MSE}_{TM\&STBC}}\right) = 10\log\left(\frac{1}{4}\right) = -6.02 \text{ dB}, \tag{3.60}$$

which indicates that the MSE of the channel estimation of CM-based matrices is 6.02-dB superior to that of TM- and STBC-based matrices, in the half-block fading channel model.

3.3.2.2 Data Detection Performance Analysis

In the following analysis, the closed form expression, in a matrix form for the sake of convenience, for the pair-wise probability of transmitting a codeword $\mathbf{D}$ and deciding in favor of a different codeword $\mathbf{E}$ at the maximum-likelihood receiver is provided. By using the linear channel model described in the channel estimation performance analysis, the pair-wise probability of error, given $\hat{\mathbf{H}}(t)$ and $\Delta\mathbf{H}(t)$, is given by [50]

$$P(\mathbf{D} \to \mathbf{E}|\hat{\mathbf{H}}(t), \Delta\mathbf{H}(t)) = P(\|\mathbf{Y}_1(t) - \hat{\mathbf{H}}(t)\mathbf{E}\|^2 < \|\mathbf{Y}_1(t) - \hat{\mathbf{H}}(t)\mathbf{D}\|^2|\hat{\mathbf{H}}(t), \Delta\mathbf{H}(t)). \tag{3.61}$$

3.3.2.2.1) TM- & STBC-Based Matrices: By the virtue of the AWGN assumption, substituting (3.49) and (3.50) into (3.61) to arrive at, after some algebraic manipulation,

$$P(\mathbf{D}\rightarrow\mathbf{E}|\hat{\mathbf{H}}_{TM\&STBC}(t),\Delta\mathbf{H}(t))=Q\left(\frac{\|\hat{\mathbf{H}}_{TM\&STBC}(t)(\mathbf{D}-\mathbf{E})+\Delta\mathbf{H}(t)\mathbf{D}\|^2-\|\Delta\mathbf{H}(t)\mathbf{D}\|^2}{\sqrt{\frac{2}{N}(\frac{N}{\beta}+\frac{L_t}{\alpha})\sigma^2}\|\hat{\mathbf{H}}_{TM\&STBC}(t)(\mathbf{D}-\mathbf{E})\|}\right), \tag{3.62}$$

where $Q(\cdot)$ is the Q-function defines as $Q(x)=\int_x^\infty\frac{1}{\sqrt{2\pi}}e^{-\frac{y^2}{2}}dy$.

It can be shown that a Chernoff's upper bound for (3.62) can be computed using the inequality $Q(x)\leq e^{-x^2/2}$, given by

$$\begin{aligned}&P(\mathbf{D}\rightarrow\mathbf{E}|\hat{\mathbf{H}}_{TM\&STBC}(t),\Delta\mathbf{H}(t))\\&\leq\exp\left(-\frac{(\|\hat{\mathbf{H}}_{TM\&STBC}(t)(\mathbf{D}-\mathbf{E})+\Delta\mathbf{H}(t)\mathbf{D}\|^2-\|\Delta\mathbf{H}(t)\mathbf{D}\|^2)^2}{\frac{4}{N}(\frac{N}{\beta}+\frac{L_t}{\alpha})\sigma^2\|\hat{\mathbf{H}}_{TM\&STBC}(t)(\mathbf{D}-\mathbf{E})\|^2}\right).\end{aligned} \tag{3.63}$$

By given the statistics of $\hat{\mathbf{H}}_{TM\&STBC}(t)$ and $\Delta\mathbf{H}(t)$, the averaged pair-wise error probability can be computed as follows,

$$\begin{aligned}&P(\mathbf{D}\rightarrow\mathbf{E})\\&=\int_{-\infty}^{\infty}\int_{-\infty}^{\infty}P(\mathbf{D}\rightarrow\mathbf{E}|\hat{\mathbf{H}}_{TM\&STBC}(t),\Delta\mathbf{H}(t))p_{x,y}(\hat{\mathbf{H}}_{TM\&STBC}(t),\Delta\mathbf{H}(t))dxdy,\end{aligned} \tag{3.64}$$

where $p_{x,y}(\hat{\mathbf{H}}_{TM\&STBC}(t),\Delta\mathbf{H}(t))$ is a joint pdf. of $\hat{\mathbf{H}}_{TM\&STBC}(t)$ and $\Delta\mathbf{H}(t)$.

3.3.2.2.2) CM-Based Matrices: Similarly, by the virtue of the AWGN assumption, substituting (3.53) and (3.54) into (3.61) to arrive at, after some algebraic manipulation,

$$P(\mathbf{D}\rightarrow\mathbf{E}|\hat{\mathbf{H}}_{CM}(t),\Delta\mathbf{H}(t))=Q\left(\frac{\|\hat{\mathbf{H}}_{CM_{eff}}(t)(\mathbf{D}-\mathbf{E})+\frac{\Delta\mathbf{H}(t)}{2}(\xi\mathbf{D}\mathbf{E}-\frac{\mathbf{I}}{\xi})\|^2-\|\frac{\Delta\mathbf{H}(t)}{2}(\xi\mathbf{D}\mathbf{D}-\frac{\mathbf{I}}{\xi})\|^2}{\sqrt{\frac{2}{N}(\frac{N}{\beta}+\frac{L_t}{\alpha})\sigma^2}\|\hat{\mathbf{H}}_{CM_{eff}}(t)(\mathbf{D}-\mathbf{E})+\frac{\Delta\mathbf{H}(t)}{2}(\xi\mathbf{D}\mathbf{E}-\frac{\mathbf{D}\mathbf{D}}{\xi})\|}\right), \tag{3.65}$$

where $\hat{\mathbf{H}}_{CM_{eff}}(t)=\hat{\mathbf{H}}_{TM}(t)+\frac{\Delta\mathbf{H}(t)}{2}=(\mathbf{H}_1(t)+\frac{\Delta\mathbf{H}(t)}{2})+\mathbf{N}_1(t)$.

If the equal power allocation is employed, then (3.65) can be rewritten as

$$P(\mathbf{D}\rightarrow\mathbf{E}|\hat{\mathbf{H}}_{CM}(t),\Delta\mathbf{H}(t))=Q\left(\frac{\|\hat{\mathbf{H}}_{CM_{eff}}(t)(\mathbf{D}-\mathbf{E})+\frac{\Delta\mathbf{H}(t)}{2}(\mathbf{D}\mathbf{E}-\mathbf{I})\|^2-\|\frac{\Delta\mathbf{H}(t)}{2}(\mathbf{D}\mathbf{D}-\mathbf{I})\|^2}{\sqrt{\frac{2}{N}(\frac{N}{\beta}+\frac{L_t}{\alpha})\sigma^2}\|\hat{\mathbf{H}}_{CM}(t)(\mathbf{D}-\mathbf{E})\|}\right). \tag{3.66}$$

It is straightforward to compute the Chernoff's upper bound and the averaged pair-wise error probability for (3.66) in a similar way as (3.63) and (3.64), respectively. Even though the comparison between (3.62) and (3.66) is difficult to get the closed form expression, we still provide the numerical performance comparison in section 3.5. It is worth mentioning that this analysis is valid for the fading channel model that changes in the multiple order of N, where $N\in 2^n,\ n\in\mathbb{I}$.

3.4 Optimum Block Power Allocation

In this section, the block power allocation problem is addressed in order to optimally allocate the power to the data and the pilot parts for quasi-static flat Rayleigh fading channels. It is clear that the performances of the pilot-embedded MIMO system essentially depend on the power percentages of the data and that of the pilot. In addition, the constant block power, where the power of the pilot-embedded ST symbol matrix $\mathbf{U}(t)$ is constant, is a case to be considered. The normalized block power allocated to the pilot-embedded ST symbol matrix $\mathbf{U}(t)$, which is normalized by the transmit antenna numbers L_t, can be expressed as follows,

$$P_s = \frac{\mathrm{E}\left[\|\mathbf{U}(t)\|^2\right]}{L_t} = \frac{\mathrm{E}\left[\|\mathbf{D}(t)\mathbf{A}\|^2\right]}{L_t} + \frac{\mathrm{E}\left[\|\mathbf{P}\|^2\right]}{L_t} = P_s^{'} + P_p = \beta + \alpha, \tag{3.67}$$

where the normalized block power allocated to the data part $P_s^{'} = \beta$, since $\mathrm{E}\left[\|\mathbf{D}(t)\mathbf{A}\|^2\right] = \mathrm{E}[\mathrm{tr}(\mathbf{D}(t)\mathbf{A}\mathbf{A}^T\mathbf{D}(t)^T)] = \mathrm{E}\left[\beta \mathrm{tr}(\mathbf{D}(t)\mathbf{D}(t)^T)\right] = \beta L_t$; and $P_p = \alpha$ is the normalized block power allocated to the pilot part.

The objective is to minimize the PEUB mismatch factor η in (3.43) with respect to the pilot-power factor α subject to the constraints of constant block power and acceptable MSE of the channel estimation which is a threshold that indicates the acceptable channel estimation accuracy for a reliable channel estimate. Substituting $\beta = P_s - \alpha$ into (3.43), the problem formulation is given by

$$\min_{\alpha} \ln\left(\frac{(N - L_t)\alpha + P_s L_t}{(\alpha + \sigma^2)(P_s - \alpha)}\right), \tag{3.68}$$

where MSE $\leq T$ with T being the acceptable threshold of the MSE in channel estimation. Differentiating (3.68) and equating the result to zero, the optimum solution for the pilot-power factor α^* can be expressed as follows,

$$\alpha^* = \begin{cases} \frac{P_s - \sigma^2}{2}; \ N = L_t \\ \frac{P_s L_t - \sqrt{P_s N(P_s L_t + \sigma^2(L_t - N))}}{(L_t - N)}; \ N \neq L_t, \end{cases} \tag{3.69}$$

where the MSE of the channel estimation obtained in (3.33) must satisfy the following inequality

$$\mathrm{MSE} = \frac{\sigma^2 L_t L_r}{\alpha} \leq T. \tag{3.70}$$

It is worth noticing that, in the case that $N \neq L_t$, the optimum solution for the pilot-power factor α^* in (3.69) exists if and only if signal-to-noise ratio SNR $\geq (N - L_t)$, where SNR $= \frac{P_s L_t}{\sigma^2}$. Since the case that $N = L_t = 4$ is considered in the simulations, the case that $N = L_t$ will be examined for the sake of exposition. Substituting (3.69) into (3.70), the feasible range of SNR, when the inequality in (3.70) is satisfied, and the optimum pilot-power factor α^*_{min}, when MSE $= T$, can be expressed as follows,

$$\text{SNR} \geq L_t + \frac{2L_t^2 L_r}{T}, \tag{3.71}$$

$$\alpha^*_{\text{min}} = \frac{L_t L_r P_s}{T + 2L_t L_r}. \tag{3.72}$$

Accordingly, the range of the optimum pilot-power factor α^* obtained in (3.69), when the SNR satisfies the inequality in (3.71), i.e. $L_t + \frac{2L_t^2 L_r}{T} \leq \text{SNR} < \infty$, is given by

$$\frac{L_t L_r P_s}{T + 2L_t L_r} \leq \alpha^* < \frac{P_s}{2}. \tag{3.73}$$

However, there is a case when the SNR does not satisfy the inequality in (3.71), i.e. SNR $< L_t + \frac{2L_t^2 L_r}{T}$, as a result, the MSE of the channel estimation is not reliable, i.e. MSE $>$ T, and the probability of detection error is inevitably increased. This scenario is equivalent to the low-SNR scenario, where wireless communication is not reliable. According to the range of the optimum pilot-power factor α^* obtained in (3.73), the minimum value of α^*, e.g. $\alpha^* = \frac{L_t L_r P_s}{T + 2L_t L_r}$, is used in this scenario because the PEUB mismatch factor in (3.68) is a monotonically increasing function of α, for α within this range.

In summary, the optimum pilot-power factor α^* for the case that $N = L_t$ under different SNR scenarios can be summarized as follows,

$$\alpha^* = \begin{cases} \frac{L_t L_r P_s}{T + 2L_t L_r}; \text{ SNR} < L_t + \frac{2L_t^2 L_r}{T} \\ \frac{P_s - \sigma^2}{2}; \text{ Otherwise.} \end{cases} \tag{3.74}$$

In addition, the acceptable threshold T for the MSE of the channel estimation is quite small and is determined by practice, e.g. the simulation results in Section 3.5. It is worth noticing that, under the high-SNR scenario where $\sigma^2 \to 0$ and, hence, the Chernoff's upper bound in (3.41) is tight, the pilot-power factor α approaches $P_s/2$, which is an equal power allocation also reported in [57] for the case that $N = L_t$ although where the channel estimator used is the LMMSE estimator. The reason of this convergence lies in the fact that, in high SNR regimes, both the ML and LMMSE channel estimators yield the same

effective SNR. Since the proposed scheme and [57] effectively maximize the effective SNR in order to achieve the minimum upper bound on error probability and the maximum lower bound on channel capacity, respectively, the convergence of the optimum power allocation is resulted. However, in low SNR regimes, the power allocation in both the proposed scheme and [57] are suboptimal, because the bound used in both schemes are loose and the channel estimation error is large. Nevertheless, both schemes perform fairly well in this severely unreliable scenario as shown in Section 3.5.

One may argue that a more straightforward approach to address this power allocation problem is to directly minimize the upper bound of the average probability of error in (3.41) with respect to the parameter α, since the final goal is to achieve a probability of error as small as possible. The motivation why the PEUB mismatch factor η is chosen as the objective function is to measure the performance loss of the proposed scheme when compared with a benchmark in (3.42). However, a later examination at this concern reveals that minimizing the PEUB mismatch factor η is equivalent to minimizing the Chernoff's upper bound of the average probability of error in (3.41), since other items in (3.41) such as λ_i's and σ^2 are not affected by α, and the same solution will thus be obtained.

3.5 Simulation Results

In this section, the performance of the proposed scheme is demonstrated. Without loss of generality, an orthogonal ST block code introduced in [14, 66] is examined, given as

$$\mathbf{D}(t) = \begin{pmatrix} s_1(t) & -s_2^*(t) & \frac{s_3^*(t)}{\sqrt{2}} & \frac{s_3^*(t)}{\sqrt{2}} \\ s_2(t) & s_1^*(t) & \frac{s_3^*(t)}{\sqrt{2}} & -\frac{s_3^*(t)}{\sqrt{2}} \\ \frac{s_3}{\sqrt{2}} & \frac{s_3}{\sqrt{2}} & \frac{(-s_1(t)-s_1^*(t)+s_2(t)-s_2^*(t))}{2} & \frac{(s_2(t)+s_2^*(t)+s_1(t)-s_1^*(t))}{2} \\ \frac{s_3}{\sqrt{2}} & -\frac{s_3}{\sqrt{2}} & \frac{(-s_2(t)-s_2^*(t)+s_1(t)-s_1^*(t))}{2} & -\frac{(s_1(t)+s_1^*(t)+s_2(t)-s_2^*(t))}{2} \end{pmatrix}, \quad (3.75)$$

where $s_i(t),\ i \in \{1, \ldots, 3\}$ are the ST symbols corresponding to the chosen modulation constellation, e.g. 4-PSK, 8-PSK. Three data bearer and pilot structures proposed in section 3.2 are investigated for two situations: the quasi-static and nonquasi-static flat Rayleigh fading channels. Under the nonquasi-static scenario, the performances of the pilot-embedded MIMO systems for nonquasi-static flat Rayleigh fading channel with different Doppler's shifts, representing different mobility speed of the mobile unit, are investigated. The BER and MSE of the channel estimate are used as performance measures, in comparison with the

MIMO systems employing the ideal channel coefficients for the ML receiver (see (3.30)). In the simulations, for the ideal channel coefficient case, the channel matrix $\mathbf{H}(t)$ is assumed known and thus the pilot matrix $\mathbf{P}$ is not employed, in the other words, the ST symbol matrix $\mathbf{U}(t)$ in (3.3) is now expressed as $\mathbf{U}(t) = \mathbf{D}(t)\mathbf{A}$. In addition, the performances of the pilot-embedded MIMO systems when employ the optimum power allocation scheme in (3.74), and the alternative scheme proposed in [57], are compared. In order to provide the fairness when comparing different schemes, the same transmit rate and the total transmit energy are employed by different schemes in our simulations.

For all of three data bearer and pilot structures, the setting parameters of the experiments are: the noise elements in $\mathbf{N}(t)$ in (3.1) are assumed to be independent complex Gaussian random variables with zero mean and variance $\frac{\sigma^2}{2}$ per real dimension; the normalized ST symbol block power P_s is 1 Watt/ST symbol block; the number of time slots M is 8 time slots/ST symbol block; the number of transmit antennas L_t is 4; and the data time slots $N = M - L_t$ is 4 time slots/ST symbol block. In addition, 4-PSK modulation is employed in these experiments, the acceptable threshold of the MSE of the channel estimation T is set as 0.5, and the number of LMMSE channel estimator's taps is 3.

3.5.1 The Quasi-Static Flat Rayleigh Fading Channel

In this situation, the channel coefficients of $\mathbf{H}(t)$ in (3.1) are taken from the normalized time-varying channel which is modelled as Jakes' model [51], where $fd * T = 0.08$ (fast fading) with fd being the Doppler's shift and T being the symbol period.

In Fig.3.3, the normalized power allocated to data and pilot parts of these two optimum power allocation strategies is illustrated. It is worth noticing that these two power allocation strategies converge to 0.5 Watt in high SNR regimes as explained in section 3.4.

In Fig.3.4, we plot MSEs of the channel estimation of the pilot-embedded MIMO system with applying the optimum and the alternative optimum power allocation strategies, when 1 and 2-received antennas are employed. Notice that the MSEs of the optimum power allocation scheme is slightly higher than that of the alternative optimum power allocation scheme in low SNR regimes. In addition, the MSEs of the channels estimation of the 2-received antenna scenario are larger than that of the 1-received antenna scenario as explained by referring to (3.33), and three types of data-bearer and pilot matrices yield the

same MSE which coincides with the trace of the CRLB in (3.36). Notice that, the LMMSE channel estimator outperforms the ML channel estimator, where the MSE of the channel estimation is much lower in the LMMSE channel estimator. In fact, the LMMSE channel estimator is a Bayesian estimator in which the prior knowledge on the statistics of channels is exploited; therefore, its performance is much better than the ML channel estimator, which is a deterministic estimator, and that of CRLB. Furthermore, the LMMSE channel estimator tradeoffs the bias for variance, hence, the overall MSE is reduced [61]. The CRLB for Bayesian estimators including the LMMSE channel estimator can be found in [58, 61].

In Fig.3.5, we plot BERs of the pilot-embedded MIMO system with applying the optimum power allocation strategy, in comparison with the ideal-channel MIMO system, when 1 and 2-received antennas are employed. In the ideal channel case, the channel coefficients are assumed known, thus it serves as a performance bound. Notice that, at BER = 10^{-4}, the SNR differences between the ideal-channel and the ML channel estimator are about 2.3 dB for both the 1 and 2-received antenna schemes, whereas the LMMSE channel estimation achieves the ideal-channel error probability for the 1-received antenna scheme, and the SNR difference between the ideal-channel and the LMMSE channel estimator are about 0.5 dB for the 2-received antenna scheme. In addition, the SNR differences between the ML and LMMSE channel estimators are about 1.8 dB. It is worth noticing that the LMMSE channel estimator performs better than the ML channel estimator because of the higher accurate channel estimate, as shown in Fig.3.4.

In Fig.3.6, the BERs are plotted in comparison between the proposed and alternative optimum power allocation strategies [57], both compared with the ideal-channel MIMO system, when 1 and 2-received antennas are employed. For the sake of clarity, the CM-based matrices are used as the representative of all three structures that behave similarly in the experimental results. Obviously, say at BER = 10^{-4}, both optimum power allocation strategies are quite close resulting from the very small difference in the power allocated to the data and pilot parts in both strategies, as shown in Fig.3.3.

3.5.2 The Nonquasi-Static Flat Rayleigh Fading Channel

In this situation, the situation where the channel coefficient matrix $\mathbf{H}(t)$ is not kept constant over a ST symbol block is considered. An example where the channel coefficient

matrix symmetrically changes twice within one ST symbol block as described in section 3.3.2 is examined. Two cases, where 1 and 2-received antennas are employed for the pilot-embedded optimum-power-allocated MIMO system, are examined in order to illustrate the effect of the time variance in the ST symbol block versus the number of received antennas.

3.5.2.1 1-Received Antenna Scheme

In Fig.3.7, the graph of MSEs of the channel estimation of the pilot-embedded MIMO system when $fd * T$ are 0.0021 (slow fading), 0.0165, 0.0412, and 0.0741 (fast fading) is shown. Notice that the CM-based matrices provides the lower MSE than the TM- and STBC-based matrices. When Doppler's shifts are fairly large, in high SNR regimes, the SNR difference between the CM- and the TM- or STBC-based matrices ML channel estimators are approximately 6.02 dB, as remarked in the figure. This result strongly supports the derivation in section 3.3.2.1 as well.

In Fig.3.8, the graph of BERs of the pilot-embedded MIMO system when $fd * T$ are 0.0021 (slow fading), 0.0165, 0.0412, and 0.0741 (fast fading) is shown. Notice that, when Doppler's shifts are small, e.g. $fd * T = 0.0021$, the probability of error detection of three kinds of data bearer and pilot structures are quite the same; however, when Doppler's shifts are getting larger, the CM-based structure is much better than the TM- and STBC-based structures, where the error floors of the CM-based structure are much lower than the TM- and STBC-based structures. It is worth mentioning that, in high SNR regimes, the SNR difference between the CM-based matrices and the TM- or STBC-based matrices ML channel estimators are approximately 6.02 dB, as remarked in the figure. This result supports the derivation in section 3.3.2.2 as well. Since the nonquasi-static flat Rayleigh fading channel is the severe situation, there exists error floors that increase significantly as the Doppler's shift increases.

3.5.2.2 2-Received Antenna Scheme

In Fig.3.9, the graph of MSEs of the channel estimation of the pilot-embedded MIMO system when $fd * T$ are 0.0021 (slow fading), 0.0412, 0.0741, and 0.1235 (fast fading) is shown. Similarly to the 1-received antenna scheme, the CM-based matrices provides the

much lower MSE than the TM- and STBC-based matrices. In addition, the 6.02-dB SNR difference is also observed when Doppler's shifts are fairly large, in high SNR regimes.

In Fig.3.10, the graph of BERs of the pilot-embedded MIMO system when $fd * T$ are 0.0021 (slow fading), 0.0412, 0.0741, and 0.1235 (fast fading) is shown. Similarly to the 1-received antenna scheme, the CM-based structure is much better than the TM- and STBC-based structures, and, in high SNR regimes, the SNR difference between the CM- and the TM- or STBC-based matrices ML channel estimators are approximately 6.02 dB, as remarked in the figure.

It is worth mentioning that the CM-based structure yields better BER performances than that of the TM- and STBC-based structures, especially under the high Doppler's shift scenarios. The reason why the CM-based structure performs better than the TM-based and STBC-based structures is that it takes both of the channel coefficient matrices $\mathbf{H}_1(t)$ and $\mathbf{H}_2(t)$ into account (see (3.53)), whereas the other two structures exploit either some parts of $\mathbf{H}_1(t)$ or $\mathbf{H}_2(t)$ based on their structures (see (3.49)). In this situation, there also exists the inevitable error floors that increase significantly as the Doppler's shift increases. These error floors result from the channel mismatch introduced as the bias in the channel estimate, thus result in a poor detection performance especially under the high Doppler's shift scenarios. Furthermore, the LMMSE channel estimator performs better than the ML channel estimator in low SNR regimes, in which the AWGN is the major factor that causes the detection error; however, in high SNR regimes, the channel mismatch plays a major role in causing the detection error resulting in the comparable error floors for the LMMSE and ML channel estimators. Interestingly, increasing the number of receive antennas yields an additional benefit to the ML receiver in term of the robustness to the Doppler's shift, where the 2-received antenna scenario is less sensitive to the Doppler's shift than the 1-received antenna scenario.

3.6 Concluding Remark

In this chapter, the data-bearing approach for pilot-embedding frameworks was proposed for joint data detection and channel estimation in ST coded MIMO systems. The main contributions of this chapter are as follows.

- The advantages of the data-bearing approach are that it is the generalized form for

pilot-embedded channel estimation and data detection in ST coded MIMO systems, in which the classical channel estimation method, e.g. PSAM, is subsumed; the low computational complexity and the efficient ML and LMMSE channel estimators are achieved; and it is capable of better acquiring the channel state information in fast-fading channels.

- For the quasi-static flat Rayleigh fading channels, the error probability and the channel estimation performance of three data-bearer and pilot structures, i.e. the TM-, STBC-, and CM-based data-bearer and pilot matrices, are quite similar, where the optimum-power-allocated schemes based on the minimum upper bound on error probability and the maximum lower bound on channel capacity optimizations yield the close results. This result claims that the proposed scheme is one of the implementable scheme that achieves the maximum lower bound on channel capacity derived in [57], in high SNR regimes. In addition, the SNR differences between the optimum-power-allocated schemes and the ideal-channel schemes are about 2.3 dB when employing the unconstrained ML channel estimator and 0.5 dB for the LMMSE channel estimator.

- For the case of nonquasi-static flat Rayleigh fading channels, the CM-based structure provide superior detection and channel estimation performances over the TM- and STBC-based structures. For instance, the 6.02 dB SNR difference is observed, as well as the error floors of the former are much smaller than that of the other two, under fairly high Doppler's shift scenarios, in high SNR regimes.

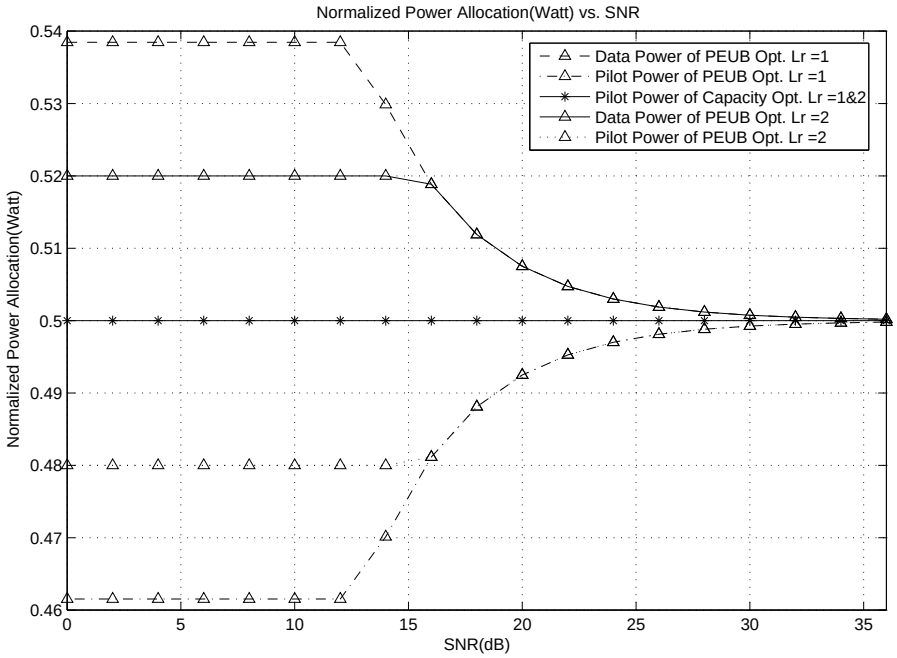

Figure 3.3: The graph of the normalized power allocated to the data and pilot parts when applying the proposed and alternative optimum power allocation strategies.

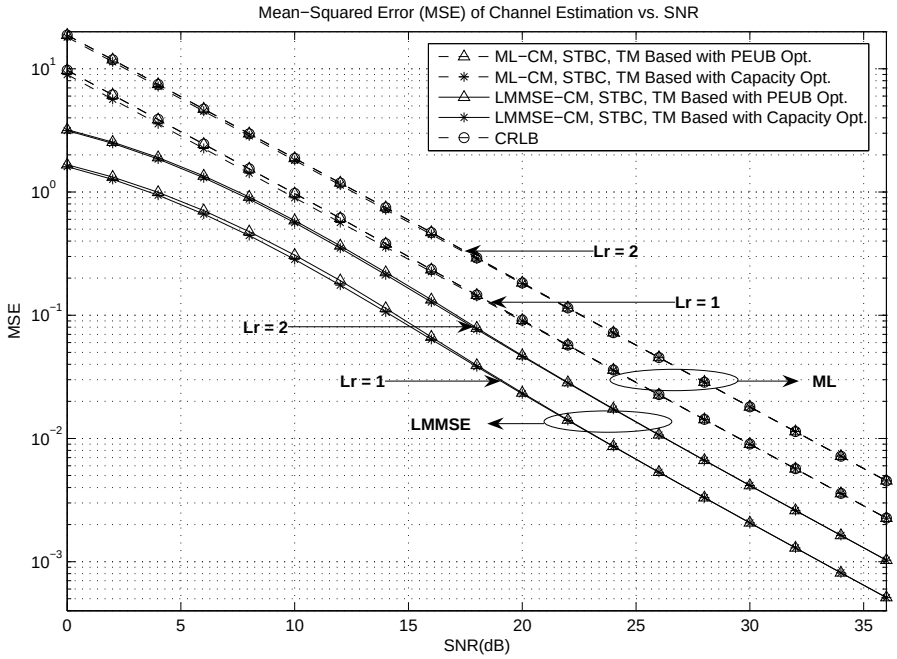

Figure 3.4: The graph of MSEs of the ML and LMMSE channel estimations where the proposed and alternative optimum power allocation strategies are compared in the quasi-static flat Rayleigh fading channel.

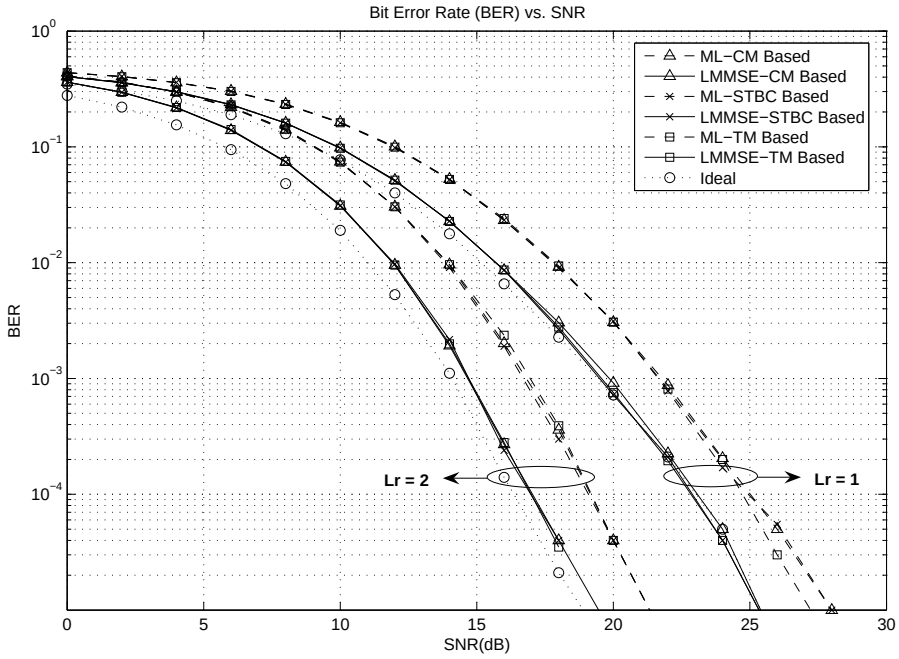

Figure 3.5: The graph of BERs of the pilot-embedded optimum-power-allocated MIMO system in the quasi-static flat Rayleigh fading channel.

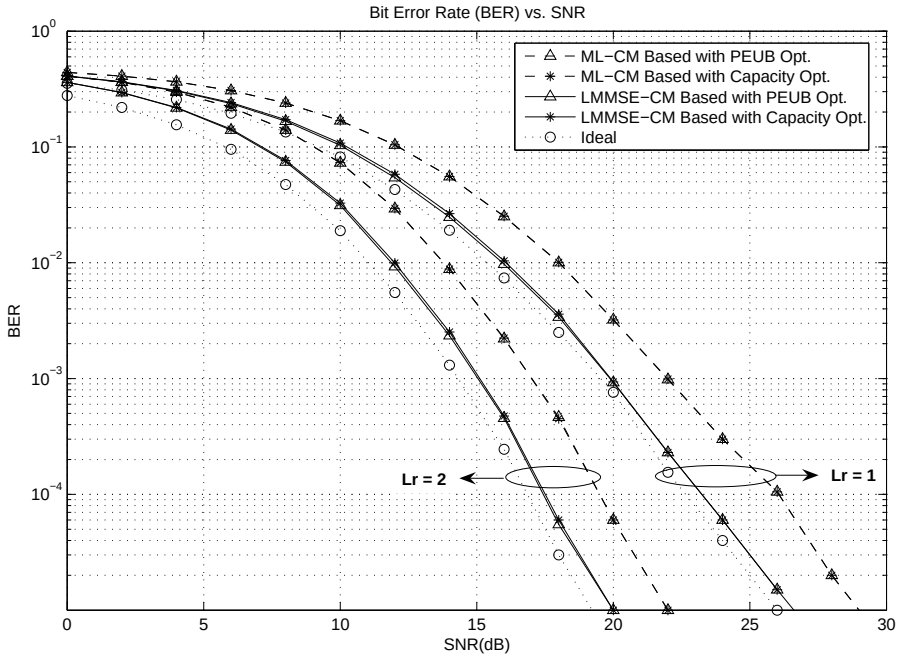

Figure 3.6: The graph of BERs where the proposed and alternative optimum power allocation strategies are compared in the quasi-static flat Rayleigh fading channel.

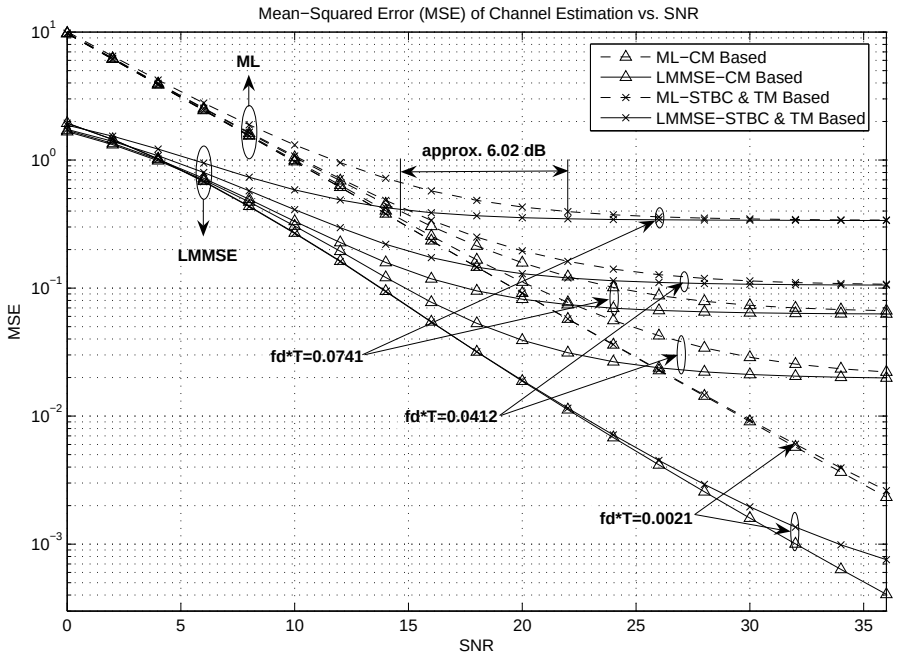

Figure 3.7: The graph of MSEs of the pilot-embedded optimum-power-allocated ML and LMMSE channel estimations when $L_r = 1$ in the nonquasi-static flat Rayleigh fading channel.

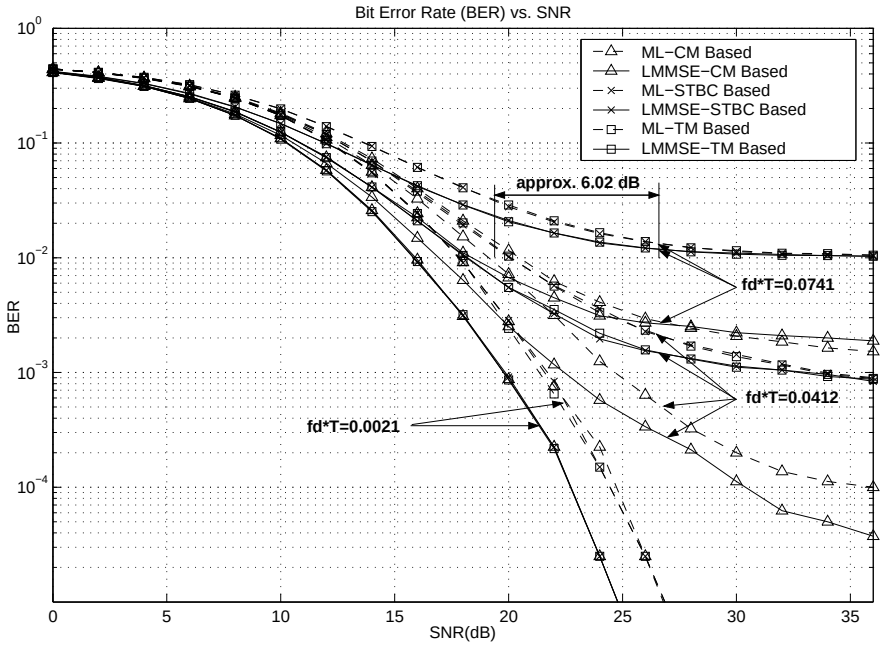

Figure 3.8: The graph of BERs of the pilot-embedded optimum-power-allocated MIMO system when $L_r = 1$ in the nonquasi-static flat Rayleigh fading channel.

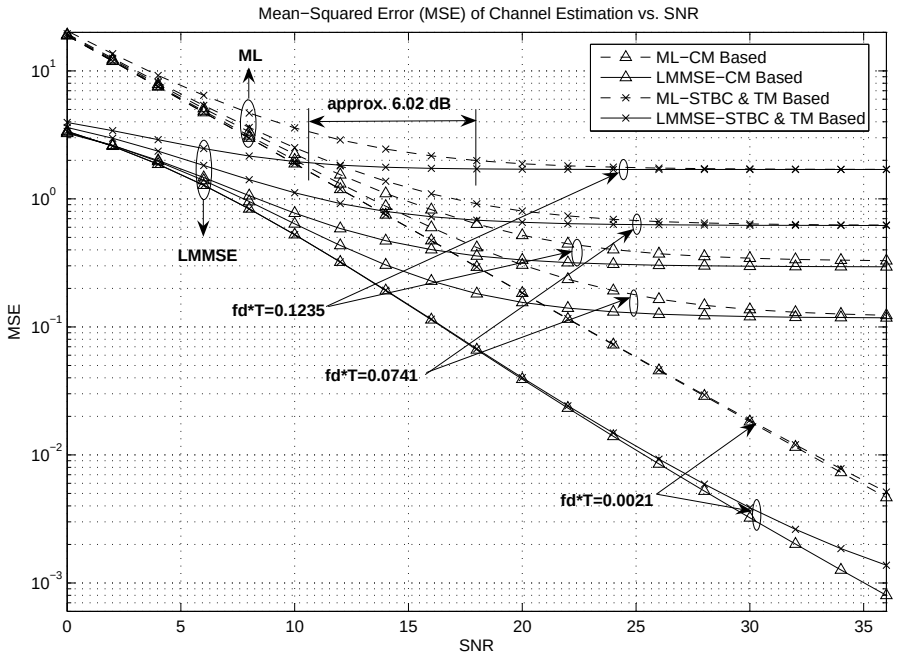

Figure 3.9: The graph of MSEs of the pilot-embedded optimum-power-allocated ML and LMMSE channel estimations when $L_r = 2$ in the nonquasi-static flat Rayleigh fading channel.

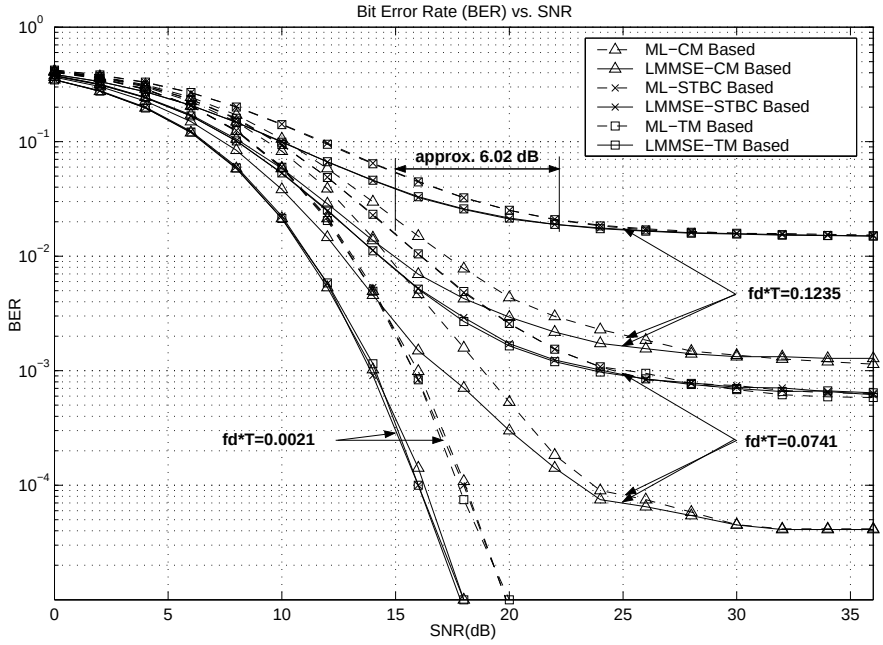

Figure 3.10: The graph of BERs of the pilot-embedded optimum-power-allocated MIMO system when $L_r = 2$ in the nonquasi-static flat Rayleigh fading channel.

CHAPTER IV

ADAPTIVE CHANNEL ESTIMATION USING PILOT-EMBEDDED DATA-BEARING APPROACH FOR SPACE-FREQUENCY CODED MIMO-OFDM SYSTEMS

In chapter III, the data-bearing approach for pilot-embedding frameworks was developed for acquiring the CSI of the frequency-nonselective (or flat) fading channels in ST coded MIMO systems. Since only a direct line-of-sight-path signal exists in such channels, a number of channel coefficients to be estimated is essentially equal to a multiplication of L_t-transmit and L_r-receive antennas, i.e. $L_t L_r$. However, in practical applications, the frequency-selective (or multipath) fading channel models are more realistic and more general than the flat fading channel models. Furthermore, the multipath fading channels are challenger than that of the flat fading channels in terms of the complication of an underlying problem, where a large number of channel coefficients are to be estimated, and the corresponding computational complexity. It is well known that the OFDM technique is one of the multicarrier modulation technique that is effectively able to combat the multipath fading channels. Recently, the OFDM technique has been introduced to MIMO systems, namely the MIMO-OFDM systems. One critical issue for such systems employing coherent receivers is channel estimation. Since the multipath delay profile of channels are arbitrary in the MIMO-OFDM systems, an effective channel estimator is needed to estimate these channels. In this chapter, the basic background about channel estimation techniques for MIMO-OFDM systems is reviewed. Further, a generalization of the pilot-embedded data-bearing approach for joint channel estimation and data detection, in which PEDB-LS channel estimation and PEDB-ML data detection are employed, is first developed. Then an LS FFT-based channel estimator by employing the concept of FFT-based channel estimation to improve the PEDB-LS channel estimation via choosing certain significant taps in constructing a channel frequency response is proposed. The effects of model mismatch error inherent in the proposed LS FFT-based channel estimator when considering non-integer multipath

delay profiles, and its performance analysis are investigated. Under the framework of pilot embedding, an adaptive LS FFT-based channel estimator, that employs the optimum number of taps such that an average total energy of the channels dissipating in each tap is completely captured in order to compensate the model mismatch error as well as minimize the corresponding noise effect to improve the performance of the LS FFT-based channel estimator, is further proposed. Simulation results reveal that the adaptive LS FFT-based channel estimator is superior to the LS FFT-based and PEDB-LS channel estimators under quasi-static channels or low Doppler's shift regimes.

4.1 Introduction

High speed data transmission services have been highly demanded in future wireless communications [67]. One promising transmission scheme to satisfy this growing demand is the use of the OFDM technique [68], in which frequency-selective fading channels are transformed into a set of parallel flat fading subchannels. Hence, such communication techniques, e.g. channel estimation and equalization, designed for flat fading channels can be directly applied to frequency-selective fading channels through the OFDM communication scheme. In addition, since the OFDM communication scheme is a block transmission scheme, its symbol duration is longer. When the symbol duration is longer than the delay spread of channels, ISI is therefore eliminated. Nowadays, the OFDM communication scheme has been employed in various high speed wireless transmission standards such as broadband wireless LANs (IEEE 802.11a) [69], digital audio broadcasting (DAB) [70], and digital video broadcasting (DVB-T) [71]. Recently, MIMO-OFDM systems have been proposed for increasing communication capacity as well as reliability of the wireless communication systems by exploiting both the spatial and frequency diversities [68, 72]. Further the space-frequency (SF) coding for MIMO-OFDM systems have been developed for achieving such diversities in order to enhance the reception performance for high data-rate wireless communications. However, those aforementioned schemes normally need to assume an accurate CSI for coherently decoding the transmitted data, e.g. the ML decoder. Therefore, channel estimation is of critical interest for MIMO-OFDM systems.

Typically a pilot or training signal, a known signal transmitted from the transmitter to the receiver, is highly desirable to obtain an accurate channel estimation. In [73], the

optimal criteria of designing the training sequence in MIMO-OFDM systems were proposed. There are two main types of pilot-aided channel estimation techniques for MIMO systems: the PSAM technique [56, 57], and the pilot-embedding technique [59, 60]. Recently, the pilot-embedded data-bearing approach for joint channel estimation and data detection has been proposed by exploiting the null-space property and the orthogonality property of the data bearer and pilot matrices [74].

Various channel estimation schemes have been recently proposed for MIMO-OFDM systems [73, 75--78]. In [75], the LMMSE channel estimator was proposed, in which SVD decomposition is used to simplify the ordinary LMMSE channel estimator. Despite the highly accurate channel estimate of this scheme, it requires intensive computational complexity and the knowledge of the underlying channel correlation. In [76], the FFT-based channel estimation using a certain number of significant taps for estimating the channel impulse response in a temporal domain was proposed. Despite the efficient computational complexity of this scheme, it could suffer from an error floor caused by a non-integer multipath delay spread, relative to the system sampling period, in the wireless channels, known as a *model mismatch error*. The enhancement and simplification of [76] were proposed in [77, 78], respectively.

The model mismatch error or, in the other word, the leakage effect was first mentioned in SISO-OFDM systems employing the FFT-based channel estimation [79--81]. Without the knowledge of channel correlation information, there are two ways to reduce the leakage effect: 1) by changing the exponential basis functions to the polynomial basis functions in the FFT-based channel estimation [82--84] for SISO systems and [85] for MIMO systems, and 2) by employing a proper number of taps to construct a channel frequency response in the FFT-based channel estimation [76]. In the former approach, the thorough investigation of the polynomial-based channel estimation for the MIMO systems has been conducted in [85]. Although this approach provides better performance than the FFT-based approach [81] under the non-integer multipath delay profiles, its performance is worse under the integer multipath delay profiles. Furthermore, this approach impose higher computational complexity than that of the FFT-based approach, and a general rule of designing the optimum window length as well as the optimum order of the polynomial is not fully discovered. Given the efficient implementation and reliability constraints, the FFT-based approach is still attractive.

However, the optimal guideline about how to choose the number of taps remains unsolved. The challenge now is to find the optimal criteria for obtaining the optimum number of taps given that the knowledge of channel correlation information or Doppler's shift are unavailable.

The goal of this chapter is to develop an efficient channel estimation scheme when employing pilot-embedding idea in MIMO-OFDM systems. The main contributions of this chapter are as follows.

- A generalization of the pilot-embedded data-bearing approach for joint channel estimation and data detection for MIMO-OFDM systems, in which the PEDB-LS channel estimation and PEDB-ML data detection are employed, respectively, is developed. Furthermore, the LS FFT-based channel estimation is proposed to improve the performance of the PEDB-LS channel estimate by employing the FFT-based approach concept.

- The model mismatch error of the LS FFT-based channel estimator is investigated, and this problem is solved by proposing an adaptive LS FFT-based channel estimation approach that employs the optimum number of taps such that the average total energy of the channels dissipating in each tap is completely captured in order to compensate the model mismatch error as well as minimize the corresponding noise effect.

The organization of this chapter is as follows. In section 4.2, the wireless channel and system models used in this chapter are introduced. In section 4.3, the generalization of the pilot-embedded data-bearing approach for joint channel estimation and data detection, including the PEDB-LS channel estimation and PEDB-ML data detection, is proposed. Under this pilot-embedding framework, in section 4.4, the LS FFT-based channel estimator is proposed, and the performance analysis for the PEDB-LS and LS FFT-based channel estimation approaches is also investigated. In section 4.5, the adaptive LS FFT-based channel estimation for improving the performance of the LS FFT-based channel estimation is proposed. In section 4.6, the performance of the proposed schemes are examined via simulations, and the conclusion is given in section 4.7.

4.2 Wireless Channel and System Models

In this section, the wireless channel and system models used in this chapter are now described. A $K-$tone SF-coded OFDM system with L_r receive and L_t transmit antennas is considered.

4.2.1 Wireless Channel Model

The complex baseband impulse response of the wireless channel between the a^{th} $(a = 1, \ldots, L_r)$ receive antenna and the b^{th} $(b = 1, \ldots, L_t)$ transmit antenna can be described by [86]

$$h_{ab}(t, \tau) = \sum_l \gamma_l(t)\delta(\tau - D_l), \tag{4.1}$$

where D_l is the delay of the l^{th} path and $\gamma_l(t)$ represents the corresponding complex amplitude. $\gamma_l(t)$'s are modelled as wide-sense stationary (WSS), narrowband complex Gaussian processes, which are independent for different paths, and $\mathrm{E}[|\gamma_l(t)|^2] = \sigma_l^2$ with σ_l^2 being the average power of the l^{th} path. Throughout this chapter, all the signals transmitted from different transmit antennas and received at different receive antennas are assumed undergone independent fading, and the channel average power is normalized to have $\sum_l \sigma_l^2 = 1$. For OFDM systems with tolerable leakage, the normalized frequency response of the OFDM systems at the k^{th} $(k = 0, \ldots, K-1)$ subcarrier between the a^{th} receiver and the b^{th} transmitter can be described by [76]

$$H_{ab}(m, n, k) = \sum_{l=0}^{L-1} h_{ab}(m, n, l) F_K^{k\tau_l}, \tag{4.2}$$

where $h_{ab}(m, n, l) \triangleq h_{ab}(m, nT_f, \tau_l T_s)$, $F_K = \exp(-j2\pi/K)$, $T_s = 1/(K\Delta)f$, with Δf being the tone spacing, is the sample interval of the system, T_f is the OFDM block length, and m denotes the index of a group of N-OFDM blocks described next. L is the number of nonzero paths, which represents the order of frequency diversity of the channel, and the integer τ_l, $l = 0, \ldots, L-1$ is the l^{th} path's delay sampled at rate T_s, e.g. $D_l = \tau_l T_s$. Furthermore, the average power of $h_{ab}(m, n, l)$ and the value of $L(\leq K)$ depend on the delay profile and the dispersion of the wireless channels. For simplicity, the time index n is omitted in all notations in the next text.

4.2.2 System Model

At the transmitter side, the data stream is split into L_t substreams, and, in each substream, a group of data is chosen to match the corresponding baseband M-phase-shift keyed (MPSK) constellation symbol. These MPSK-data symbols are then coded by the SF block code, e.g. [72], and grouped to construct the $L_t \times KN$ SF-coded data matrix $\mathbf{S}(m)$, where N denotes the number of OFDM blocks (each OFDM block has K tones) to be regarded as one SF-coded data block, and m denotes the N-OFDM-block index. Before modulating this SF-coded data block by the OFDM modulator, the SF-coded data matrix $\mathbf{S}(m)$ is embedded by the pilot signal using the pilot-embedded data-bearing approach proposed later, so that the SF-coded symbol matrix with size $L_t \times KM$, where M denotes the number of OFDM blocks included in one SF-coded symbol block, is defined. Notice that $M > N$ since redundancy is introduced after embedding the pilot signal for acquiring the CSI. Each pilot-embedded OFDM block is then modulated and simultaneously transmitted across L_t transmit antennas. In order to eliminate ISI, a cyclic prefix in which the length of cyclic extension must be no smaller than τ_{L-1} is employed. In this chapter, two types of fading channels: quasi-static and nonquasi-static frequency-selective Rayleigh fading channels are considered. The former is the scenario that the channel remains constant over the SF-coded symbol block but changes in a block-by-block way, whereas in the latter the channel changes within the SF-coded symbol block. At the receiver side, the received signal is sampled at rate t_s and demodulated by the OFDM demodulator. By assuming tolerable power leakage and perfect time/frequency synchronization, the received signal of the m^{th} SF-coded symbol block can be described by

$$\mathbf{Y}(m) = \mathbf{H}(m)\mathbf{U}(m) + \mathbf{N}(m), \tag{4.3}$$

where $\mathbf{Y}(m)$ is a $L_r \times KM$ matrix; $\mathbf{H}(m)$ is the $L_r \times KL_t$ channel matrix in which the a^{th} row of $\mathbf{H}(m)$ is $[\mathbf{H}_{a1}(m), \ldots, \mathbf{H}_{aL_t}(m)]$ where $\mathbf{H}_{ab}(m) = [H_{ab}(m,0), \ldots, H_{ab}(m,K-1)]$; $\mathbf{N}(m)$ is the $L_r \times KM$ AWGN matrix with zero mean and variance $\frac{\sigma^2}{2}\mathbf{I}_{(L_rKM \times L_rKM)}$ per real dimension; and $\mathbf{U}(m)$ is the $KL_t \times KM$ equivalent SF-coded symbol matrix. Throughout this chapter, the channels and noise, and channels from different paths are assumed mutually uncorrelated.

4.3 Pilot-Embedded Data-Bearing Approach

In this section, the main ideas of the pilot-embedded data-bearing approach for joint channel estimation and data detection is first presented. The basic LS channel estimation and the ML data detection are then briefly introduced.

4.3.1 Pilot-Embedded Data-Bearing Approach

In the pilot-embedded data-bearing approach for joint channel estimation and data detection, the equivalent SF-coded symbol matrix $\mathbf{U}(m)$ can be described as follows,

$$\mathbf{U}(m) = \mathbf{D}(m)\mathbf{A} + \mathbf{P}, \tag{4.4}$$

where $\mathbf{D}(m)$ denotes the $KL_t \times KN$ equivalent SF-coded data matrix constructed from the matrix $\mathbf{S}(m)$ using the $K \times K$ matrix-diagonalized operator diag$\{\cdot\}$, where the $((b-1)K+1)^{th}$ row to the $(bK)^{th}$ row of $\mathbf{D}(m)$ are $[\text{diag}\{[\mathbf{S}(m)]_{b,1:K}\}, \ldots, \text{diag}\{[\mathbf{S}(m)]_{b,(N-1)K+1:NK}\}]$ with $x : y$ denotes the column/row index interval ranging x to y; $\mathbf{A}$ is the $KN \times KM$ data bearer matrix; and $\mathbf{P}$ is the $KL_t \times KM$ pilot matrix. Notice that the K diagonal elements of a $(b, c)^{th}$ submatrix, $c = 1, \ldots, M$, represented in $\mathbf{U}(m)$ by the $((b-1)K+1)^{th}$ row to the $(bK)^{th}$ row and the $((c-1)K+1)^{th}$ column to the $(cK)^{th}$ column are the c^{th} transmitted SF-coded OFDM block at the b^{th} transmitter in the m^{th} SF-coded symbol block-group. In addition, the energy constraint $\mathrm{E}[\|\mathbf{D}(m)\|^2] = KL_t$ is maintained for the equivalent SF-coded data matrix. Substituting (4.4) into (4.3), we have the received signal matrix as

$$\mathbf{Y}(m) = \mathbf{H}(m)(\mathbf{D}(m)\mathbf{A} + \mathbf{P}) + \mathbf{N}(m). \tag{4.5}$$

Now, by the pilot-embedded data-bearing approach, the data bearer matrix $\mathbf{A}$ and the pilot matrix $\mathbf{P}$ are required to satisfy the following properties:

$$\mathbf{A}\mathbf{P}^T = \mathbf{0}_{(KN \times KL_t)}, \ \mathbf{P}\mathbf{P}^T = \alpha\mathbf{I}_{(KL_t \times KL_t)}, \tag{4.6}$$

$$\mathbf{P}\mathbf{A}^T = \mathbf{0}_{(KL_t \times KN)}, \text{ and } \mathbf{A}\mathbf{A}^T = \beta\mathbf{I}_{(KN \times KN)}, \tag{4.7}$$

where β is the real-valued data-power factor, α is the real-valued pilot-power factor. The similar property $\mathbf{P}\mathbf{P}^T = \alpha\mathbf{I}$ in (4.6) is also suggested in [73] that they are the optimal criteria for the optimal training design for MIMO-OFDM systems. There are several possible

structures of data-bearing and pilot matrices, in which the elements of these matrices are real numbers, that satisfy the properties (4.6) and (4.7). There is particularly of interest in the case of the CM-based matrices, since it provides the superior performance among the three structures studied in chapter III, see also [74].

The CM-Based matrices are now described. The structures of these matrices are given as

$$\mathbf{A} = \sqrt{\beta}\text{WH}[1:N]_{(N\times M)} \otimes \mathbf{I}_{(K\times K)}, M = N + L_t,$$
$$\mathbf{P} = \sqrt{\alpha}\text{WH}[N+1:M]_{(L_t\times M)} \otimes \mathbf{I}_{(K\times K)}, \tag{4.8}$$

where WH$[x:y]$ denotes a sub-matrix created by splitting the $M \times M$ normalized Walse-Hadamard matrix [64] starting from x^{th}-row to y^{th}-row and $\otimes$ denotes the Kronecker product. The disadvantage of this structure is the limitation of dimensionality of Walse-Hadamard matrix, which has a dimension proportionally to $2^n,\ n \in \mathbb{I}$. This structure provides an instructive example of the proposed general idea in (4.4) for pilot-embedding.

Notice that, in (4.8), the proposed scheme is a block-training scheme in which L_t OFDM blocks are used for estimating the CSI. As suggested in [75, 76], when using only one OFDM block for training in the MIMO-OFDM systems, the LS channel estimator for $\mathbf{H}_{ab}(m)$ exists only if $K \geq L_t L$. In general, in the case that $K < L_t L$ and $L \leq K$, the use of L_t OFDM blocks for training can guarantee the existence of the LS channel estimation and other better channel estimators, such as the LMMSE channel estimator [75].

4.3.2 Pilot-Embedded Data-Bearing Least Square Channel Estimation

The pilot part is first extracted from the received signal matrix $\mathbf{Y}(m)$. By using the null-space and orthogonality properties in (4.6), respectively, the extraction of the pilot part can be accomplished by simply post multiplying $\mathbf{Y}(m)$ in (4.5) by $\mathbf{P}^T$, and then dividing by α, to arrive at

$$\frac{\mathbf{Y}(m)\mathbf{P}^T}{\alpha} = \mathbf{H}(m) + \frac{\mathbf{N}(m)\mathbf{P}^T}{\alpha}. \tag{4.9}$$

Let $\mathbf{Y}_1(m) = \frac{\mathbf{Y}(m)\mathbf{P}^T}{\alpha}$ and $\mathbf{N}_1(m) = \frac{\mathbf{N}(m)\mathbf{P}^T}{\alpha}$, we have

$$\mathbf{Y}_1(m) = \mathbf{H}(m) + \mathbf{N}_1(m). \tag{4.10}$$

The PEDB-LS channel estimator can be obtained by minimizing the following mean-squared-error objective function,

$$\hat{\mathbf{H}}_{LS}(m) = \min_{\mathbf{H}(m)} \mathrm{E}\left[\|\mathbf{Y}_1(m) - \mathbf{H}(m)\|^2\right]. \tag{4.11}$$

It is straightforward to show that

$$\hat{\mathbf{H}}_{LS}(m) = \mathbf{Y}_1(m) = \frac{\mathbf{Y}(m)\mathbf{P}^T}{\alpha}. \tag{4.12}$$

The PEDB-LS channel estimate in (4.12) completely captures the whole channel frequency response contaminated by AWGN. Later it can be shown that it does not benefit by using all the PEDB-LS channel estimate taps in decoding the SF-coded transmitted signal since some taps are dominated by noise, where the noise power is significantly larger than the channel energy contained. More specifically, if the significant taps for estimating the channel frequency response are properly chosen, and the rest less significant taps are therefore discarded, the accuracy of the channel estimate could be enhanced because the noise effects contained in these less significant taps are completely avoided. The problem of how to choose the optimum number of taps will be thoroughly investigated in section 4.5.

4.3.3 Pilot-Embedded Data-Bearing Maximum Likelihood Data Detection

The procedure of PEDB-ML data detection is now explored. First, the data part is extracted from the received signal matrix $\mathbf{Y}(m)$. Using the null-space and orthogonality properties in (4.7), respectively, the extraction of the data part can be accomplished by simply post multiplying $\mathbf{Y}(m)$ in (4.5) by $\mathbf{A}^T$, and then dividing by β,

$$\frac{\mathbf{Y}(m)\mathbf{A}^T}{\beta} = \mathbf{H}(m)\mathbf{D}(m) + \frac{\mathbf{N}(m)\mathbf{A}^T}{\beta}. \tag{4.13}$$

Let $\mathbf{Y}_2(m) = \frac{\mathbf{Y}(m)\mathbf{A}^T}{\beta}$ and $\mathbf{N}_2(m) = \frac{\mathbf{N}(m)\mathbf{A}^T}{\beta}$, it can be shown that

$$\mathbf{Y}_2(m) = \mathbf{H}(m)\mathbf{D}(m) + \mathbf{N}_2(m). \tag{4.14}$$

From the orthogonality of $\mathbf{A}$ in (4.7), we note that $\sum_{j'=1}^{KM} |A_{i',j'}|^2 = \beta,\ \forall i'$. Therefore, the data-bearer-projected noise $\mathbf{N}_2(m)$ is AWGN with zero-mean and variance $\frac{\sigma^2}{2\beta}\mathbf{I}_{(KL_rN \times KL_rN)}$ per real dimension. Due to the i.i.d white Gaussian distribution of $\mathbf{N}_2(m)$, the PEDB-ML receiver jointly decides the codewords for the d^{th} OFDM block in the m^{th} SF-coded data

block by solving the following minimization problem,

$$\hat{\mathbf{D}}_{i,j}(m) = \min_{\mathbf{D}_{i,j}} \|\mathbf{Y}_{2_{s,j}}(m) - \hat{\mathbf{H}}_{s,i}(m)\mathbf{D}_{i,j}(m)\|^2,$$
$$i = 1 : KL_t,\ j = (d-1)K + 1 : dK,\ s = 1 : L_r, \text{ and } d = 1, \ldots, N, \qquad (4.15)$$

where $\hat{\mathbf{H}}(m)$ is the estimated channel matrix, e.g. $\hat{\mathbf{H}}(m) = \hat{\mathbf{H}}_{LS}(m)$. The codeword transmitted from the b^{th} transmitter is represented by $\hat{\mathbf{D}}_{i_b,j}(m)$, with $i_b = (b-1)K+1 : bK$. Later in simulations, by using the specific property of the SF block code based on Alamouti's structure, a simplified decoding approach can be applied to implement the above PEDB-ML receiver.

4.4 The Least Square FFT-Based Channel Estimation and Performance Analysis

As mentioned earlier, the PEDB-LS channel estimate contains the channel frequency response that is contaminated by AWGN. By properly choosing the significant taps and discarding the rest less significant taps, these corresponding significant taps can be used to reconstruct the whole channel frequency response in which the excessive noise contained in the less significant taps are completely cancelled. Hence, the enhanced channel estimate can be expected. In this section, the performance of the PEDB-LS channel estimator in (4.12) is improved by employing the basic concepts of the FFT-based approach proposed in [76]. First, following the description in section 4.3, the LS FFT-based channel estimator is proposed, and an inherent problem is pointed out. Then the channel estimation performances of the PEDB-LS and LS FFT-based channel estimators are analyzed.

4.4.1 Least Square FFT-Based Channel Estimation Approach

As suggested in [76], the FFT-based channel estimation approach first calculates the temporal LS channel estimate by using L significant taps. The resulting temporal LS channel estimate is then FFT transformed to obtain the K-subcarrier channel frequency response. The simplified approach was suggested in [76] by choosing P significant taps, in the sense that P's largest $\sum_{b=1}^{L_t} |\hat{H}_{LS_{ab}}(m,k)|^2$, among $k = 0, \ldots, K-1$, is selected, instead of using L significant taps.

Now the LS FFT-based channel estimator is ready to be proposed in details. From (4.12), it can be shown that $\hat{\mathbf{H}}_{LS_{ab}}(m) = ([\hat{\mathbf{H}}_{LS}(m)]_{a,(b-1)K+1:bK})^T$. From the channel model in (4.2), $\hat{\mathbf{H}}_{LS_{ab}}(m)$ can be expressed as

$$\hat{\mathbf{H}}_{LS_{ab}}(m) = \mathbf{F}\mathbf{h}_{ab}(m) + \mathbf{N}_{1_{ab}}(m), \tag{4.16}$$

where $\mathbf{F}$ is the $K \times L$ matrix whose element $[\mathbf{F}]_{xy}$ is defined by $\exp[(-j2\pi/K)(x-1)\tau_y]$, $x = 1, \ldots, K$, $y = 0, \ldots, L-1$; $\mathbf{h}_{ab}(m) = [h_{ab}(m,0), \ldots, h_{ab}(m, L-1)]^T$; and $\mathbf{N}_{1_{ab}}(m) = ([\mathbf{N}_1(m)]_{a,(b-1)K+1:bK})^T$. Notice that the LS channel estimate in (4.16) indeed represents the K-tap LS FFT-based channel estimate for a^{th} receive and b^{th} transmit antennas.

Transforming the PEDB-LS channel estimate in (4.16) to the temporal PEDB-LS channel estimate by using the $K \times K$ IFFT matrix $\mathbf{G}$, whose element $[\mathbf{G}]_{xy}$ is defined by $\frac{1}{K}\exp(j2\pi/K)(x-1)(y-1)$, $x, y = 1, \ldots, K$, it can be shown that

$$\hat{\mathbf{h}}_{LS_{ab}}(m) = \mathbf{G}\hat{\mathbf{H}}_{LS_{ab}}(m) = \mathbf{G}\mathbf{F}\mathbf{h}_{ab}(m) + \mathbf{G}\mathbf{N}_{1_{ab}}(m). \tag{4.17}$$

From the fact that

$$[\mathbf{G}\mathbf{F}]_{xy} = \tfrac{f(x-1-\tau_y)}{K}\exp(j\xi(x-1-\tau_y)),\ x = 1, \ldots, K,\ y = 0, \ldots, L-1, \tag{4.18}$$

where $f(q) = \frac{\sin(\pi q)}{\sin(\pi q/K)}$ is the leakage function and $\xi = \frac{(K-1)\pi}{K}$. Note that if q is equal to an integer number, then $f(q) = 0$; if q is equal to zero, then $f(0) = K$. The illustration of the magnitude of $f(q)$ is shown in Fig.4.1. Substituting (4.18) into (4.17) results in

$$\begin{aligned}\mathbf{G}\mathbf{F}\mathbf{h}_{ab}(m) = \tfrac{1}{K}[&\textstyle\sum_{l=0}^{L-1} h_{ab}(m,l)f(-\tau_l)e^{j\xi(-\tau_l)}, \ldots, \\ &\textstyle\sum_{l=0}^{L-1} h_{ab}(m,l)f(K-1-\tau_l)e^{j\xi(K-1-\tau_l)}]^T.\end{aligned} \tag{4.19}$$

Let $\mathbf{N}^G_{1_{ab}}(m) = \mathbf{G}\mathbf{N}_{1_{ab}}(m)$, then substituting $\mathbf{N}^G_{1_{ab}}(m)$ and (4.19) into (4.17), and let

$$\hat{\mathbf{h}}_{LS_{ab}}(m) = [g(1), \ldots, g(K)]^T, \tag{4.20}$$

it can be shown that

$$g(x) = \frac{1}{K}\sum_{l=0}^{L-1} h_{ab}(m,l)f(x-1-\tau_l)e^{j\xi(x-1-\tau_l)} + N^G_{1_{ab}}(m,x) \tag{4.21}$$

with $N^G_{1_{ab}}(m,x)$ being the x^{th} element of $\mathbf{N}^G_{1_{ab}}(m)$.

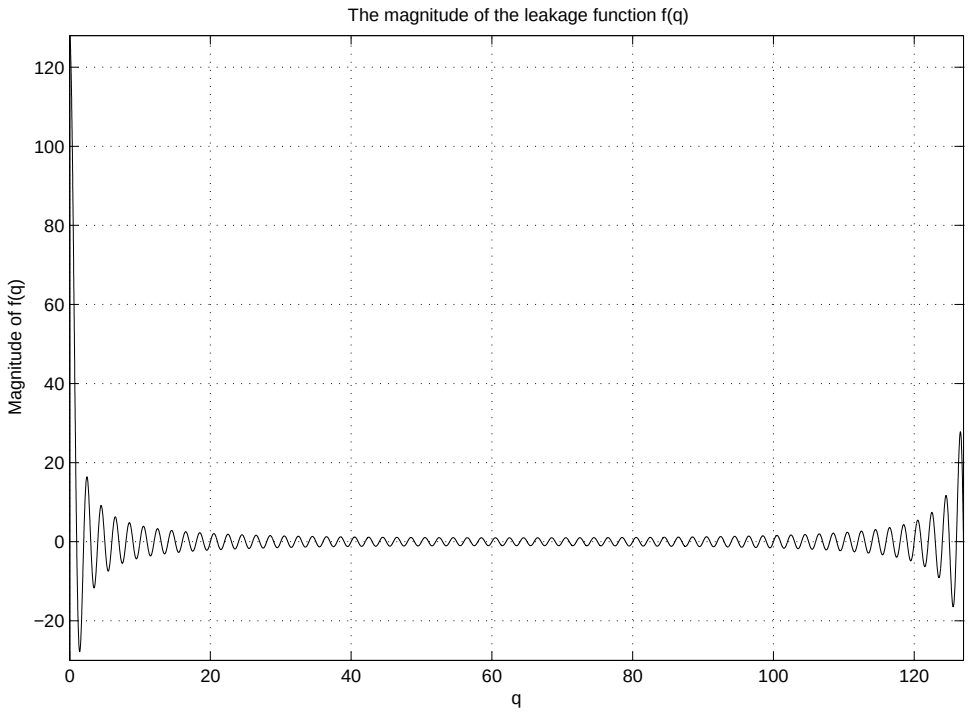

Figure 4.1 The graph of the magnitude of the leakage function $f(q)$.

Obviously, from (4.21), if τ_l is an integer number, then the l^{th} element of the L largest elements of $\hat{\mathbf{h}}_{LS_{ab}}(m)$ is equal to $h_{ab}(m,l)+N^G_{1_{ab}}(m,l)$, and the rest elements, which are not a member of the L largest elements, are equal to $N^G_{1_{ab}}(m,e),\ e\neq l,\ e\in\{0,\ldots,K-1\}\backslash\Xi_1$ with Ξ_1 being the set of the L largest elements. As a result, by choosing L largest taps and replacing the $(K-L)$ remaining taps by zero is sufficient and optimal, resulting in the LS FFT-based estimate of the temporal channel impulse response $\hat{\mathbf{h}}_{FFT_{ab}}(m)$, since the channel impulse response $\mathbf{h}_{ab}(m)$ is completely captured, and the excessive noise in the $(K-L)$ remaining taps is also completely removed. However, in reality, the l^{th} multipath delay τ_l is often a non-integer number, hence, the L-multipath channel impulse response dissipates to all K taps of $\hat{\mathbf{h}}_{LS_{ab}}(m)$ and thus results in the *model mismatch error*, which increases the channel estimation error, primarily caused by the AWGN $\mathbf{N}^G_{1_{ab}}(m)$. This additional channel estimation error causes the severe error floor in the MSE of the channel estimation, and the detection error probability. Once the L or P largest taps are chosen and the rest taps are replaced by zero, the LS FFT-based estimated channel frequency response is determined by

$$\hat{\mathbf{H}}_{FFT_{a,b}}(m)=K\mathbf{G}^H\hat{\mathbf{h}}_{FFT_{ab}}(m). \tag{4.22}$$

It is worth mentioning that, for this problem, there is no assumption about the

knowledge of channel correlation information or Doppler's shift, so that $\hat{\mathbf{h}}_{FFT_{ab}}(m)$ can be simply used for constructing the whole channel frequency response in (4.22). In addition, if the additional information about channel correlation or Doppler's shift are available, the robust channel estimator proposed in [81] can be used to enhance the performance of the LS FFT-based channel estimation.

4.4.2 Channel Estimation Error Performance Analysis

The performance of the PEDB-LS and LS FFT-based channel estimators is now analyzed by using the MSE of channel estimation as the performance measure.

4.4.2.1 Pilot-Embedded Data-Bearing Least Square Channel Estimator

For arbitrary multipath delay profiles, the temporal channel impulse response between the a^{th} receiver and b^{th} transmitter can be described by, as in (4.19),

$$\mathbf{h}_{ab}^{G}(m) = \mathbf{GFh}_{ab}(m). \tag{4.23}$$

The channel estimation error can be readily described by

$$\tilde{\mathbf{h}}_{LS_{ab}}(m) = \mathbf{h}_{ab}^{G}(m) - \hat{\mathbf{h}}_{LS_{ab}} = -\mathbf{N}_{1_{ab}}^{G}(m), \tag{4.24}$$

by referring to $\hat{\mathbf{h}}_{LS_{ab}}(m)$ in (4.17), and $\mathbf{h}_{ab}^{G}(m)$ in (4.23). Using (4.24), the MSE of the channel estimation is expressed as

$$\text{MSE}_{LS}(a,b) = \text{E}[\|\tilde{\mathbf{h}}_{LS_{ab}}(m)\|^2] = \text{E}[\|-\mathbf{N}_{1_{ab}}^{G}(m)\|^2] = \frac{\sigma^2}{\alpha}, \tag{4.25}$$

by using $\text{E}[|N_{1_{ab}}^{G}(m,x)|^2] = \frac{\sigma^2}{K\alpha},\ x = 1,\ldots,K$, as referring to section III.B. It is worth noticing that (4.25) is also the MSE of the K-tap FFT-based channel estimation.

For a L_r-receiver L_t-transmitter MIMO systems, the overall MSE_{LS} in (4.25) can be expressed as follows,

$$\text{MSE}_{LS}^{T} = \sum_{a=1}^{L_t}\sum_{b=1}^{L_r}\text{MSE}_{LS}(a,b) = \frac{\sigma^2 L_t L_r}{\alpha}. \tag{4.26}$$

4.4.2.2 Least Square FFT-Based Channel Estimator

As mentioned earlier, the LS FFT-based channel estimator first simply chooses the L largest taps, and then replaces the $(K-L)$ remaining taps by zero. This operation can be

equivalently described by using the $K \times K$ tap-selection matrix $\mathbf{T}$ given by

$$\mathbf{T} = \text{diag}\{1, 1, \ldots, 0, 1, \ldots, 0\}, \tag{4.27}$$

where 0's and 1's represent non-selected and selected taps, respectively. There are $(K - L)$ 0's and L 1's elements in the diagonal elements of $\mathbf{T}$. By using the tap-selection matrix $\mathbf{T}$, the temporal LS FFT-based-estimate of the channel impulse response between the a^{th} receiver and b^{th} transmitter can be described by

$$\hat{\mathbf{h}}_{FFT_{ab}}(m) = \mathbf{TG}\hat{\mathbf{H}}_{LS_{ab}}(m) = \mathbf{TGF}\mathbf{h}_{ab}(m) + \mathbf{TGN}_{1_{ab}}(m), \tag{4.28}$$

by plugging in $\hat{\mathbf{H}}_{LS_{ab}}(m)$ in (4.16).

Similarly to (4.24), the channel estimation error can be described by, using $\mathbf{h}^G_{ab}(m)$ in (4.23) and $\hat{\mathbf{h}}_{FFT_{ab}}(m)$ in (4.28),

$$\tilde{\mathbf{h}}_{FFT_{ab}}(m) = \mathbf{h}^G_{ab}(m) - \hat{\mathbf{h}}_{FFT_{ab}}(m) = (\mathbf{GF} - \mathbf{TGF})\mathbf{h}_{ab}(m) - \mathbf{TGN}_{1_{ab}}(m). \tag{4.29}$$

Now defining $\Xi_2 \in \{0, \ldots, K-1\} \backslash \Xi_1$ to be a set of the non-selected $(K - L)$ less significant taps, and $w_2 \in \Xi_2$ and $w_1 \in \Xi_1$ are row indices indicating the 0's and 1's elements of $\mathbf{T}$, respectively. It can be shown that

$$[\mathbf{GF} - \mathbf{TGF}]_{w_2,1:L} = \tfrac{1}{K}[f(w_2 - 1)e^{j\xi(w_2-1)}, \ldots, f(w_2 - 1 - \tau_{L-1})e^{j\xi(w_2-1-\tau_{L-1})}], \tag{4.30}$$

by using (4.18) and $\tau_0 = 0$. Therefore, by substituting (4.30) into (4.29), each part of the channel estimation error can be expressed as follows,

$$\begin{aligned} [(\mathbf{GF} - \mathbf{TGF})\mathbf{h}_{ab}(m)]_{w_1 \in \Xi_1} &= [\mathbf{TGN}_{1_{ab}}(m)]_{w_2 \in \Xi_2} = 0, \\ [(\mathbf{GF} - \mathbf{TGF})\mathbf{h}_{ab}(m)]_{w_2 \in \Xi_2} &= \tfrac{1}{K} \textstyle\sum_{l=0}^{L-1} h_{ab}(m, l) f(w_2 - 1 - \tau_l) e^{j\xi(w_2-1-\tau_l)}, \text{ and} \\ [\mathbf{TGN}_{1_{ab}}(m)]_{w_1 \in \Xi_1} &= [\mathbf{N}^G_{1_{ab}}(m)]_{w_1 \in \Xi_1}. \end{aligned} \tag{4.31}$$

From (4.31), it is readily shown that the channel estimation error of the LS FFT-based channel estimator are due to two error sources: the model mismatch error, i.e. $[(\mathbf{GF} - \mathbf{TGF})\mathbf{h}_{ab}(m)]_{w_2 \in \Xi_2}$, and the corresponding noise effect, i.e. $[\mathbf{TGN}_{1_{ab}}(m)]_{w_1 \in \Xi_1}$. By substituting (4.31) into (4.29), we have the MSE of the LS FFT-based channel estimator as

$$\begin{aligned} \text{MSE}_{FFT}(a, b) = \text{E}[\|\tilde{\mathbf{h}}_{FFT_{ab}}(m)\|^2] = \tfrac{1}{K^2} \textstyle\sum_{w_2 \in \Xi_2} \sum_{l=0}^{L-1} \text{E}[|h_{ab}(m, l) f(w_2 - 1 - \tau_l)|^2] \\ + \tfrac{L\sigma^2}{K\alpha}, \end{aligned} \tag{4.32}$$

where the second equality is obtained by using the assumption that the channel and noise, and channels from different paths are mutually uncorrelated. For a L_r-receiver L_t-transmitter MIMO systems, the overall MSE_{FFT} in (4.32) can be expressed as follows,

$$\text{MSE}_{FFT}^{T} = \frac{1}{K^2}\sum_{a=1}^{L_r}\sum_{b=1}^{L_t}\sum_{w_2\in\Xi_2}\sum_{l=0}^{L-1}\text{E}[|h_{ab}(m,l)f(w_2-1-\tau_l)|^2] + \frac{L\sigma^2 L_t L_r}{K\alpha}. \tag{4.33}$$

Defining the first term as χ, it can be shown that

$$\begin{aligned}\chi &= \sum_{a=1}^{L_r}\sum_{b=1}^{L_t}\sum_{w_2\in\Xi_2}\sum_{l=0}^{L-1}\text{E}[|h_{ab}(m,l)f(w_2-1-\tau_l)|^2] \triangleq \chi_1-\chi_2,\\ &= \sum_{a=1}^{L_r}\sum_{b=1}^{L_t}\sum_{j=1}^{K}\sum_{l=0}^{L-1}\text{E}[|h_{ab}(m,l)f(j-1-\tau_l)|^2] - \sum_{a=1}^{L_r}\sum_{b=1}^{L_t}\sum_{w_1\in\Xi_1}\sum_{l=0}^{L-1}\text{E}[|h_{ab}(m,l)f(w_1-1-\tau_l)|^2].\end{aligned} \tag{4.34}$$

Thus (4.33) can be rewritten as

$$\text{MSE}_{FFT}^{T} = \frac{\chi}{K^2} + \frac{L\sigma^2 L_t L_r}{K\alpha}. \tag{4.35}$$

From the fact that

$$\frac{1}{K^2}\chi_1 + \eta_1 = \sum_{a=1}^{L_r}\sum_{b=1}^{L_t}\sum_{j=1}^{K}\text{E}[\|[\hat{\mathbf{h}}_{LS_{ab}}(m)]_j\|^2] - \eta_2,$$

where $\eta_1 = \frac{L\sigma^2 L_t L_r}{K\alpha}$ and $\eta_2 = \frac{(K-L)\sigma^2 L_t L_r}{K\alpha}$; and that

$$\frac{1}{K^2}\chi_2 + \eta_1 = \sum_{a=1}^{L_r}\sum_{b=1}^{L_t}\sum_{w_1\in\Xi_1}\text{E}[\|[\hat{\mathbf{h}}_{LS_{ab}}(m)]_{w_1}\|^2];$$

it can be shown that

$$\frac{\chi}{K^2} = \sum_{a=1}^{L_r}\sum_{b=1}^{L_t}\sum_{j=1}^{K}\text{E}[\|[\hat{\mathbf{h}}_{LS_{ab}}(m)]_j\|^2] - \eta_2 - \sum_{a=1}^{L_r}\sum_{b=1}^{L_t}\sum_{w_1\in\Xi_1}\text{E}[\|[\hat{\mathbf{h}}_{LS_{ab}}(m)]_{w_1}\|^2]. \tag{4.36}$$

First, let consider the case of the multipath delay profiles with integer delays. In this case, the model mismatch error χ is equal to zero, as explained in section 4.4.1. Hence, the minimum MSE of the LS FFT-based channel estimation is given by

$$\text{MSE}_{FFT_{min}}^{T} = \frac{L\sigma^2 L_t L_r}{K\alpha}. \tag{4.37}$$

It is worth noticing that, since $L \leq K$, (4.37) is always less than or equal to (4.26), meaning that the channel estimation performance of the LS FFT-based channel estimator is superior

to that of the PEDB-LS channel estimator when the multipath delay profiles are with integer delays.

Using $\chi = 0$ for the case of the multipath delay profiles with integer delays, it can be shown that

$$\sum_{a=1}^{L_r}\sum_{b=1}^{L_t}\sum_{w_1\in\Xi_1}\mathrm{E}[\|[\hat{\mathbf{h}}_{LS_{ab}}(m)]_{w_1}\|^2] = \sum_{a=1}^{L_r}\sum_{b=1}^{L_t}\sum_{j=1}^{K}\mathrm{E}[\|[\hat{\mathbf{h}}_{LS_{ab}}(m)]_{j}\|^2] - \frac{(K-L)\sigma^2 L_t L_r}{K\alpha}. \tag{4.38}$$

Therefore, (4.38) can be used as the optimal criterion in choosing the set Ξ_1 which indicates the indices of the L significant taps, in order to achieve the a minimum MSE. This observation in (4.38) indicates that in order to achieve the minimum MSE of the LS FFT-based channel estimator, the L largest taps must be capable of capturing the average total energy of channels in the presence of AWGN.

Further, let consider the case of the multipath delay profiles with non-integer delays. In this case, a non-zero model mismatch error χ exists, as shown in (4.35), due to the leakage phenomenon. It is important to study the joint effects of the tap length L and the noise level σ^2 on the MSE measure. In (4.35), it can be seen that MSE_{FFT}^{T} includes two terms: the error due to the model mismatch and the error due to the noise effect. From the definition of the model mismatch error χ, it is straightforward to see that, as increasing the number of selected taps L, the model mismatch error χ decreases, so does the first term in (4.35); however, the resulting noise effect contained in these selected taps is inevitably increased, as shown by the second term in (4.35). On the other hand, as decreasing L, the model mismatch error is therefore increased, whereas the resulting noise effect is decreased. This tradeoff between the model mismatch error and noise effect is very crucial to the MIMO system performances, e.g. the channel estimation error and the detection probability. In what follows, an improvement of the LS FFT-based channel estimator is proposed to overcome such problems.

4.5 The Proposed Adaptive Least Square FFT-Based Channel Estimator

In this section, an adaptive LS FFT-based channel estimation approach in which the number of taps used in channel estimation can be adjustable in order to minimize the model mismatch error and the corresponding noise effect is proposed. The model mismatch error

in the LS FFT-based channel estimation stems from the fact that a fixed number of L (or P) largest taps is used in the channel estimation process for all signal-to-noise ratio (SNR) values. It has been suggested in [76] that, in low SNR regimes, the channel estimation error is mainly caused by the AWGN, hence, a small number of taps is recommended in order to reduce the noise effect; as a result, a smaller overall channel estimation error is possible. In high SNR regimes, the channel estimation error is mainly caused by the model mismatch error, hence, a large number of taps is suggested in order to compensate this model mismatch error. Based on this basic idea, the adaptive LS FFT-based channel estimation approach, in which the number of taps P is chosen to achieve the intuitive goal that the average total energy of the channels dissipating in each tap is completely captured in order to compensate the model mismatch error, is proposed. Specifically, the proposal is that the number of taps P_{opt} used to capture the CSI in $\hat{\mathbf{h}}_{LS_{ab}}(m)$ in (4.20) is obtained by solving the following optimization problem:

$$P_{opt} = \min(P) \quad \text{s.t.}$$
$$\sum_{a=1}^{L_r}\sum_{b=1}^{L_t} \mathrm{E}\left[\max_{\Xi_p,|\Xi_p|=P} \sum_{i\in\Xi_p} \|[\hat{\mathbf{h}}_{LS_{ab}}(m)]_i\|^2\right] \geq$$
$$\sum_{a=1}^{L_r}\sum_{b=1}^{L_t}\sum_{j=1}^{K} \mathrm{E}[\|[\hat{\mathbf{h}}_{LS_{ab}}(m)]_j\|^2] - \frac{(K-P)L_tL_r\sigma^2}{K\alpha}. \tag{4.39}$$

It is clear that, for a given P, the solution of achieving $\max_{\Xi_p,|\Xi_p|=P} \sum_{i\in\Xi_p} \|[\hat{\mathbf{h}}_{LS_{ab}}(m)]_i\|^2$ is to choose Ξ_p as the indices of the P largest taps.

Now let intuitively explain why (4.39) in details. If a perfect situation is assumed, then the most desired criteria used to determine the number of taps P is the MSE in equation (4.35), such that the optimization solution is expressed as

$$P_{opt} = \min_P \{\mathrm{MSE}_{FFT}^T(P)\}. \tag{4.40}$$

First, instead of minimizing $\mathrm{MSE}_{FFT}^T(P)$ directly, it is worth taking advantage of specific observations revealed in the two terms of (4.35). In (4.36), it can be seen that choosing $L = K$ yields a zero model mismatch error χ. To illustrate the effects of P (i.e. $P = L$ in equation (4.36) and (4.35)) and σ^2 on the overall MSE measure, considering a specific scenario as in section 4.6, in Fig.4.2, the corresponding χ/K^2 term and the noise error term $\frac{L\sigma^2 L_t L_r}{K\alpha}$ are plotted as a function of P under several SNR levels. From this figure, it is worth

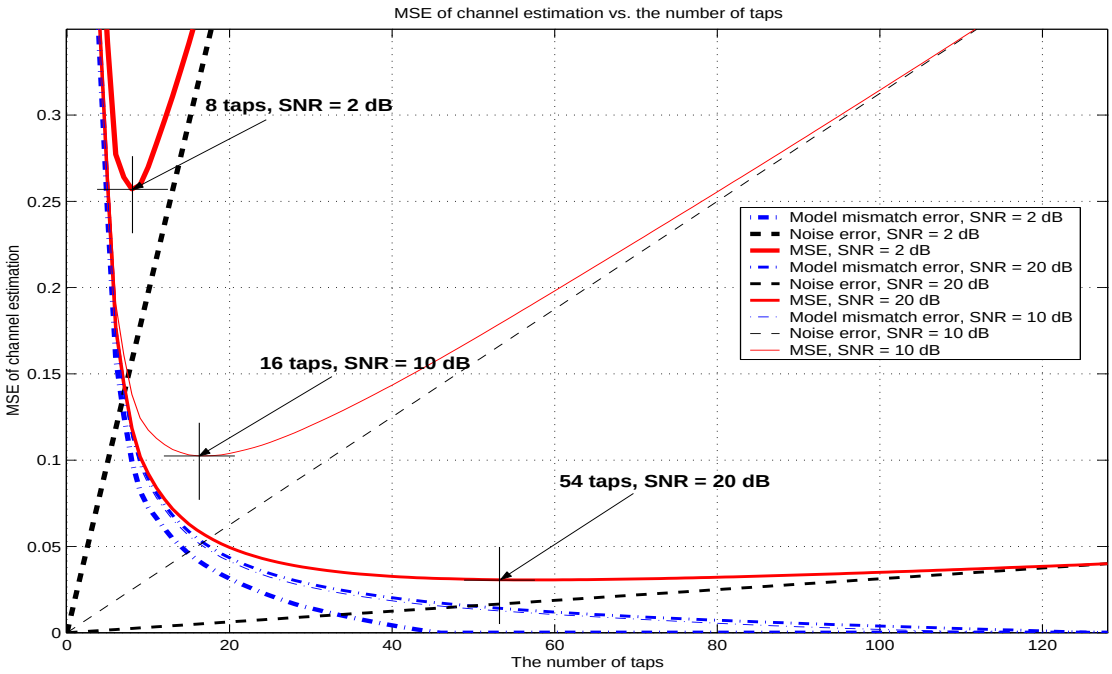

Figure 4.2: Theoretical examples of the model mismatch error, the noise effect, and the overall MSE of the LS FFT-based estimator as a function of the number of taps P. Here the perfect situation is assumed.

noticing that χ/K^2 converges to zero as P increases, meaning that more taps can be used to compensate the model mismatch error. Also, it is seen that the resulting P_{opt} increases as SNR increases. In addition it is noted that P_{opt} can be approximately determined by locating the intersection point of the curve of the model mismatch error and the curve of the noise error. Therefore, based on the above observation, the problem described in (4.40) can be formulated as

$$P_{opt} = \min(P) \quad \text{s.t.} \quad \{\frac{\chi}{K^2} \leq \frac{P\sigma^2 L_t L_r}{K\alpha}\}. \tag{4.41}$$

By substituting (4.36), the problem in (4.41) can be equivalently described as

$$P_{opt} = \min(P) \quad \text{s.t.}$$
$$\sum_{a=1}^{L_r}\sum_{b=1}^{L_t}\sum_{i\in\Xi_p} \mathrm{E}\left[\|[\hat{\mathbf{h}}_{LS_{ab}}(m)]_i\|^2\right] + \frac{P\sigma^2 L_t L_r}{K\alpha} \geq$$
$$\left(\sum_{a=1}^{L_r}\sum_{b=1}^{L_t}\sum_{j=1}^{K} \mathrm{E}[\|[\hat{\mathbf{h}}_{LS_{ab}}(m)]_j\|^2] - \frac{(K-P)L_t L_r \sigma^2}{K\alpha}\right). \tag{4.42}$$

However, in practice, since Ξ_p is an unknown set, it is not feasible to compute the

term

$$\sum_{a=1}^{L_r}\sum_{b=1}^{L_t}\sum_{i\in\Xi_p}\mathrm{E}\left[\|[\hat{\mathbf{h}}_{LS_{ab}}(m)]_i\|^2\right]$$

directly. In stead, for each transmission, depending on the real observations, for different P, the term $\max_{\{\Xi_p,|\Xi_p|=P\}}\sum_{i\in\Xi_p}\|[\hat{\mathbf{h}}_{LS_{ab}}(m)]_i\|^2$ can be instantaneously computed. Then empirical expectation is calculated. Overall, the following term is to be computed

$$\sum_{a=1}^{L_r}\sum_{b=1}^{L_t}\mathrm{E}\left[\max_{W_p,|W_p|=P}\sum_{i\in W_p}\|[\hat{\mathbf{h}}_{LS_{ab}}(m)]_i\|^2\right].$$

Since

$$\sum_{a=1}^{L_r}\sum_{b=1}^{L_t}\mathrm{E}\left[\max_{\Xi_p,|\Xi_p|=P}\sum_{i\in\Xi_p}\|[\hat{\mathbf{h}}_{LS_{ab}}(m)]_i\|^2\right]\geq\sum_{a=1}^{L_r}\sum_{b=1}^{L_t}\sum_{i\in\Xi_p}\mathrm{E}\left[\|[\hat{\mathbf{h}}_{LS_{ab}}(m)]_i\|^2\right], \quad (4.43)$$

where Ξ_p is a set of the P largest taps. In low SNR regimes, the l.h.s of (4.43) is much larger than that of r.h.s because of the large noise variance. In high SNR regimes, the l.h.s of (4.43) is much closer to that of the r.h.s because of the small noise variance. Intuitively it can be seen that the l.h.s consists of both the r.h.s and the noise effect. It is worth noticing that the left hand is based on order statistics. In this case, since the components in $\hat{\mathbf{h}}_{LS_{ab}}(m)$ follow non-identical distributions, due to the complex nature of order statistics, it is infeasible to find the theoretical close-form expression of the l.h.s of (4.43) in term of the r.h.s of (4.43). Due to the inequality in (4.43), one most interesting question is how close the difference between the l.h.s and the r.h.s of (4.43) to the noise error $\frac{L\sigma^2L_tL_r}{K\alpha}$ is. Numerical examples are plotted in Fig.4.3 to demonstrate the relationship between the l.h.s of (4.42) and the l.h.s of (4.43). From Fig.4.3, it can be seen that the curves of the l.h.s of (4.42) and (4.43) are close together when the number of taps are small until the intersection point between these two curves and the r.h.s of (4.42) for both SNR = 2 and 20 dB. This phenomenon indicates that by replacing the l.h.s of (4.42) by the l.h.s of (4.43) for determining the minimum number of taps that yield the equality to the constraint of (4.42), the resulting number of taps are mostly the same as solving (4.42) directly. It is worth noticing that in the regimes beyond the intersection point, these two curves are different; however, this phenomenon does not affect the minimum number of taps since their relationship in these regimes have never been exploited.

Based on the above observations, the l.h.s of (4.42) is proposed to be replaced by the l.h.s of (4.43), and thus the inequality constraint in (4.42) is replaced by the inequality

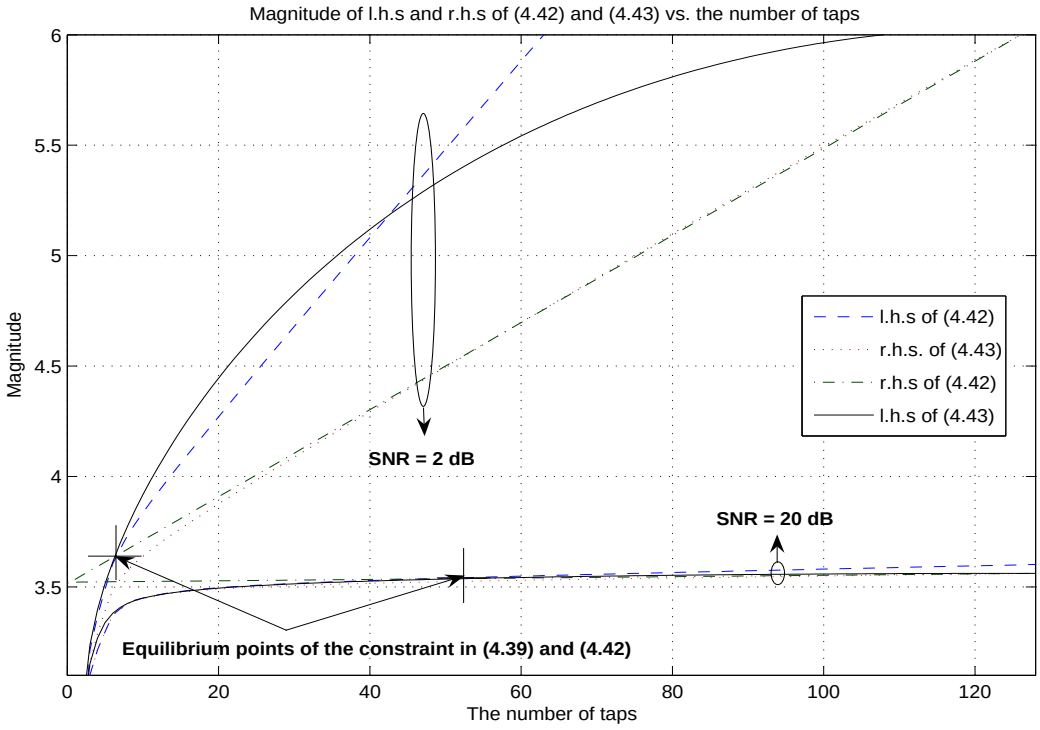

Figure 4.3: The relationship between l.h.s and r.h.s of (4.42) and (4.43) based on numerical calculations.

constraint in (4.39). Therefore, the proposed scheme for determining P_{opt} can be shown in (4.39). In this sense, one could regard the proposed scheme in (4.39) as a sub-optimal approach in determining P_{opt}. However, as illustrated in Fig.4.4, in most cases the P_{opt} determined by solving the problem in (4.39) is almost identical to the optimum solution obtained by using an exhaustive search for the minimum MSE_{FFT}^{T} in (4.35). While the later case is not practical and thus serves as a theoretical ideal solution. Further, studying the problem described in (4.39), it can be seen that in low SNR regimes, due to the large noise variance, a small number of taps is enough to make the constraint of (4.39) existed. In high SNR regimes, a large number of taps is needed, as expected, in order to make the constraint of (4.39) existed. These results is consistent with the intuitions. The equality will be held for (4.43) if and only if $\sigma^2 = 0$ or $P = K$.

It is worth emphasizing that the solution of (4.39) is the optimum number of taps for the LS FFT-based channel estimator in the sense that the average total energy of the channels dissipating in each tap is completely captured by using the P_{opt} significant taps; as a result, the minimum model mismatch error as well as the minimum corresponding noise

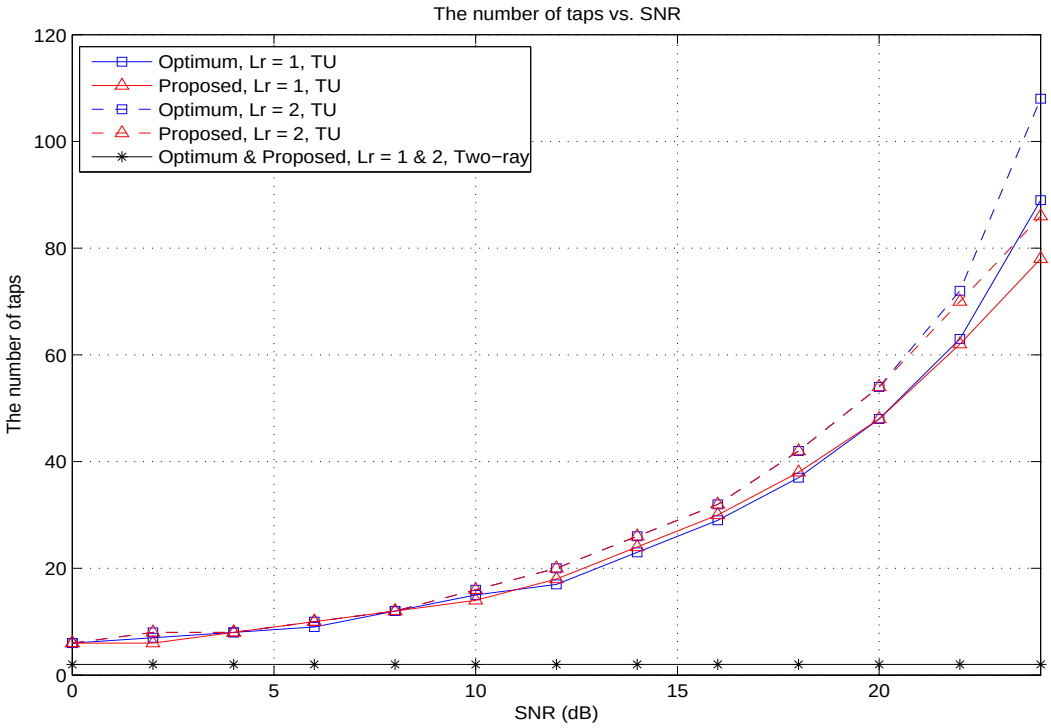

Figure 4.4: Illustration of the number of taps of the proposed scheme in (4.39) compared with the optimum number of taps obtained from an exhaustive search for the minimum MSE_{FFT}^{T} in (4.35) in two different power delay profiles: typical urban and two-ray power delay profiles with delay spread of 5 μs.

effect are achieved.

To illustrate different patterns about the optimum number of taps obtained from (4.39) under different delay profiles with delay spread of 5 μs, both the two-ray delay profile, where the delays τ_l's take integer values, and the typical urban (TU) six-ray delay profile, where non-integer τ_l's are observed, are investigated. In addition, the setting parameters of this experiment are described is section 4.6. As in Fig.4.4, it can be seen that the optimum number of taps, the solution of (4.39), for the two-ray delay profile are constantly equal to 2 for all SNR values, whereas, for that of the TU six-ray profile, the optimum number of taps increase as the SNR value increases. The phenomenon supports the derivations in section 4.4.1 and above discussions as well.

4.6 Simulation Results

To illustrate the performance of the proposed scheme, simulations are conducted under two different scenarios: quasi-static and nonquasi-static frequency-selective Rayleigh fading channels. The simulated SF block code is obtained from Alamouti's structure [?], as proposed in [72], whose elements are taken from a BPSK constellation for two transmit antennas and two receive antennas. The COST207 typical urban (TU) six-ray normalized power delay profile [87] with delay spread of 5 μs is studied. The entire channel bandwidth, 1 MH_z, is divided into $K = 128$ subcarriers in which four subcarriers on each end are served as guard tones, and the rest (120 tones) are used to transmit data. To make the tone orthogonal to each other, the symbol duration is 128 μs, and additional 20 μs guard interval is used as the cyclic prefix length in order to protect the ISI due to the multipath delay spread. This results in a total block length $T_f = 148$ μs and a subchannel symbol rate $r_b = 6.756$ KBd.

In addition, the equal block-power allocation, i.e. $\beta = \alpha = 0.5$ W, is employed, the normalized SF-coded symbol block-power is 1 W, the number of transmit antennas L_t is 2, $N = 2$, and $M = N + L_t = 4$. To illustrate the performance of the proposed adaptive LS FFT-based channel estimation versus the PEDB-LS and LS FFT-based channel estimations, the CM-based structure in (4.8), which is the best structure for nonquasi-static fading channels, is selected as the representative of three structures studied in [74].

4.6.1 The Quasi-Static Fading Channel

In this scenario, the channel impulse response $h_{ab}(m, l)$'s in (4.2) are from the normalized time-varying channel which is modelled as Jake's model [51], when $f_d * T_f = 0.08$ (fast fading) with f_d being the Doppler's shift.

In Fig.4.5, the MSEs of the PEDB-LS, 10-tap LS FFT-based, adaptive LS FFT-based, and LMMSE channel estimators [75], when 2 receive antennas are employed, are shown. Notice that the PEDB-LS channel estimator has a higher MSE in low SNR regimes than that of the 10-tap LS FFT-based and the adaptive LS FFT-based channel estimators. This is due to the severe noise effect corrupting in all K channel estimate taps; whereas the latter two employ small number of taps resulting in the lower noise effect. In high SNR regimes, the PEDB-LS and adaptive LS FFT-based channel estimators performs better than the 10-tap

LS FFT-based channel estimator in which the error floor caused by the model mismatch error occurs, whereas the former two do not suffer from this severe error floor since they employ more taps and thus result in a lower model mismatch error. It is worth noticing that the LMMSE channel estimator serves as the channel estimation performance bound at the price of the intensive computational complexity and the additional information about channel correlation.

In Fig.4.6, the BERs of the SF-coded MIMO-OFDM system employing the PEDB-LS, 10-tap LS FFT-based, adaptive LS FFT-based, and LMMSE channel estimators, when 2 receive antennas are employed, are shown. Notice that the 10-tap LS FFT-based and adaptive LS FFT-based channel estimator performances are quite close in low SNR regimes, whereas the PEDB-LS channel estimator performs worse, in which the 2-dB SNR difference compared to the former two channel estimators, at BER of 10^{-3}, is observed. In high SNR regimes, the 10-tap LS FFT-based channel estimator suffers from the error floor, say at BER of 2×10^{-4}, whereas the adaptive LS FFT-based and the PEDB-LS channel estimators do not. At BER of 10^{-4}, the SNR differences between the ideal-channel scheme, where the true channel impulse response is employed, and the adaptive LS FFT-based and PEDB-LS channel estimators are 2.2 dB and 3.6 dB, respectively, whereas the LMMSE channel estimator provides the error probability coincide with the ideal-channel scheme.

4.6.2 The Nonquasi-Static Fading Channel

For the sake of exposition, a 4-block fading model is investigated in which the channel impulse response $h_{ab}(m, l)$ symmetrically changes four times within one SF-coded symbol block, i.e. there exists $\mathbf{H}_1(m)$ to $\mathbf{H}_4(m)$ in the m^{th}-block SF-coded symbol matrix.

In Fig.4.7, the BERs of the SF-coded MIMO-OFDM system employing the PEDB-LS, 10-tap LS FFT-based, adaptive LS FFT-based, and LMMSE channel estimators, when 2 receive antennas are employed, and $f_d * T_f$ are 0.04 and 0.064, are shown. Notice that when the Doppler's shift is small ($f_d * T_f = 0.04$) in high SNR regimes, the PEDB-LS, adaptive LS FFT-based, and LMMSE channel estimators are superior to the 10-tap LS FFT-based channel estimator. In low SNR regimes, the 10-tap LS FFT-based, adaptive LS FFT-based, and LMMSE channel estimators outperform the PEDB-LS channel estimator resulting from the severe noise effect. When Doppler's shift is high ($f_d * T_f = 0.064$) in high SNR regimes,

all channel estimators yields quite close results. This phenomenon stems from the fact that the channel mismatch error dominates all factors causing the detection error.

In Fig.4.8, the optimum number of taps of the adaptive LS FFT-based channel estimator, when 2 receive antennas are employed, in both the quasi-static and nonquasi-static fading channels is shown. Notice that, in nonquasi-static fading channels at the particular SNR value, the number of taps is higher than the quasi-static fading channels resulting from the fact that the average energy in each PEDB-LS channel estimate tap of the former case is less than the latter because of the Doppler's shift effect, i.e. the higher channel fluctuation in the SF-coded symbol block; as a result, in order to make the constraint of (4.39) exists, the higher number of taps is required. This phenomenon is also observed when the Doppler's shift increases resulting in the higher number of taps for the higher Doppler's shift case.

In this scenario, there exists the inevitable error floors in the error probability, that increases significantly as the Doppler's shift increses, resulting from the channel mismatch error introduced as the bias in the channel estimate.

4.7 Concluding Remark

In this chapter, the adaptive LS FFT-based channel estimator for improving the channel estimation and detection performances of the LS FFT-based and PEDB-LS channel estimators, and the pilot-embedded data-bearing approach for joint channel estimation and data detection were proposed. Simulations were conducted to examine the performance of the proposed schemes. For quasi-static TU-profile fading channels, the adaptive LS FFT-based channel estimator shows superior performance to that of the 10-tap LS FFT-based and PEDB-LS channel estimators. For instance, at BER of 10^{-4}, the SNR differences are as 2.2 dB and 3.6 dB, respectively, for the adaptive LS FFT-based and the PEDB-LS channel estimators compared with the ideal-channel scheme, whereas the 10-tap LS FFT-based channel estimator suffers from the severe error floor caused by the model mismatch error. For the nonquasi-static TU-profile fading channels, under low Doppler's shift regimes, the adaptive LS FFT-based channel estimator outperforms the 10-tap LS FFT-based and PEDB-LS channel estimators in high SNR regimes; however, in the low SNR regimes, the performance of the PEDB-LS approach is the worst and the other two estimators are comparable. Furthermore, under high Doppler's shift regimes, the channel mismatch error

dominates all factors causing the detection error and thus result in comparable error floors for all channel estimators. In addition, the LMMSE channel estimator serves as a performance bound.

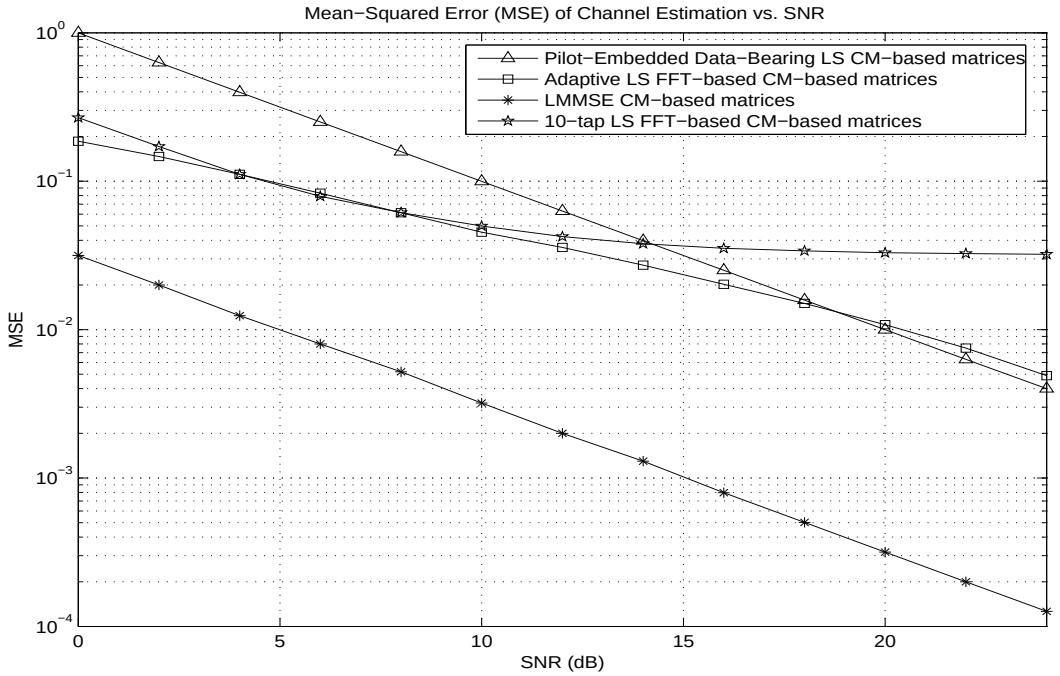

Figure 4.5 The graph of MSEs of the channel estimation in quasi-static fading channels.

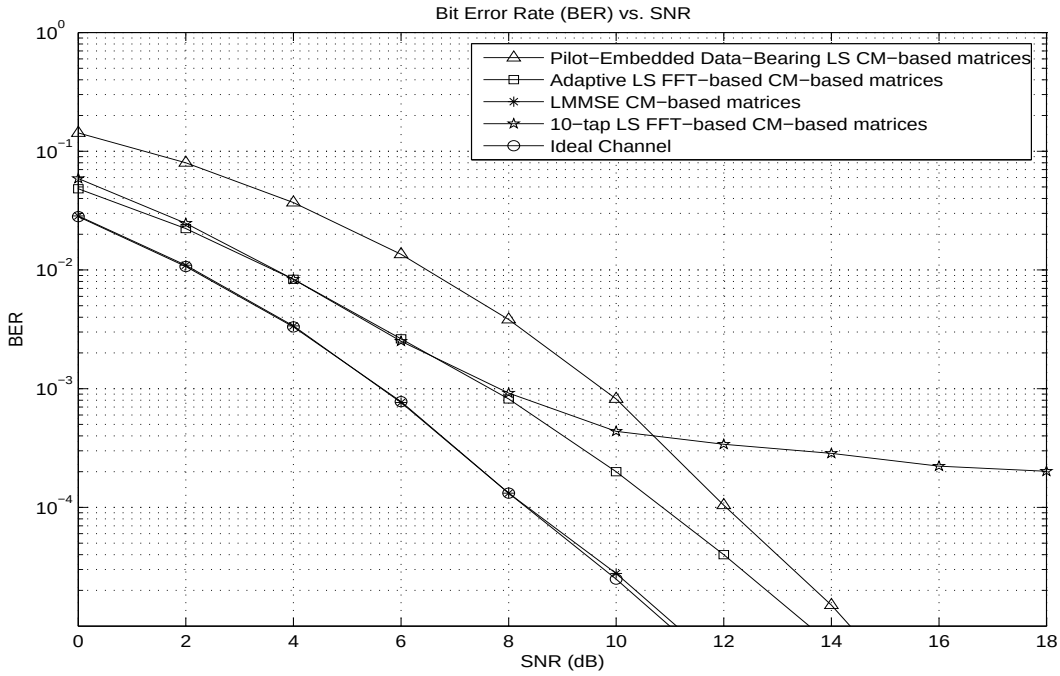

Figure 4.6: The graph of BERs of the pilot-embedded SF-coded MIMO-OFDM system in quasi-static fading channels.

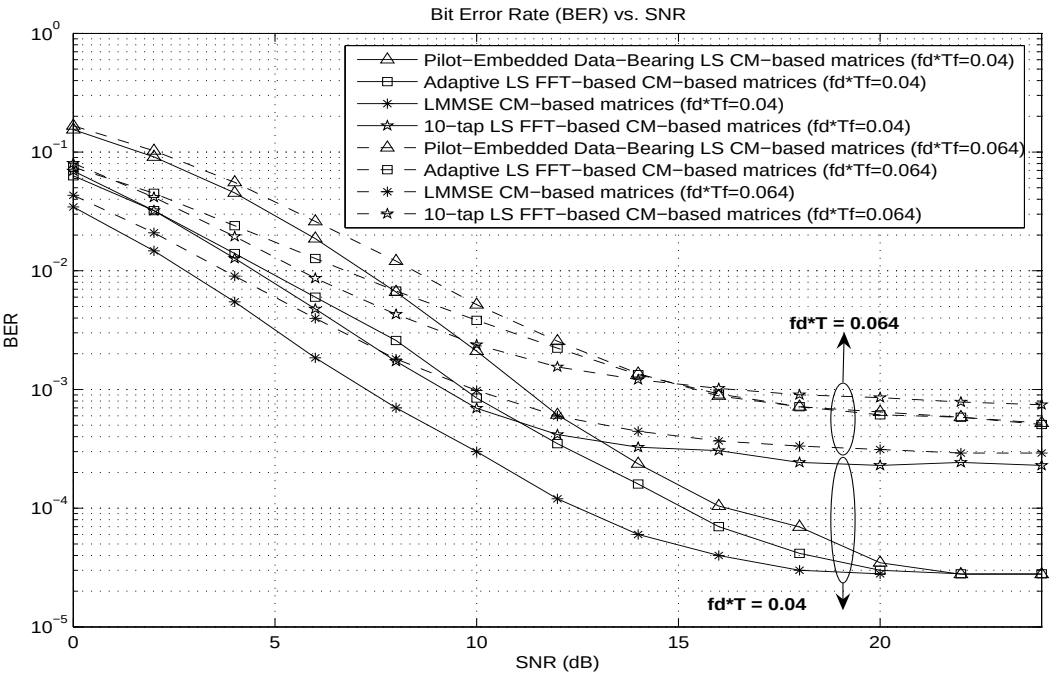

Figure 4.7: The graph of BERs of the pilot-embedded SF-coded MIMO-OFDM system in nonquasi-static fading channels.

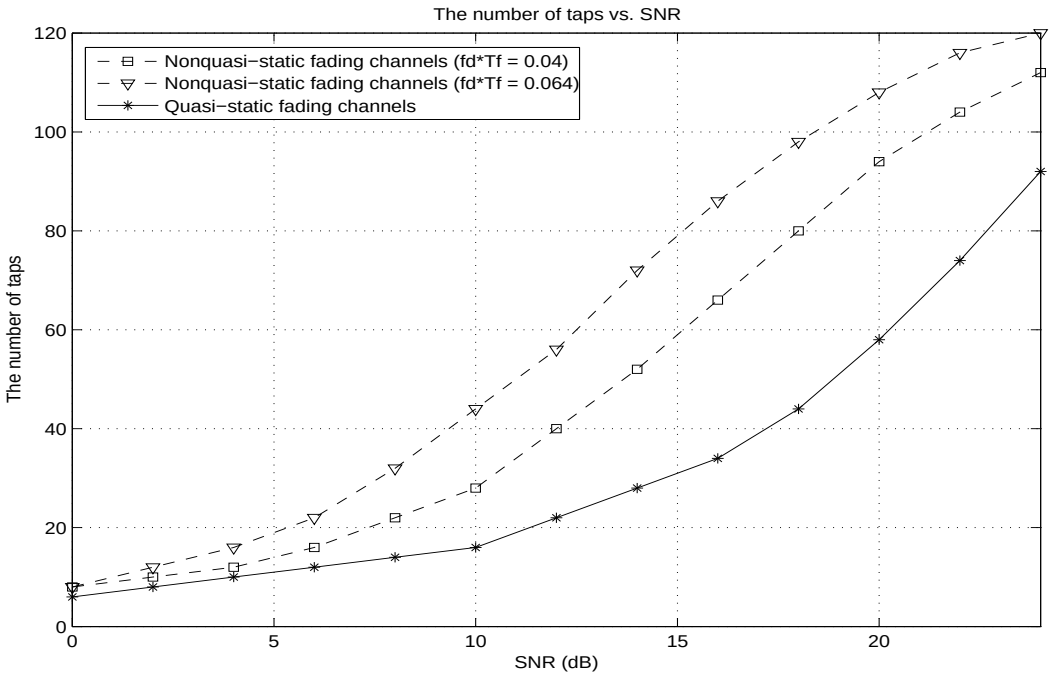

Figure 4.8: The graph of the optimum number of taps in both quasi-static and nonquasi-static fading channels.

CHAPTER V

CONCLUSIONS

In this dissertation, the MIMO wireless communication systems have been investigated in two aspects: the smart antenna system and channel estimation. In chapter 2, it was obvious that the smart antenna system, i.e. IRBAP, has significantly improved the performances of the interference canceling receivers in the DS-CDMA systems in terms of the probability of error and the stability of the system. Although the IRBAP requires more complexity, which is linear with the number of users in the system, than the original scheme, the IRBAP does provide significant benefits, especially in the closely-separated-DOA situation. From the simulation results, the SNR improvement of the IRBAP over the original scheme, e.g. the minimization method, is significant in both the nonordering-user-power closely-separated-DOA and the nonordering-user-power mixed-separated-DOA situations. For instance, in the AWGN channel, the SNR difference is about 0.6 dB in the ordering-user-power mixed-separated-DOA situation, and 10 dB in the nonordering-user-power mixed-separated-DOA situation, at BER=10^{-3}. Furthermore, the probability of error curves of the IRBAP are quit close to that of the theoretical BER. In the AWGN and slow-varying Rayleigh fading channels, the SNR difference is about 2 dB in the ordering-user-power mixed-separated-DOA situation, at BER=10^{-3}; however, in the nonordering-user-power mixed-separated-DOA situation, the minimization method of the existing work diverges at BER=10^{-2} whereas the IRBAP still yields the good BER.

In chapter 3, the data-bearing approach for pilot-embedding frameworks was proposed for joint data detection and channel estimation in ST coded MIMO systems. The main contributions of this chapter are as follows.

- The advantages of the data-bearing approach are that it is the generalized form for pilot-embedded channel estimation and data detection in ST coded MIMO systems, in which the classical channel estimation method, e.g. PSAM, is subsumed; the low computational complexity and the efficient ML and LMMSE channel estimators

are achieved; and it is capable of better acquiring the channel state information in fast-fading channels.

- For the quasi-static flat Rayleigh fading channels, the error probability and the channel estimation performance of three data-bearer and pilot structures, i.e. the TM-, STBC-, and CM-based data-bearer and pilot matrices, are quite similar, where the optimum-power-allocated schemes based on the minimum upper bound on error probability and the maximum lower bound on channel capacity optimizations yield the close results. This result claims that the proposed scheme is one of the implementable scheme that achieves the maximum lower bound on channel capacity derived in [57], in high SNR regimes. In addition, the SNR differences between the optimum-power-allocated schemes and the ideal-channel schemes are about 2.3 dB when employing the unconstrained ML channel estimator and 0.5 dB for the LMMSE channel estimator.

- For the case of nonquasi-static flat Rayleigh fading channels, the CM-based structure provide superior detection and channel estimation performances over the TM- and STBC-based structures. For instance, the 6.02 dB SNR difference is observed, as well as the error floors of the former are much smaller than that of the other two, under fairly high Doppler's shift scenarios, in high SNR regimes.

In addition, the proposed pilot-embedding scheme can be well applied to the general MIMO systems.

In chapter 4, different kinds of channel estimator have been proposed for the SF coded MIMO-OFDM systems. The main contributions of this chapter can be summarized as follows.

- The generalization of the pilot-embedded data-bearing approach for joint channel estimation and data detection for MIMO-OFDM systems, in which PEDB-LS channel estimation and PEDB-ML data detection are employed, respectively, was developed. The LS FFT-based channel estimation was further proposed by employing the FFT-based approach concept to improve the performance of the PEDB-LS channel estimation via choosing certain significant taps in constructing a channel frequency response.

- The performance of the LS FFT-based channel estimation was analyzed. Then the relationship between the MSE and the number of chosen taps was revealed, which in

turn, the optimal criterion for choosing the optimum number of taps was explored.

- The model mismatch error of the LS FFT-based channel estimator was investigated, and the adaptive LS FFT-based channel estimation approach was proposed to solve such problem by employing the optimum number of taps, such that the average total energy of the channels dissipating in each tap is completely captured in order to compensate the model mismatch error as well as minimize the corresponding noise effect, to construct the channel frequency response.

Simulations were conducted to examine the performance of the proposed schemes. For quasi-static TU-profile fading channels, the adaptive LS FFT-based channel estimator shows superior performance to that of the 10-tap LS FFT-based and PEDB-LS channel estimators. For instance, at BER of 10^{-4}, the SNR differences are as 2.2 dB and 3.6 dB, respectively, for the adaptive LS FFT-based and the PEDB-LS channel estimators compared with the ideal-channel scheme, whereas the 10-tap LS FFT-based channel estimator suffers from the severe error floor caused by the model mismatch error. For the nonquasi-static TU-profile fading channels, under low Doppler's shift regimes, the adaptive LS FFT-based channel estimator outperforms the 10-tap LS FFT-based and PEDB-LS channel estimators in high SNR regimes; however, in the low SNR regimes, the performance of the PEDB-LS approach is the worst and the other two estimators are comparable. Furthermore, under high Doppler's shift regimes, the channel mismatch error dominates all factors causing the detection error and thus result in comparable error floors for all channel estimators. In addition, the LMMSE channel estimator serves as a performance bound. In addition, the proposed estimators can be applied to the general MIMO-OFDM systems as well.

Overall, this dissertation achieved its two objectives, which were the novel smart antenna system for DS-CDMA systems and the novel channel estimation approaches for the ST coded MIMO systems and the SF coded MIMO-OFDM systems. Firstly, it was obvious that the proposed smart antenna system, i.e. IRBAP, could be well applied to DS-CDMA systems without requiring the descending order of power for each receiver's stage for IRBAP. It was also robust to the near-far effect situations in such systems, and it was superior to the existing work [19] in term of the probability of detection error.

Secondly, it was clear that the proposed data bearing approach for pilot-embedding yielded significant performance improvement, including the enhanced probability of detection

error in nonquasi-static fading channels, to the ST coded MIMO systems. The optimum power allocation for the pilot and the data parts for the ML channel estimator was also revealed, based on minimizing the Chernoff's upper bound on error probability. This result claimed that this novel channel estimation approach could be applied to the real-world ST coded MIMO communications, where the channels were changing rapidly, with the enhanced probability of detection error in comparison with the traditional approach, i.e. PSAM approach.

For the SF coded MIMO-OFDM systems, the data bearing approach for pilot-embedding could be directly applied with some modifications. It was obvious that the proposed adaptive LS FFT-based channel estimator employing the optimum number of significant taps could jointly optimize the model mismatch error, caused by the non-integer multipath delay profiles for the real-world multipath fading channels, and noise effect, caused by the additive noise, inherent in the MSE of the LS FFT-based channel estimation. As a result, the enhanced probability of detection error as well as the enhanced MSE could be achieved. Hence, this channel estimator could be well applied to the real-world SF coded MIMO-OFDM communications with the enhanced performances in comparison with the proposed PEDB-LS and LS FFT-based channel estimators.

5.1 Future Works

In the future work, the extension of the IRBAP to the multipath fading channels by employing a tap delay line concept [37] is of interest. Since, here, the IRBAP regards the multipath signals as ISI, the null capability of the array antennas has been used to cancel this interference. On the other hand, the multipath signals can be exploited to improve the received SNR as well as the error probability performance of the system by coherently combining these multipath signals together. This idea resembles the concept of a RAKE receiver initially proposed for the conventional CDMA systems. This extension is straightforward, hence, it is not investigated in this dissertation. Assuming the knowledge of time delays of the multipath fading channels at the receiver, it would be interesting in exploiting the concept of the RAKE receiver to improve the performance of IRBAP.

For the data-bearing approach for pilot-embedding, an another optimum power allocation scheme based on a different criterion, e.g. the lower bound on channel capacity, is being

considered for the future work. In fact, such criterion was not considered in this dissertation because this dissertation considered fixed data-rate ST coded MIMO communications. It would be of interest in comparing the performance of such systems employing different power allocation strategies.

Recently, the generalized MIMO systems (i.e. the distributed antenna array), called "Cooperative Communications," are of widespread interest. This communications scheme can take the benefit of the MIMO system, i.e. the diversity gain, by the help of all active users in the wireless networks, e.g. the cellular phone networks. However, many issues have been waiting for being explored, including a protocol design, an effective channel estimation, synchronization, a generalized space-time code design, and scheduling and routing problems. All of these issues are of crucially interest for the future works as well.

References

1. Winters, J. On the capacity of radio communication systems with diversity in a rayleigh fading environment. IEEE Journal on Selected Areas in Communications 5 (June 1987): 871--878.

2. Foschini, G. J. Layered space-time architecture for wireless communication in a fading environment when using multiple antennas. Bell Labs Technical Journals 1 (1996): 41--59.

3. Foschini, G. J. and Gans, M. On limits of wireless communications in a fading environment when using multiple antennas. Wireless Personal Coomunications 6 (March 1998): 311--355.

4. Telatar, E. Capacity of multi-antenna gaussian channels. European Transactions on Telecommunication ETT 10 (November 1999): 585--596.

5. Telatar, E. Capacity of multi-antenna gaussian channels. AT & T Bell Labs International Memorandum (June 1995): 1--12.

6. Goldsmith, A. Wireless Communications. UK : Cambridge University Press, 2005.

7. Zheng, L. and Tse, D. N. Diversity and multiplexing: a fundamental tradeoff in multiple antenna channels. IEEE Transactions on Information Theory 49 (May 2003): 1073--1096.

8. Gamal, H., Caire, G., and Damon, M. Lattice coding and decoding achieve the optimal diversity-multiplexing tradeoff of mimo channels. IEEE Transactions on Information Theory 50 (June 2004): 968--985.

9. Yao, H. and Wornell, G. Structured space-time block codes with optimal diversity-multiplexing tradeoff and minimum delay. Proceeding of IEEE Global Telecommunications Conference 2003 (December 2003): 1941--1945.

10. Gamal, H. E. and Damon, M. O. Universal space-time coding. IEEE Transactions on Information Theory 49, 5 (May 2003): 1097--1119.

11. Damon, M. O., Gamal, H. E., and Beaulieu, N. C. Linear threaded algebraic space-time constellations. IEEE Transactions on Information Theory 49, 10 (October 2003): 2372--2388.

12. Liberti, J. C. and Rappaport, T. S. Smart Antennas for Wireless Communications: IS-95 and Third Generation CDMA Applications. NJ : Prentice Hall, 1999.

13. Tarokh, V., Seshadri, N., and Calderbank, A. R. Space-time codes for high data rate wireless communication: performance criterion and code construction. IEEE Transactions on Information Theory 44 (March 1998): 744--765.

14. Tarokh, V., Seshadri, N., and Calderbank, A. R. Space-time block codes from orthogonal designs. IEEE Transactions on Information Theory 45 (July 1999): 1456--1467.

15. Ding, Z. and Li, Y. (G.) Blind Equalization and Identification. NY : Marcel Dekker, 2001.

16. Cavers, J. K. An analysis of pilot symbol assisted modulation for rayleigh fading channels. IEEE Transactions on Vehicular Technology 40 (November 1991): 686--693.

17. Hoeher, P. and Tufvesson, F. Channel estimation with superimposed pilot sequence. Proceeding of IEEE Global Telecommunications Conference 1999 4 (December 1999): 2162--2166.

18. Sage, A. P. and Melsa, J. L. Estimation Theory with Applications to Cimmunications and Control. NY : McGraw-Hill, 1971.

19. Ghazi-Moghadam, V. and Kaveh, M. A cdma interference canceling receiver with an adaptive blind array. IEEE Journal on Selected Areas in Communications 16, 8 (Oct 1998): 1542--1554.

20. Tsai, J. -A. and Woerner, B. D. Performance of combined mmse beamforming with parallel interference cancellation for overloaded ofdm-cdma systems. Proceeding of IEEE Military Communications Conference 2002 1 (October 2002): 748--752.

21. Nazar, S. N., Ahmad, M. O., Swamy, M. N. S. and Zhu, W. -P. An adaptive parallel interference canceler using adaptive blind arrays. Proceeding of IEEE Vehicular Technology Conference 2002 1 (September 2002): 425--429.

22. Pirak, C., Prayongpun, W., and Jitapunkul, S. The interference-rejected blind array processing for cdma interference cancellation in the near-far situation. Proceeding of World Wireless Congress 2004 (May 2004): 535--539.

23. Hu, C. -C. and Reed, I. S. Space-time adaptive reduced-rank multistage wiener filtering for asynchronous ds-cdma. IEEE Transactions on Signal Processing 52, 7 (July 2004): 1862--1877.

24. Al-Dabbous, N. A. and Sharif, B. S. Adaptive space-time multistage canceller for ds/cdma systems. IEE Electronics Letters 37, 6 (March 2001): 381--383.

25. Yener, A., Yates, R. D., and Ulukus, S. Combined multiuser detection and beamforming for cdma systems: filter structures. IEEE Transactions on Vehicular Technology 51, 5 (September 2002): 1087--1095.

26. Guo, Z. and Letaief, K. B. Adaptive mmse receiver with beamforming for ds/cdma systems. IEEE Transactions on Wireless Communications 2, 4 (July 2003): 605--610.

27. Balanis, C. A. Antenna Theory : analysis and design. NY : Harper & Row, 1982.

28. Keerthi, A. V., Mathur, A., Shynk, J. J., and Gooch, R. P. A blind adaptive antenna system for the estimation of mutually correlated cochannel sources. Proceeding of IEEE Military Communications Conference 1995 3 (November 1995): 1051--1055.

29. Li, Y. and Liu, K. J. R. Adaptive blind source separation and equalization for multiple-input/multiple-output systems. IEEE Transactions on Information Theory 44, 7 (November 1998): 2864--2876.

30. Pirak, C. and Jitapunkul, S. The JADE-estimated cm array for correlated cochannel recovery. Proceeding of IEEE Vehicular Technology Conference 2003 1 (October 2003): 1497--1501.

31. Shynk, J. J. and Gooch, R. P. The constant modulus array for cochannel signal copy and direction finding. IEEE Transactions on Acoustics, Speech, and Signal Processing 44, 3 (March 1996): 652--660.

32. Verdu, S. Multiuser Detection. UK. : Cambridge University Press, 1998.

33. Dominique, F. and Reed, J. H. Despread data rate update multitarget adaptive array for cdma signals. IEE Electronics Letters 33, 2 (January 1997): 119--121.

34. Rong, Z., Petrus, P., Rappaport, T. S., and Reed, J. H. Despread-respread multi-target constant modulus array for cdma systems. IEEE Communications Letters 1, 4 (July 1997): 114--116.

35. Zoltowski, M. D. and Ramos, J. Blind adaptive beamforming for cdma based pcs/cellular. Proceeding of IEEE Asilomar Conference on Signals, Systems and Computers 1995 (November 1995): 378--382.

36. Zoltowski, M. D. and Ramos, J. Blind multi-user access interference cancellation for cdma based pcs/cellular using antenna arrays. Proceeding of IEEE International Conference on Acoustics, Speech, and Signal Processing 1996 (May 1996): 2730--2733.

37. Chen, Y. -F. and Zoltowski, M. D. Blind rls based space-time adaptive 2-d rake receivers for ds-cdma communication systems. IEEE Transactions on Signal Processing 48, 7 (July 2000): 2145--2150.

38. Vaidynathan, C., Buckley, K. M., and Hosur, S. A. Blind adaptive antenna array for cdma systems. Proceeding of IEEE Asilomar Conference on Signals, Systems and Computers 1995 2 (November 1995): 1373--1377.

39. Veen, A.-J. van der Algebraic methods for deterministic blind beamforming. IEEE Proceedings 86 (October 1998): 1987--2008.

40. Sidiropoulos, N. D., Giannakis, G. B., and Bro, R. Blind parafac receivers for ds-cdma systems. IEEE Transactions on Signal Processing 48, 3 (March 2000): 810--823.

41. Weiss, A. J. and Friedlander, B. Channel estimation for ds-cdma downlink with aperiodic spreading codes. IEEE Transactions on Communications 47, 10 (October 1999): 1561--1569.

42. Li, K. and Liu, H. Channel estimation for ds-cdma with aperiodic spreading codes. Proceeding of IEEE International Conference on Acoustics, Speech, and Signal Processing 1999 5 (March 1999): 2535--2538.

43. Monzingo, R. A. and Miller, T. W. Introduction to Adaptive Arrays. NY : Wiley, 1980.

44. Shahbazpanahi, S., Gershman, A. B., Luo, Z. -Q., and Wong, K. M. Robust adaptive beamforming for general-rank signal models. IEEE Transactions on Signal Processing 51, 9 (September 2003): 2257--2269.

45. Vorobyov, S. A., Gershman, A. B., and Luo, Z. -Q. Robust adaptive beamforming using worst-case performance optimization: a solution to the signal mismatch problem. IEEE Transactions on Signal Processing 51, 2 (February 2003): 313--324.

46. Li, J., Storica, P., and Wang, Z. On robust capon beamforming and diagonal loading. IEEE Transactions on Signal Processing 51, 7 (July 2003): 1702--1715.

47. Lee, C. -C. and Lee, J. -H. Robust adaptive array beamforming under steering vector errors. IEEE Transactions on Antennas Propagation 45, 1 (January 1997): 168--175.

48. Cox, H., Zeskind, R. M., and Owen, M. M. Robust adaptive beamforming. IEEE Transactions on Acoustics, Speech, and Signal Processing ASSP-35, 10 (October 1987): 1365--1376.

49. Haykin, S. Adaptive Filter Theory. NJ : Prentice-Hall International, 1996.

50. Proakis, J. G. Digital Communications, 3^{rd} edition. MA : McGraw-Hill, 2001.

51. Jakes, Jr. W. C. Multipath Interference. NY : Microwave Mobile Communication, Wiley, 1974.

52. Alamouti, S. M. A simple transmitter diversity scheme for wireless communications. IEEE Journal on Selected Areas in Communications 16 (Oct 1998): 1451--1458.

53. Cheon, H. and Hong, D. Performance analysis of space-time block codes in time-varying rayleigh fading channels. Proceeding of IEEE International Conference on Acoustics, Speech, and Signal Processing 2002 3 (May 2002): 2357--2360.

54. Kotecha, J. H., and Sayeed, A. M. Transmit signal design for optimal estimation of correlated mimo channels. IEEE Transactions on Signal Processing 52 (February 2004): 546--557.

55. Samardzija, D. and Mandayam, N. Pilot-assisted estimation of mimo fading channel response and achievable data rates. IEEE Transactions on Signal Processing 51 (November 2003): 2882--2890.

56. Song, Y. and Blostein, S. D. Channel estimation and data detection for mimo systems under spatially and temporally colored interference. EURASIP Journals on Applied Signal Processing (May 2004): 685--695.

57. Hassibi, B. and Hochwald, B. M. How much training is needed in multiple-antenna wireless links?. IEEE Transactions on Information Theory 49 (April 2003): 951--963.

58. Dong, M. and Tong, L. Optimal design and placement of pilot symbols for channel estimation. IEEE Transactions on Signal Processing 50 (December 2002): 3055--3069.

59. Budianu, C. and Tong, L. Channel estimation for space-time orthogonal block codes. IEEE Transactions on Signal Processing 50 (October 2002): 2515--2528.

60. Zhu, H., Farhang-Boroujeny, B., and Schlegel, C. Pilot embedding for joint channel estimation and data detection in mimo communication systems. IEEE Communications Letters 7 (January 2003): 30--32.

61. Vosoughi, A. and Scaglione, A. Everything you wanted to know about training: guidelines derived using the affine precoding framework and the crb. to appear in IEEE Transactions on Signal Processing.

62. Pease, M. C. Methods of Matrix Algebra. NY : Academic Press, 1965.

63. Perlis, S. Theory of Matrices. MA : Addison-Wesley Press, 1952.

64. Geramita, A. V. and Seberry, J. Orthogonal Designs. NY : Marcel Dekker, 1979.

65. Khuri, A. I. Advanced Calculus with Applications in Statistics. NY : Wiley, 1993.

66. Tarokh, V., Seshadri, N., and Calderbank, A. R. Space-time block coding for wireless communications: performance results. IEEE Journal on Selected Areas in Communications 17 (March 1999): 451--460.

67. Ojanperä, T. and Prasad, R. An overview of third generation wireless personal communications: A european perspective. IEEE Personal Communications 5 (December 1998): 59--65.

68. Cimini, Jr. L. J. and Sollenberger, N. R. Ofdm with diversity and coding for high-bit-rate mobile data applications. Proceeding of IEEE Global Telecommunications Conference 1997 (November 1997): 305--309.

69. IEEE, IEEE Std 802.11a: Wireless LAN Medium Access Control (MAC) and physical layer (PHY) specifications: High-speed physical layers in the 5GHz band, 1999.

70. ETS, ETS Std 300 401: Radio Broadcasting Systems; Digital Audio Braodcasting (DAB) to mobile, portable and fixed receivers, 1997.

71. ETS, ETS Std 300 744, v1.2.1: Digital Video Broadcasting (DVB) framing structure, channel coding and modulation digital terestrail television (DVB-T), 1999.

72. Su, W., Safar, Z., Olfat, M., and Liu, K. J. R. Obtaining full-diversity space-frequency codes from space-time codes via mapping. IEEE Transactions on Signal Processing 51, 11 (November 2003): 2905--2916.

73. Barhumi, I., Leus, G., and Moonen, M. Optimal training design for mimo-ofdm systems in mobile wireless channels. IEEE Transactions on Signal Processing 51, 6 (June 2003): 1615--1624.

74. Pirak, C., Wang, Z. J., Liu, K. J. R., and Jitapunkul, S. Performance analysis for pilot-embedded data-bearing approach in space-time coded mimo systems. Proceeding of IEEE International Conference on Acoustics, Speech, and Signal Processing 2005 (March 2005): 593--596.

75. Gong, Y. and Lataief, K. B. Low complexity channel estimation for space-time coded wideband ofdm systems. IEEE Transactions on Wireless Communications 2, 5 (September 2003): 876--882.

76. Li, Y. (G.) Channel estimation for ofdm systems with trsmitter diversity in mobile wireless channels. IEEE Journal on Selected Areas in Communications 17, 3 (March 1999): 461--471.

77. Li, Y. (G.), Winters, J. H., and Sollenberger, N. R. Mimo-ofdm for wireless communications: signal detection with enhanced channel estimation. IEEE Transactions on Communications 50, 9 (September 2002): 1471--1477.

78. Li, Y. (G.) Simplified channel estimation for ofdm systems with multiple transmit antennas. IEEE Transactions on Wireless Communications 1, 1 (January 2002): 67--75.

79. van de Beek, J. J., Edfors, O., Sandell, M., Wilson, S. K., and Borjesson, P. O. On channel estimation in ofdm systems. Proceeding of IEEE Vehicular Technology Conference 1999 (July 1999): 815--819.

80. Edfors, O., van de Beek, J. J., Wilson, S. K., Sandell, M., and Borjesson, P. O. Ofdm channel estimation by singular value decomposition. IEEE Transactions on Communications 46 (July 1998): 931--939.

81. Li, Y. (G.), Cimini, L. J., and Sollenberger, N. R. Robust channel estimation for ofdm systems with rapid dispersive fading channels. IEEE Transactions on Communications 46 (July 1998): 902--915.

82. Chang, M, -X., and Su, Y. T. Model-based channel estimation for ofdm signals in rayleigh fading. IEEE Transactions on Communications 50, 4 (April 2002): 540--544.

83. Wang, X. and Liu, K. J. R. Channel estimation for multicarrier modulation systems using a time-frequency polynomial model. IEEE Transactions on Communications 50, 7 (July 2002): 1045--1048.

84. Pandana, C., Sun, Y., and Liu, K. J. R. Channel-aware priority transmission scheme using joint channel estimation and data loading for ofdm systems. to appear in IEEE Transactions on Signal Processing.

85. Wang, X. and Liu, K. J. R. Model based channel estimation framework for mimo multicarrier communication systems. IEEE Transactions on Wireless Communications 4, 3 (May 2005): 1--14.

86. Steele, R. Mobile Radio Coomunications. NY : IEEE Press, 1992.

87. Stuber, G. Principles of Mobile Communications. MA : Kluwer, 2001.

Appendices

Appendix A
List of Abbreviations

A/D	analog to digital
AWGN	additive white Gaussian noise
BER	bit error rate
bps	bit per second
CDMA	code-division multiple access
CM	code multiplexing
CMA	constant modulus algorithm
CRLB	Cramer-Rao lower bound
CSI	channel state information
D/A	digital to analog
DAB	digital audio broadcasting
DC	down converting
DD	decision-directed
DFT	discrete Fourier transform
DOA	directions of arrival
DR	despread-respread
DS-CDMA	direct sequence code division multiple access
DSL	digital subscriber lines
DVB-T	digital video broadcasting
FCC	federal communications commission
FDMA	frequency-division multiple access
FIR	finite impulse response
FFT	fast Fourier transform
HF	high frequency

HP	half-width
IDFT	inverse discrete Fourier transform
IFFT	inverse fast Fourier transform
i.i.d.	independent and identically distributed
IRBAP	interference-rejected blind array processing
ISI	intersymbol interference
ISM	industrial, scientific, and medical
LANs	local area networks
LCMV	linear constraint minimum variance distortionless response
LMMSE	linear minimum mean square error
LMS	least mean square
LS	least squares
MAI	multiple access interference
Max SNR	maximum signal-to-noise ratio
MIMO	multiple-input multiple-output
ML	maximum likelihood
MMSE	minimum mean square error
MPSK	M-phased-shift-keyed
MSE	mean square error
MTSO	mobile telephone switching office
OFDM	orthogonal frequency division multiplexing
OFDMA	orthogonal frequency-division multiple access
PEDB	pilot-embedded data-bearing
PSAM	pilot-symbol assisted modulation
PSK	phase shift keying modulation
QAM	quadrature amplitude modulation
RLS	recursive least square
SF	space-frequency
SISO	single-input single-output
SNR	signal-to-noise ratio
SP	Sampling

ST	space-time
STBC	space-time block code
SVD	singular value decomposition
TDMA	time-division multiple access
TM	time multiplexing
TU	typical urban
ULA	uniform linear array
U-NII	unlicensed national information infrastructure
W-CDMA	wideband code-division multiple access
ZF	zero-forcing
ZMSW	zero-mean spatially white

Appendix B

Publications and Presentations

Pirak, C., Wang, Z. J., Liu, K. J. R., and Jitapunkul, S.
"A data-bearing approach for pilot-embedding frameworks in space-time coded MIMO systems," to be published in IEEE Transactions on Signal Processing, 2006.

Pirak, C., Wang, Z. J., Liu, K. J. R., and Jitapunkul, S.
"Adaptive channel estimation using pilot-embedded data-bearing approach for MIMO-OFDM systems," to be published in IEEE Transactions on Signal Processing, 2006.

Pirak, C., Wang, Z. J., Liu, K. J. R., and Jitapunkul, S.
"A data-bearing approach for pilot-aiding in space-time coded MIMO systems," to be published in Proceeding of 63^{rd} IEEE Vehicular Technology Conference 2006 (Melbourne, Australia), May 2006.

Pirak, C., Wang, Z. J., Liu, K. J. R., and Jitapunkul, S.
"Adaptive pilot-embedded data-bearing approach channel estimation in space-frequency coded MIMO-OFDM systems," to be published in Proceeding of 63^{rd} IEEE Vehicular Technology Conference 2006 (Melbourne, Australia), May 2006.

Pirak, C., Wang, Z. J., Liu, K. J. R., and Jitapunkul, S.
"LS FFT-based channel estimators using pilot-embedded data-bearing approach in space-frequency coded MIMO-OFDM systems," to be published in Proceeding of IEEE Wireless Communications & Networking Conference 2006 (Las Vegas, USA), April 2006.

Pirak, C., Wang, Z. J., Liu, K. J. R., and Jitapunkul, S.
"Performance analysis for pilot-embedded data-bearing approach in space-time coded MIMO systems," Proceeding of IEEE International Conference on Acoustics, Speech, and Signal Processing 2005 (Philadelphia, USA), pp.593-596, March 2005.

Pirak, C., Prayongpun, W., and Jitapunkul, S.
"The interference-rejected blind array processing for CDMA interference cancellation in the near-far situation," Proceeding of 5^{th} World Wireless Congress 2004 (San Francisco, USA), pp.535-539, May 2004.

Pirak, C. and Jitapunkul, S.
"The JADE-estimated CM array for correlated cochannel signal recovery," Proceeding of 58^{th} IEEE Vehicular Technology Conference 2003 (Florida, USA), pp.1497-1501, Oct. 2003.

Vitae

Chaiyod Pirak was born in Chiangmai, Thailand, in 1978. He received the B.Eng. (Hons.I) degree in Telecommunication Engineering from Department of Telecommunication Engineering, King Mongkut's Institute of Technology Ladkrabang, Thailand, in 2000 and the Ph.D. degree in Electrical Engineering from Department of Electrical Engineering, Chulalongkorn University, Thailand, in association with Department of Electrical & Computer Engineering, University of Maryland College Park, the United States of America, in 2005, respectively. He received a Ph.D. scholarship from Commission on Higher Education, Ministry of Education, Royal Thai Government, for being a faculty member at King Mongkut's Institute of Technology North Bangkok after his graduation. He was appointed as a research assistance at University of Maryland College Park under the joint research program between Chulalongkorn University and University of Maryland College Park from 2003-2005. His research areas are digital signal processing for wireless communications including array signal processing, beamforming, interference cancellation techniques, channel estimation for space-time coded MIMO systems and space-frequency coded MIMO-OFDM systems, CDMA systems, etc.